OBSERVATIONS OF PHYSICAL PROCESSES IN CLUSTER CORES: CONNECTION BETWEEN THE INTRACLUSTER GAS AND THE BRIGHTEST CLUSTER GALAXY

By

Aaron Hoffer

A DISSERTATION

Submitted to
Michigan State University
in partial fulfillment of the requirements
for the degree of

Astrophysics and Astronomy—Doctor of Philosophy

2015

ABSTRACT

OBSERVATIONS OF PHYSICAL PROCESSES IN CLUSTER CORES: CONNECTION BETWEEN THE INTRACLUSTER GAS AND THE BRIGHTEST CLUSTER GALAXY

By

Aaron Hoffer

This dissertation examines the relationship between galaxy clusters and the brightest cluster galaxies (BCGs) of those clusters. It has been known for a while that the state of the hot intracluster medium (ICM) gas in the core of a galaxy cluster, quantified as the central entropy of the gas, can be found in two particular states. Galaxy clusters with central entropies greater than 30 keV cm^2 are typically disturbed clusters with no radio activity or line emission in their BCG. On the other hand, those clusters with low central entropy can host BCGs which are considered “active” and contain strong central radio sources as well as line emission suggesting star formation. While there is this dichotomy, the relative importance of physical processes which may help to create this dichotomy, is not well determined.

In Chapter 2, we examine the ultraviolet and infrared properties of BCGs in a heterogeneous sample of clusters. We find that the dichotomy still holds when investigating star formation in both the obscured and unobscured regimes. In these low entropy clusters $\sim$40% have a BCG with some form of star formation such that star formation in BCGs is enabled by the dense X-ray emitting ICM gas. The results we find are consistent with other star formation indicators, such as Hα, but we are able to create a more complete picture of the star formation occurring in the BCG.

In Chapter 3 we conduct an in depth investigation of the cool core galaxy cluster RXJ 2014.8-2430. Based on *Chandra* X-ray data, we find the cluster core is sloshing. However,

the BCG is still located near the X-ray peak and the metallicity is still centrally peaked, which suggests sloshing is a recent phenomenon. Also, we do not find X-ray cavitites even though they are expected in a cool core with radio emission. We simulate X-ray images with various bubble configurations and sizes to set limits on what we could have missed in the data. We analyze narrow band Hα imaging and optical spectra and find elongation of the Hα filaments along the same east-west axis of the sloshing. The emission line spectra show a velocity gradient across the central Hα region, suggesting the galaxy is getting pulled into or out of the cluster. The weak sloshing as well as the limit on X-ray cavities suggests we may be observing RXJ 2014.8-2430 during a rare period where sloshing and the AGN are beginning to heat the cluster core.

In Chapter 4 we present results from our polarimetry pilot study for the optical imager on the Southern Astrophysical Research (SOAR) Telescope. We discuss the methodology used to collect the data and determine data quality for appropriate analysis. We verify that we can reproduce polarization fractions and angles in sources that are polarization standards. We attempt to measure polarization in the Hα filaments in the BCG M87, but do not find a statistically significant measurement of polarization in the filaments and place an upper limit on their total polarization. The limit on polarization of emission from the filaments in M87 limits the role saturated thermal conduction can play at the interface of the hot ICM and the cold filaments. We summarize the results of the dissertation in Chapter 5.

For my grandmother, Lauretta Cohen.

ACKNOWLEDGMENTS

Thanks to Megan Donahue for helping me navigate the densely packed forest which is the world of observational astronomy as well as securing funding during my time here so I could focus on my research. For funding during graduate school, I would like to thank Michigan State University Department of Physics and Astronomy as well as the College of Natural Sciences for my teaching assistantship, thesis completion fellowship, and conference travel grant. During most of my time here as a researcher I would like to thank the following for the funding provided: Marc Postman from the Space Telescope Science Institute (STScI) and CLASH, *Spitzer* through JPL, *Chandra*, and William Sparks (also from STScI) for the purchase of the SOI polarizers purchased under the STScI Directors Discretionary Research Fund.

I'd also like to thank my coauthors and collaborators: Mark Voit, Amalia (Molly) Hicks, Deborah Haarsma, William Sparks, Ramón Barthelemy. I'd also like to thank others I have met at my three trips to AAS as well as the CIAO and Sherpa staff at the X-ray summer school for providing helpful discussion to further my work. Thanks goes out to all of the SOAR operators Daniel Maturana, Patricio Ugarte, Sergio Pizarro, and Alberto Pasten for their great assistance during our observing nights as well as Steve Heathcote and Sean Points to help troubleshoot the bigger issues with the telescope. I'd like to thank Shawna Prater and Debbie Barratt for making sure I crossed all of my 'i's and dotted all of my 't's so I wasn't dis-enrolled before I even got to MSU. And no one could survive grad school without other grad students to commiserate with. So I'd like to thank all of those graduate students past and present in astronomy for both scientific discussion and commiseration in classes and research to some very non-scientific discussion.

Also, I would like to thank my parents for providing an immeasurable amount of support to get me to this point in my life. Thanks to my brothers for continuing to be their annoying selves. Thanks to Emi for making it work from so far away and letting me be a house husband while I search for a job. Thanks to a former stranger who let me borrow her tent. Thanks to Raft, Toad, and the SHC for being amazing places to live and meet truly unique people. Thanks to the rest of my family and friends back home who make it fun to pick back up where we left off.

This research has made use of SAOImage DS9, developed by Smithsonian Astrophysical Observatory. This research has made use of the SIMBAD database, operated at CDS, Strasbourg, France. This research has made use of the NASA/IPAC Extragalactic Database (NED) which is operated by the Jet Propulsion Laboratory, California Institute of Technology, under contract with the National Aeronautics and Space Administration. Based on observations obtained at the Southern Astrophysical Research (SOAR) telescope, which is a joint project of the Ministério da Ciência, Tecnologia, e Inovação (MCTI) da República Federativa do Brasil, the U.S. National Optical Astronomy Observatory (NOAO), the University of North Carolina at Chapel Hill (UNC), and Michigan State University (MSU).

Support for this thesis was provided by Michigan State University through Prof. Donahue's startup funds, from the Physics and Astronomy Department and College of Natural Sciences. This work is based in part on observations and archival data obtained with the Spitzer Space Telescope, which is operated by the Jet Propulsion Laboratory, California Institute of Technology under a contract with NASA and data obtained with the Chandra X-ray Observatory also under contract with NASA. Support for this work was provided by NASA through an award JPL 1353923 (MSU RC065195) and JPL 1377112 (MSU RC065166) issued by JPL/Caltech. Support for this work was also provided by the National Aeronautics and Space Administration through Chandra Award Number SAO GO0-11018X issued by the Chandra X-ray Observatory Center, which is operated by the Smithsonian Astrophysical Observatory for and on behalf of the National Aeronautics Space Administration under contract NAS8-03060. Finally, partial support for this thesis with the program #12065.07 (CLASH) was provided by NASA through a grant from the Space Telescope Science Institute, which is operated by the Association of Universities for Research in Astronomy, Inc., under NASA contract NAS 5-26555.

TABLE OF CONTENTS

LIST OF TABLES

LIST OF FIGURES

Chapter 1

Introduction

1.1 Galaxy Clusters

Galaxy clusters, which contain hundreds to thousands of galaxies, are the largest gravitationally bound structures in the Universe. As their name implies, galaxy clusters were first discovered from the spatial clustering of galaxies [Zwicky, 1937, 1938]. Massive elliptical and S0 galaxies are the dominant galaxy types seen in clusters (Zwicky et al. [1961];Bautz and Abell [1973]). Galaxy clusters are different from sparse galaxy groups, such as our Local Group, which typically have tens of galaxies. Also, galaxy groups typically host lower mass spirals and irregular type galaxies as their primary galaxy types. Clusters form hierarchically [White and Frenk, 1991] such that the gravitational attraction of nearby subclusters build up to form these large self-gravitating systems. While galaxy clusters are developing, individual galaxies are also forming. During this time there are many mergers of these protogalaxies and subclusters, which heat the gas and prevent some of the gas from associating with individual galaxies. These merger events cause some of the gravitational potential energy in the cluster to convert into kinetic energy, heating up the gas particles. However, early observations belie the true nature of galaxy clusters. The mass of stars in individual cluster galaxies provides only a small fraction of the total mass in a cluster. Galaxy clusters, which are typically $10^{14} - 10^{15}$ solar masses (a solar mass is the mass of the Sun, 1.99×10^{30}

kg), are mostly dark matter ($\sim$ 85%). Perhaps more intriguing, however, is the next largest mass contribution is the diffuse low density (10^{-3} cm^{-3} e.g. [David et al., 1990b]) gas that permeates the entire cluster. It is, by far ($\sim$80%), the dominant form of baryonic mass. This diffuse gas is known as the intracluster medium (ICM) and it is very bright, with a typical luminosity of $10^{43} - 10^{46}$ erg s^{-1} ($10^{9} - 10^{12}$ solar luminosities). From the thermal motions in the cluster, the typical ICM virial temperature is $\mathrm{T}_{\mathrm{virial}} \sim 10^{7}$-$10^{9}$ K ($kT_{\mathrm{virial}} \sim$ 1-10 keV). With this high virial temperature, it wasn't discovered until the 20th century because X-ray probes located above the Earth's atmosphere are required to observe the hot gas of the ICM. In 1971, the *UHURU* X-ray satellite confirmed there is X-ray emission coming from galaxy clusters [Gursky et al., 1971]. The ICM is optically thin at X-ray wavelengths such that high energy photon emission from the ICM can stream freely from the cluster.

These massive, gravitationally bound boxes which contain dark matter, galaxies, and multiphase gas are extremely interesting astronomical sources. In this dissertation, we use multi-wavelength (from X-rays to the mid-IR) observations to study different phenomena present in galaxy clusters. Each wavelength regime presents a complementary set of observations used to better understand the physical processes in clusters. In particular, we focus on the interaction between the ICM near the center of the cluster and the central brightest galaxy, known as the brightest cluster galaxy (BCG), in the cluster. The underlying physical processes which fuel interactions between the ICM and the BCG have been a strongly contentious topic with a variety of conflicting proposed theories and models. Multi-wavelength observations that cover a wide variety of cluster types can help constrain theoretical predictions and, hopefully, be used to resolve these debates.

In the next section, we review more details about the intracluster medium. Then, we review the concept of entropy as it relates to clusters. After an introduction to entropy, we introduce the cooling flow problem and the role of BCGs in clusters. Then we discuss the cluster samples where our data are from as well as the telescopes used to collect the data. Finally, we briefly summarize each of the subsequent chapters of the thesis.

1.2 Intracluster Medium

The intracluster medium is a mixture of H and He with a typical abundance of heavier elements (abundance is defined here as the ratio of number of particles of element X to the number of Hydrogen nuclei) that is about 30% that of the Sun's heavy element abundance, and the mass in heavy elements compared to the mass in hydrogen is termed "metallicity". The source of the ICM is likely from intergalactic gas which was part of the cluster during its creation but isn't gravitationally bound by individual galaxies since the mass of the ICM is about 7 times that of the stars in galaxies. Despite its relatively high heavy element abundance, very little of the ICM could have been processed by a star, and is therefore the source of the H and He is primordial, pristine, intergalactic gas. With virial temperatures, $kT_{\rm virial} = 1 - 15$ keV, the typical thermal motions of the mostly ionized H gas are $500 - 1500$ km $\rm s^{-1}$, nearly the same velocities as the galaxies moving in the gravitational potential of the cluster. Therefore the gas is confined by the gravitational potential and the temperature of the gas is largely dictated by the depth of the potential well. Since the ICM is a highly ionized plasma, the emission is primarily free-free (i.e. thermal bremsstrahlung) which takes the form:

$$e^{ff} = 1.4 \times 10^{-27} T^{-1/2} n_e Z^2 g_B \text{ erg s}^{-1}\text{cm}^{-3}. \tag{1.1}$$

This spectral shape has an exponential cut off at high temperatures at the frequency $\nu_c = kT/h$ [Rybicki and Lightman, 1979].

In addition to this thermal continuum emission, there is line emission shown in Figure 1.1 from Sarazin and Bahcall [1977]. The relative line-to-continuum emission strength is affected by both cluster temperature as well as metal abundance. In particular, the strongest line emission in clusters is from the Fe K (7 keV) line complex, which is a blend of K lines (dominated by Fe^{+24} and Fe^{+25} bound-free emission) [Peterson and Fabian, 2006]. These line strengths are used to measure the metallicity (typically described as the Fe/H content relative to the solar abundance of Fe/H) of the cluster which is typically a third [Bahcall and Sarazin, 1977] of the solar value [Grevesse and Sauval, 1998]. Since the initial elemental distribution in the Universe is set to be about 75% hydrogen, 25% helium and trace amounts of lithium, beryllium, and boron, roughly 5 minutes after the Big Bang, carbon and heavier elements are formed as a result of massive stars which have exploded as Type II core collapse supernova early in the history of the cluster, as well as Type Ia supernova(Arnaud et al. [1992], Mushotzky and Loewenstein [1997]). Much, if not all, of these newly formed elements, even if they manage to escape their parent galaxies, are retained in the deep potential well of the clusters.

The resolution of current X-ray telescopes can't distinguish between the lines within the blends of Fe K and Fe L shells. The future generation of highly energy resolved telescopes such as Astro-H [Takahashi et al., 2010] will be required to disentangle these lines and give more precise velocities and abundances of these gases.

The X-ray surface brightness emission (photons per unit area) near the center of a relaxed, isolated cluster can usually be well described by a β model as a function of the projected

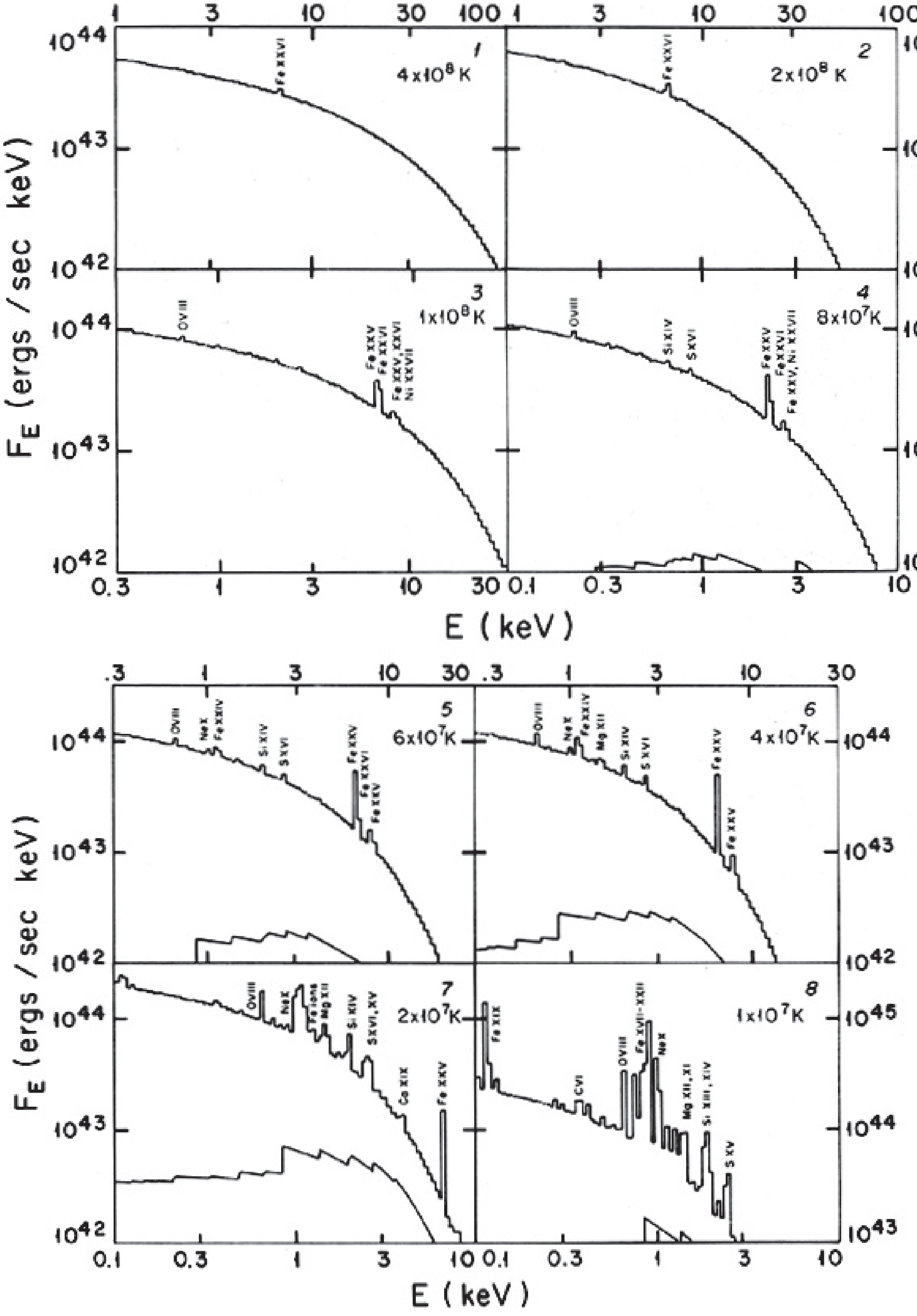

Figure 1.1 Model X-ray Spectra. Plots of numerical models which assume an isothermal gas are reproduced from Sarazin and Bahcall [1977]. The upper panels are for hotter temperature clusters and feature only the highest ionized lines on top of the thermal bremsstrahlung continuum spectrum. The models all assume spheres of gas inside a radius of 0.5 Mpc and with a proton number density of 0.001 cm^{-3}.

radius b [Sarazin, 1988]:

$$I_X(b) \propto \left(1 + \left(\frac{b}{r_c}\right)^2\right)^{-(3\beta-1)/2} . \tag{1.2}$$

In some cases, galaxy clusters with dense X-ray cores require a second β model to fit the core of the cluster. Using the X-ray surface brightness as an emission measure, ($\mathrm{EM} \equiv \int n_p n_e \, dl$) we can analytically deproject the observed surface brightness distribution to recover the true X-ray gas distribution as a function of the physical radius r:

$$\rho_g(r) \propto \left(1 + \left(\frac{r}{r_c}\right)^2\right)^{-3\beta/2} . \tag{1.3}$$

The use of a β model is not derived from physical principles, it is a useful form to describe the surface brightness profile, inasmuch as it accurately represents the shape and can be used as a reference model to detect asymmetries and other substructure. But because it is not a physical model, using it to extrapolate beyond the detected surface brightness can lead to errors. For our work, we confine the analysis to the detected regimes (e.g. Lea et al. [1973],Kellogg and Murray [1974]).

Photon energies are also recorded in an X-ray dataset. Using the energy information, X-ray spectra can be created by collecting photon events from spatial regions and binning them as a function of photon energy. From the comparison of that spectrum with plasma emission models, the temperature of the ICM gas can be estimated from the thermal bremsstrahlung cut-off frequency, such as those shown in Figure 1.2, to the spectrum. With some additional assumptions, the densities and temperatures measured can be used to calculate the pressure and entropy of the system, which lead to important insights about the state of the ICM and the thermodynamic history of the cluster.

1.3 Cluster Entropy

Entropy is an important and fundamental thermodynamic quantity. On a macroscopic scale, it represents the amount of energy available in the system related to heat transfer in the form $dS = dQ/T$. Our two main ICM observables, temperature and density, are combined to make an estimate of the gas entropy. Temperature is sensitive to the depth of the gravitational potential, while the density of the ICM is set by the entropy distribution. For example, if the gas entropy is low, the ICM can get quite dense; if it is high (say it has been highly shocked before it falls into the cluster) it will remain at a low density, it can't be compressed very easily.

We can compare the adiabatic equation of state for an ideal monatomic gas, $P = K\rho^{\gamma}$ where K is the adiabatic constant, $\gamma = 5/3$ for a monatomic gas to the ideal gas pressure, $P = \rho kT/\mu m_H$ where μ is the mean molecular weight of the gas and m_H is the mass of hydrogen. From here we can solve for the adiabatic constant K to be

$$K = \frac{kT}{\mu m_H \rho^{2/3}}. \tag{1.4}$$

In terms of our X-ray measurables, electron density, n_e, and X-ray temperature, T_X (measured in keV), the adiabatic constant becomes:

$$K = \frac{T_X}{n_e^{2/3}}. \tag{1.5}$$

By simply measuring the surface brightness and fitting the spectra of the X-ray image of the cluster, we can solve for the adiabatic constant of the cluster. The adiabatic constant K is related to the specific entropy $s = k$ ln $\mathrm{K}^{3/2} + \mathrm{s}_0$, which we can use to compare the relative thermodynamic states between clusters with simple X-ray observables. Because of this relationship, in this dissertation we use the terms "entropy" and "cluster entropy" when referring to the adiabatic constant K. We expect that low entropy gas will sink into the deep gravitational potential well at the center of the cluster and any high entropy gas that is created near the cluster core will buoyantly rise to the outskirts of the cluster.

As you approach the cluster center, the entropy profile flattens to a non-zero minimum entropy and the minimum entropy that is obtained at the center varies drastically across different galaxy clusters. Cavagnolo et al. [2009] calculate the central entropy by fitting the radial entropy profile to the functional form

$$K(r) = K_0 + K_{100}(\frac{r}{100\ \mathrm{kpc}})^{\alpha} \tag{1.6}$$

where K_0 is the entropy at the center, K_{100} is the entropy at 100 kpc, and r is the distance from the center of the cluster in kpc. Figure 1.2, from Cavagnolo et al. [2009], includes a heterogeneous sample of galaxies entropy profiles. In the figure, a pure cooling model from Voit et al. [2002] is plotted as a black line for comparison. At large radii, nearly all the clusters are consistent with this profile which is reflected in the term $K_{100}(\frac{r}{100kpc})^{\alpha}$. Therefore, while the centers of clusters have some mechanism that prevents the clusters from catastrophic cooling, the outskirts of the clusters are well represented by pure cooling. We can estimate a central cooling time, which is an estimate of the time it takes for all the energy in the core gas to dissipate. The cooling time function is in the form $t_{cool} = 5nkT_X/2n_eN_H\Lambda(T,Z)$ where $\Lambda(T,Z)$ is a modeled cooling rate as a function of temperature T and metallicity Z.

Typically the cooling time at the cluster outskirts defined in this way is longer than the age of the Universe. The gas has shorter cooler times near the cluster center. In some clusters, the central cooling time can be much shorter (< 1 Gyr) than the age of the Universe. The histogram in Figure 1.2 from Cavagnolo et al. [2009], shows a significant fraction of these clusters have a short central cooling time. This was initially perplexing because it was thought that clusters should be catastrophically cooling due to a low central entropy, which would cause the gas to form a "cooling flow" leading to an extremely luminous cluster center [Cowie and Binney, 1977, Fabian and Nulsen, 1977, Mathews and Bregman, 1978].

1.3.1 Cooling Flow Problem

To quantify how "bad" the cooling flow problem is, an estimate of the amount of gas required to be cooling is approximated as

$$\frac{dM}{dt} = \frac{2L\mu m}{5kT}, \tag{1.7}$$

where M is the mass of cooling gas, L is the cooling luminosity, μm is the mean molecular mass, and T is the temperature inside the cooling radius, assuming the X-ray gas is cooling from the virial temperature at a constant pressure. From this calculation, some clusters have cooling flows approaching 1000 solar masses per year [Edge et al., 1992]. This was initially a problem because if there was so much low entropy gas collecting in the center it should be rapidly condensing and forming stars at rate more rapidly than the most vigorous star-forming galaxies. In addition, there were predictions that there should be strong emission lines in the soft X-ray (< 1 keV) to produce enough cooling to lower temperatures, but these emission lines weren't seen [Peterson et al., 2003]. Now the consensus is there must be some physical process(es) which heat up the cluster center and prevent it from catastrophically

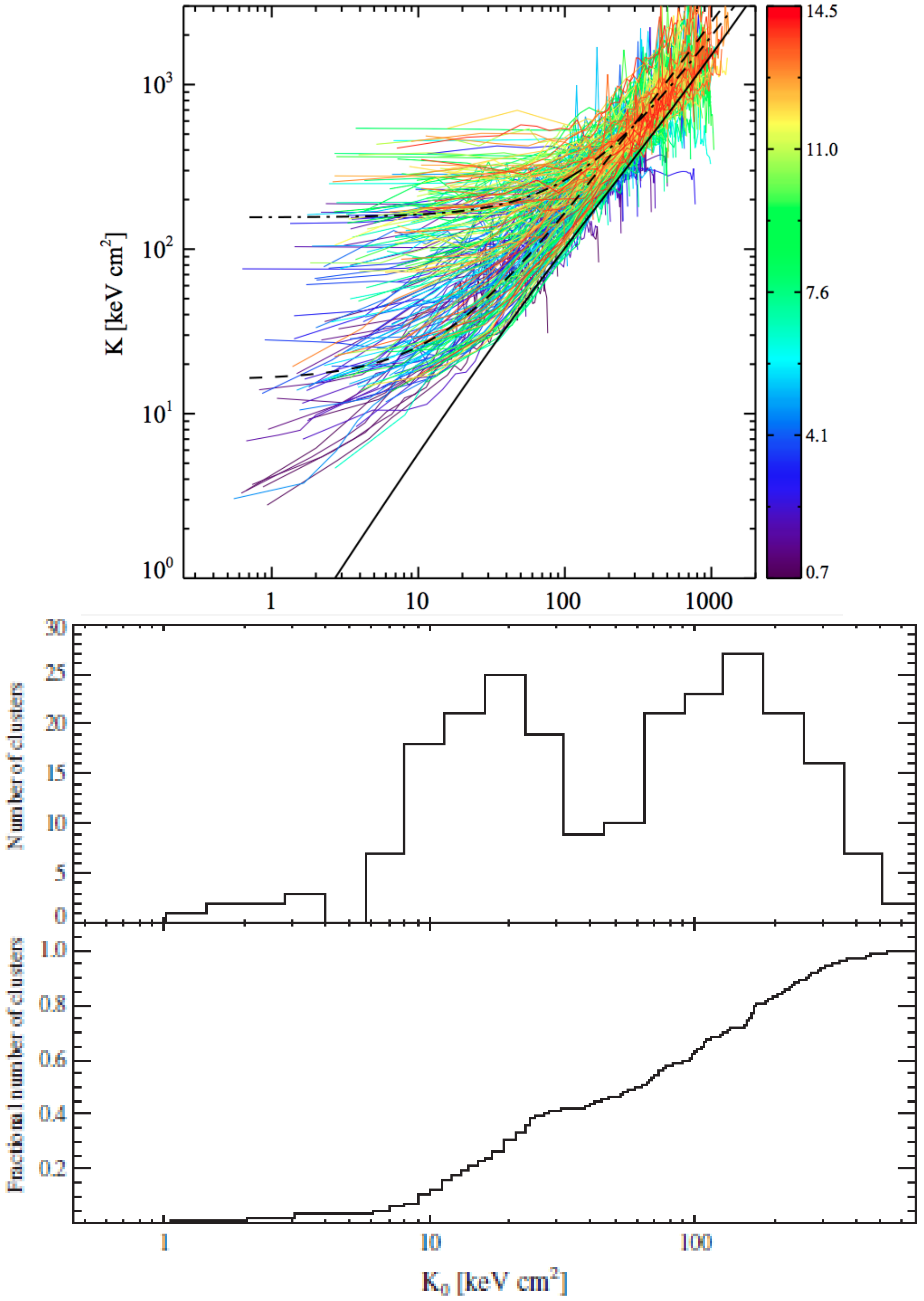

Figure 1.2 Cluster Entropy. The upper figure is reproduced from Cavagnolo et al. [2009]. The radial entropy profiles are color coded by the average cluster temperature in keV. The black line is a pure cooling model. The lower figure is also reproduced from Cavagnolo et al. [2009]. The histogram has a constant binning in log space. The cumulative histogram, though less obvious by eye, also shows the bimodality seen in the upper histogram.

cooling. Unlike their high central entropy counter parts, cool core clusters are typically very symmetric. In particular, the brightest galaxy of the cluster sits near the center where this cooling flow would terminate [Dubinski, 1998]. Therefore, many of the proposed solutions of heating of the core of the intracluster medium relate to properties of this bright galaxy. The types of effects usually considered to heat the ICM include: star formation and starbursts, AGN heating [Burns, 1990, Binney and Tabor, 1995, Churazov et al., 2001], and conduction [Tucker and Rosner, 1983, Bertschinger and Meiksin, 1986, Bregman and David, 1988, Sparks et al., 1989a]

1.4 Brightest Cluster Galaxies

Interestingly, we find that the properties of brightest cluster galaxies (BCGs), typically one or two galaxies in the cluster that are the biggest and the brightest, correlate with the central entropy of the cluster [Cavagnolo et al., 2009]. In many cases, the BCG is near the center of mass of the cluster and is known as the centrally dominant galaxy [Sarazin, 1988]. BCGs in clusters with high entropy in their cores did not show any activity indicating young stars or an active central black hole [Cavagnolo et al., 2008b]. Initially these galaxies were thought to be just the brightest cluster elliptical galaxies, but BCGs appear more extended than large cluster ellipticals [Hoessel, 1980]. Elliptical galaxies are typically the largest galaxies and are dominated by old stars without recent star formation. Given that their population is dominated by old stars, the most massive stars (which begin blue) evolve off of the main sequence and move onto their red giant phase. Lower mass stars have not evolved off of the main sequence yet, but these stars are red in color. Therefore elliptical galaxies are considered "red and dead" and aren't forming many stars compared to galaxies like spirals.

Spiral galaxies like the Milky Way form a few solar masses of stars per year [e.g. Kennicutt, 1983] while the most prolific star forming galaxies, known at starburst galaxies [Weedman et al., 1981], can have star formation rates of a few hundred solar masses per year. Those galaxies with strong star formation have some UV continuum (i.e. emission from young stars which have effective temperatures $>$ 10,000 K equivalent to a peak $<$ 300 nm) [e.g. Salim et al., 2007] and infrared continuum emission from cold dust (50 K; 100μm). Additionally, there is strong line emission in the optical and infrared. One of the dominant measurement of star formation in astronomy is Hα (i.e. the 3 to 2 transition of neutral hydrogen). Hα is seen in emission when there are stars that have UV photons with high enough energy to ionize H. The recombination of the ionized hydrogen to neutral hydrogen gives this mechanism as the most preferred transition.

BCGs have a flatter profile than large elliptical galaxies of similar size because the smooth transition from the BCG to the intracluster light (Caon et al. [1993], Gonzalez et al. [2005]). This makes it difficult to determine the total size of a BCG as they extend smoothly into the diffuse light of the cluster. Therefore, fluxes are usually measured in a metric aperture for easy comparisons between data in the literature. Typical measurements from the literature look at measurements of the core of the BCG inside of 10 kpc [e.g. Hoessel et al., 1980, Postman and Lauer, 1995].

We plot a spectral energy distribution of the nearby brightest cluster galaxy, Centaurus, from radio to gamma rays in Figure 1.3 [Ebneter and Balick, 1983] to demonstrate that, while most of the emission in a brightest cluster galaxy is in the near-infrared and comes from the old stars, there are some BCGs that have a significant amount of emission coming from the cold dust at longer mid-infrared wavelengths. Therefore, there are BCGs which can be modeled as an old stellar population (approximately a 6,000 K blackbody with stellar

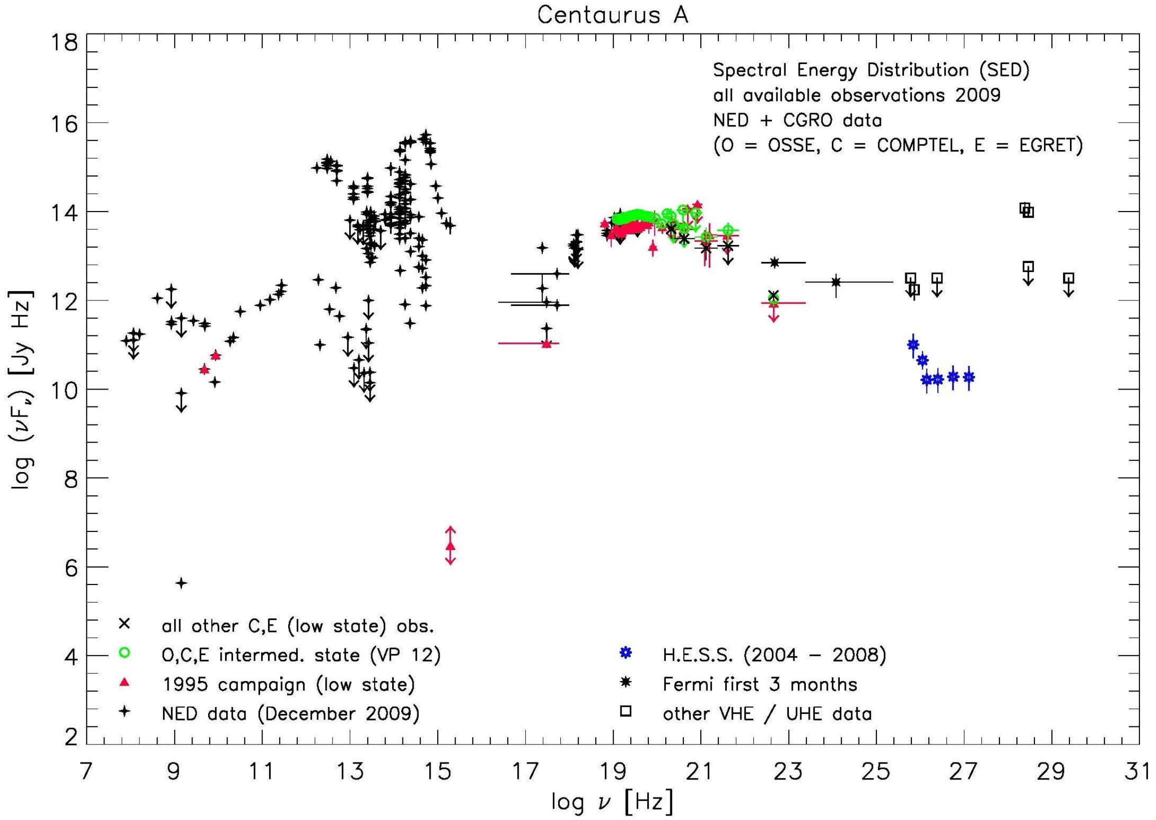

Figure 1.3 BCG Spectra Energy Distribution. The spectral energy distribution (SED) is plotted for the nearby brightest cluster galaxy Centaurus A (NGC 5128) from `http://www.mpe.mpg.de/~hcs/Cen-A/cen-a-facts.html` . There are significant contributions to the emission in the X-ray, optical, and infrared. Source is a composite SED from the NASA/IPAC Extragalactic Database [1].

atmosphere physics) plus a infrared starburst galaxy. This emission profile suggests that brightest cluster galaxies are some combination of a massive elliptical galaxy with ongoing star formation from additional cold gas.

Aside from the thermal emission of the dust in the infrared, there is additional emission in the near-infrared which is typically associated with polycyclic aromatic hydrocarbons (PAH) and silicate molecules (Draine and Li [2007], Tielens [2008]). These features result from the re-radiation of UV photons emitted by young high mass stars.

Most galaxies have a central supermassive black hole a few hundred million to a few

---

[1] `http://ned.ipac.caltech.edu/`

billion times the mass of the sun (e.g. Magorrian et al. [1998]). Some of these black holes are actively accreting material. If a black hole is accreting the material at a high enough rate, it may send some of that material back out in the form of a collimated jet. Supermassive black holes that eject this material are known as active galactic nuclei (AGN) as well as quasars (QSOs) because they were so bright and so far away.

For those galaxy clusters that have low central entropies we notice that not all of the brightest cluster galaxies associated with them are red and dead ellipticals. While all have large evolved star populations, similar to elliptical galaxies, there are some (∼40%) that also have some form of nebular emission. Heckman et al. [1989], Rafferty et al. [2008], Cavagnolo et al. [2008b] all identified brightest cluster galaxies with nebular emission. They are known to be associated with cool core clusters, which have central entropies below 30 keV cm^{-2}, however, the reason for this bimodal structure is unclear.

With the AGN in the center, this large influx of gas would cause the AGN to light up and it would increase the entropy of the gas and blow out bubbles to regulate the system. However, given the small size of AGN ($\sim$ 1 pc and the size of the cluster core (10s of kpc) it is hard to reconcile the scales. In some nearby galaxies, close enough to see the filamentary structure, some of the softest X-ray emission is co-located with these filaments [Crawford et al., 2005]. Most of the work comparing soft X-ray emission and optical line emission has been done for nearby galaxies, like NGC1275, the BCG of the Perseus Cluster (e.g. Ferland et al. [2009], Fabian et al. [2011]), and M87, the brightest cluster galaxy of the Virgo Cluster (e.g. Sparks et al. [1989a],Werner et al. [2013]).

1.5 Cluster Samples

While clusters can be interesting individually, for clusters to be truly used as a cosmological test they must be examined en masse. While there are many cluster catalogs and samples that have been constructed to study different aspects of cluster physics and cosmology, we focus our study on three particular samples: ACCEPT, CLASH, and REXCESS. We briefly review the purpose of each of these samples and how they are related to the studies in this dissertation.

1.5.1 Archive of Chandra Cluster Profile Tables

The Archive of Chandra Cluster Profile Tables (ACCEPT) examined properties of galaxy clusters which had been well observed in the Chandra archive prior to the date of publication [Cavagnolo et al., 2009]. There was a total of 239 galaxy clusters available for analysis, which were heterogenous in their morphology. However, the sample was large enough to observe a wide variety of galaxy clusters and their associated entropy profiles. We use this same sample to look for the associated brightest cluster galaxies in the *Spitzer* and *GALEX* archives to compare IR and UV star formation, respectively, to the X-ray properties found in ACCEPT.

1.5.2 Cluster Lensing And Supernova survey with Hubble

The Cluster Lensing And Supernova survey with Hubble (CLASH) is a large (524 orbit) Hubble Space Telescope (HST) Multi-Cycle Treasury Program (i.e. the data becomes public immediately after it has been taken on the telescope instead of the normal one year proprietary period) to study 25 galaxy clusters Postman et al. [2012]. Of the 25 clusters, 20 are X-ray selected clusters, most of which are relaxed clusters. These were chosen to get accurate measurements of the cluster gas mass and help measure the relative concentration of baryonic and dark matter in the cluster cores. The five remaining clusters are selected for their strong gravitational lensing characteristics. These were chosen to optimize the likelihood of discovering high redshift galaxies (z > 7) by using gravitational lensing to magnify these distant galaxies.

All of the clusters have been observed by *Chandra* and all but one (MACSJ0416.1-2403) had been in the *Chandra* archive prior to publication of the ACCEPT sample. Newer calibrations for *Chandra* as well as new data sets for some of the clusters have come out since the ACCEPT analysis, making this an interesting scientific pursuit. For this project, I was responsible for the reduction and analysis of the *Chandra* observations which were used to determine the X-ray attributes, including the X-ray gas mass, previously found in ACCEPT. The reduction and analysis tools were also used in Chapter 3 for the analysis of RXJ 2014.8-2430 (RXJ 2014.8-2430) and they are discussed in that section. This work has been included in a CLASH X-ray overview paper [Donahue et al., 2014].

1.5.3 Representative XMM-Newton Cluster Structure Survey

The Representative XMM-Newton Cluster Structure Survey (REXCESS) was a XMM-Newton Large Programme to investigate a small sample of 33 nearby (0.055 < z < 0.183) galaxy clusters [Böhringer et al., 2007a]. The goal of the survey was to sample clusters in the local Universe over a wide range of X-ray luminosity (a proxy for cluster mass) and independent on cluster morphology. From here, it would be possible to do statistics on what the galaxy cluster distribution should look like for the local Universe. The cluster RXJ 2014.8-2430 was part of this sample and found to be the strongest cool core cluster of the group. Unfortunately, the resolution of XMM is insufficient to examine kiloparsec-scale structure in the cluster core to determine what sources of heating were present in the cool core. Dr. Donahue was the PI for a *Chandra* project to examine the cluster core at a much higher resolution than would be available to XMM and look for structure near the core. These results are presented in our Chapter 3 analysis.

1.6 Telescopes and Instruments

This dissertation is composed of multiple observational studies of galaxies and galaxy clusters. To best accomplish this, a variety of telescopes and instruments with both imaging and spectroscopy were used over six orders of magnitude in wavelength from the X-ray (~ 1Å) to the mid-infrared ($\sim 160\ \mu$m). While some data were explicitly taken for this thesis, much of it was taken from publicly available archives funded and administered by NASA. Some of these data are from surveys which survey a large fraction or even the whole sky, other data are from pointed observations from previous studies requested by individual astronomers for specific projects. In the rest of this section, I will briefly overview each of the telescopes and instruments we used (or used data from) as well as a short description of each of the instruments to help motivate the reasons these telescopes were chosen to address the questions presented in this thesis.

Many of the telescopes used in this thesis are space-based telescopes. There are two main reasons for placing telescopes in space, both of which are related to effects of the atmosphere. Turbulence in the atmosphere creates distortion in the images, because a star, which appears point-like, will appear to dance around as the light is refracted through the atmosphere. For high quality sites, the typical "seeing" (i.e. FWHM of a point source) is $\sim 0.5''$ but atmospheric turbulence degrades the seeing to over $1''$ on nights. Additionally, over many wavelength regimes, the atmosphere is partially or completely opaque.

Further discussion and specifications of the telescopes and instruments are given in each of the chapters where those telescopes and instruments are used for data collection. We reduce and analyze data from GALEX, Spitzer, and 2MASS in Chapter 2. In Chapter 3 we use data from *Chandra* and the imager and spectrograph on the SOAR Telescope. In Chapter 4 we use the imager from the SOAR Telescope. The telescopes and their instruments are ordered by wavelength, from shortest observing wavelength to longest.

1.6.1 *Chandra* X-ray Observatory

The *Chandra* X-ray Observatory (abbreviated as *Chandra* or CXO) is one of the four NASA Great Observatories and has been operating since its launch into near earth orbit in 1999 [Weisskopf et al., 2002]. We used the two imaging detectors, ACIS-I and ACIS-S, which can be seen in Figure 1.4. The ACIS-S detector is back-illuminated compared to the front-illuminated ACIS-I detector.

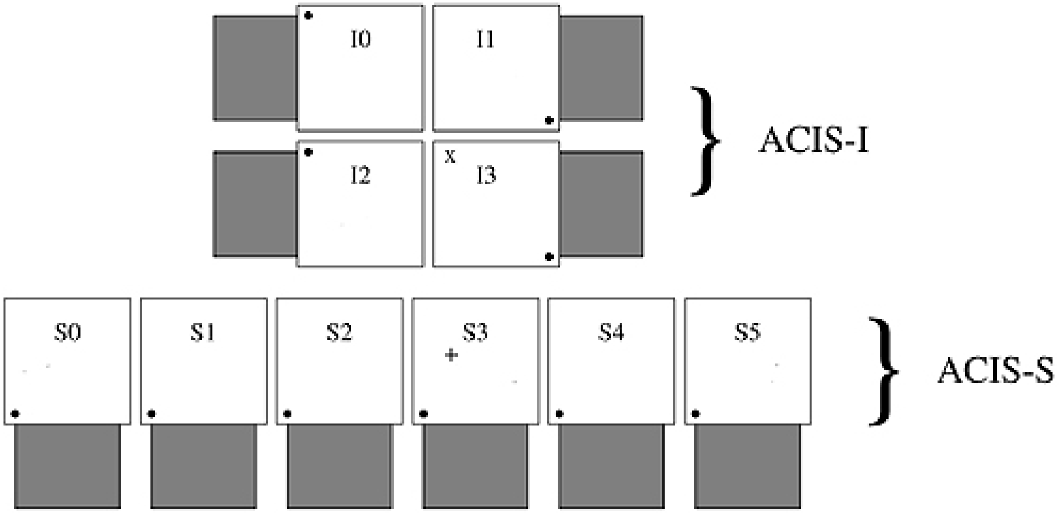

Figure 1.4 *Chandra* ACIS Chip Plane. During observations, galaxy clusters are centered on either the cross on the I3 chip or the plus on the S3 chip depending on the observer's desired configuration. The galaxy clusters we have observed typically cover part of all four of the ACIS-I chips or parts of the chips adjacent to the S3 chip. Figure courtesy of the Chandra X-ray Observatory Center, which is operated by the Smithsonian Astrophysical Observatory on behalf of NASA[2].

The goal was for the back-illuminated detectors to be more sensitive to soft X-ray emission as seen in the effective area plots in Figure 1.5. X-ray telescopes have the additional benefit that their images provided both positional information as well as energy and time information for every event (or photon). Also, *Chandra*'s principal advantage over other X-ray telescopes, such as XMM, is its excellent resolution ($0.5''$ FWHM of the PSF on axis with pixels $0.492''$ in size). For galaxy clusters, *Chandra* makes it possible to probe structure near the centers of cool core clusters, where detailed structures, such as shock fronts, as well as X-ray cavities caused by AGN, can be observed.

---

[2] `http://chandra.harvard.edu/graphics/resources/illustrations/acis_schematic-72l.jpg`

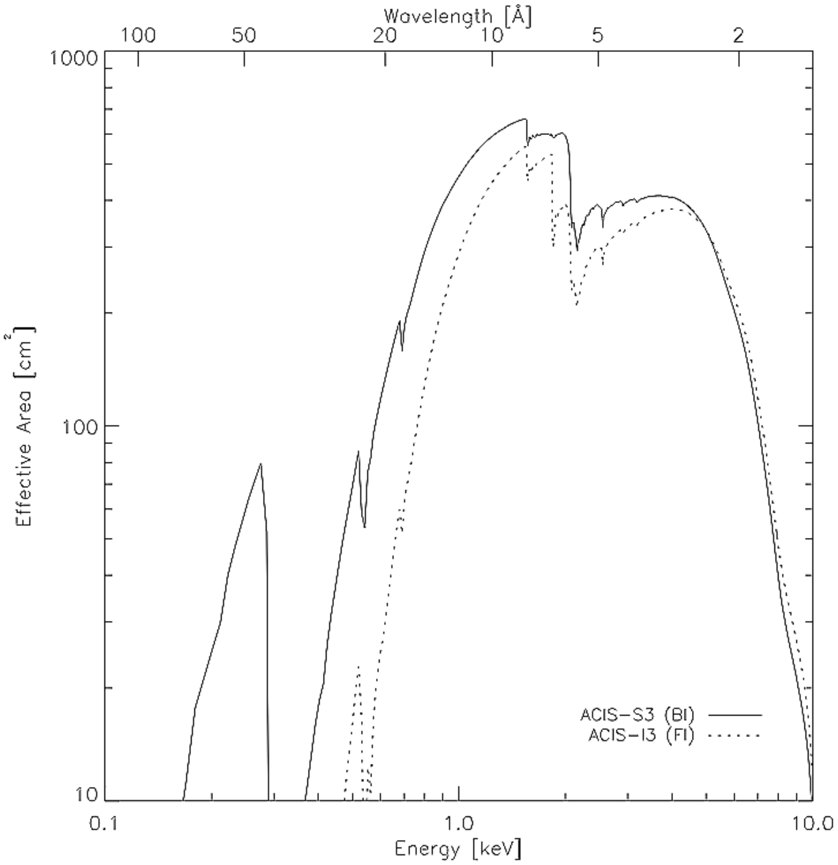

Figure 1.5 *Chandra* Effective Area. The effective area of the back-illuminated ACIS-S and front-illuminated ACIS-I detectors. Effective area as a function of wavelength is the X-ray equivalent to the filter profiles shown for optical and infrared telescopes. The main difference is the additional sensitivity the ACIS-S chips have to observe soft X-rays. Figure courtesy of the Chandra X-ray Observatory Center, which is operated by the Smithsonian Astrophysical Observatory on behalf of NASA[3].

---

[3] Figure 6.4 from `http://cxc.harvard.edu/proposer/POG/html/chap6.html`

1.6.2 Galaxy Evolution Explorer

The Galaxy Evolution Explorer (GALEX) is a space telescope built by NASA [Morrissey et al., 2007]. Similarly to X-rays, UV light is blocked by the atmosphere, so UV telescopes must be space-based. While it was designed as an all-sky survey telescope, there was time dedicated to additional follow up of targeted sources as well as general regions of the sky which were deemed to be interesting. It operated in two bands, the far UV ($1350 - 1780$ Å) and near UV ($1770 - 2730$ Å) bands which was primarily used to measure young star formation in galaxies. In Figure 1.6 we see the GALEX band-passes[4] in relation to a standard set of optical filters. Star formation less than 1 Gyr is dominated by the bluest stars, which are the most luminous. Therefore, we use GALEX Release 6 (GR6) observations of the brightest cluster galaxies in ACCEPT [Hoffer et al., 2012a].

1.6.3 Southern Astrophysical Research Telescope

The Southern Astrophysical Research (SOAR) Telescope is a 4.1 meter telescope located on Cerro Pachon, Chile and MSU is a partner, receiving a 15% fraction of the available nights in exchange for construction of the Spartan Infrared Camera.

1.6.3.1 Goodman Spectrograph

The Goodman Spectrograph [Clemens et al., 2004] was built for the SOAR telescope by the instrument group at the University of North Carolina at Chapel Hill. It is a blue-optimized optical spectrograph with imaging capabilities. It was designed to measure precise radial velocities of stars down to 1 km s^{-1} precision. We use it to measure emission line ratios

---

[4] `http://galexgi.gsfc.nasa.gov/docs/galex/Documents/ERO_data_description_2_files/image038.jpg`

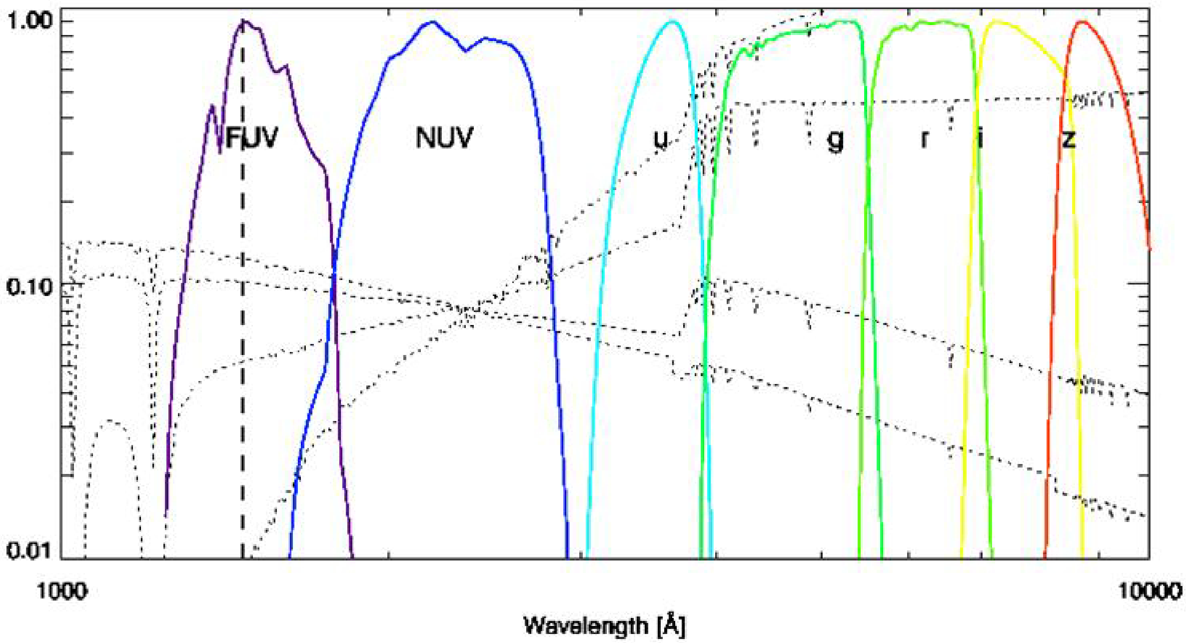

Figure 1.6 GALEX Bandpass. The NUV and FUV band-passes from GALEX are plotted in comparison to the bandpasses of the Sloan optical u′g′r′i′z′ filter set[5].

in the cores and filaments of brightest cluster galaxies. The Goodman Spectrograph's CCD is thinner than an average optical CCD, such that the Goodman Spectrograph's CCD is more ideal for observing bluer wavelengths, however, it causes interference fringing at longer wavelengths. The fringing is noticeable ($>$ 20% peak to trough oscillations) above 700 nm, which does affect some of our observations and descriptions on the methods to correct this are presented in Chapter 3. Since there is significant fringing in the red, we have concentrated our observations on Hα to low redshift BCGs.

1.6.3.2 SOAR Optical Imager

The SOAR Optical Imager (SOI) [Walker et al., 2003] was the first instrument on the SOAR Telescope. It has an approximate field of $5' \times 5'$. It shares narrow-band and broad-band filters

---

[5] `http://galexgi.gsfc.nasa.gov/docs/galex/Documents/ERO_data_description_2.htm`

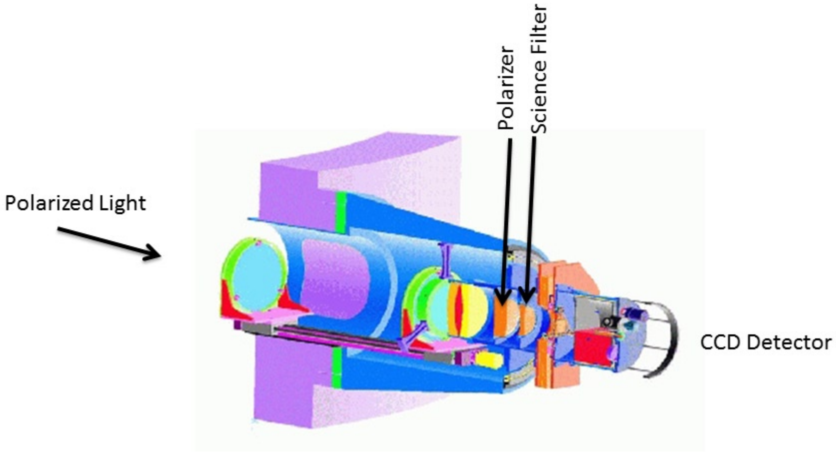

Figure 1.7 SOI Polarimeter Setup. The set up of the SOI instrument[6]. The polarizers are placed in the filter wheel closest to the sky to polarize the light prior to applying wavelength dependent filters. Image provided by the SOAR Telescope[7].

with the CTIO Blanco telescope. The variety of narrow-band filters (typically 50-100 Å wide) allows us to examine line emission across the brightest cluster galaxies. Given the limited number of filters, we have focused our efforts of measuring Hα filaments for low redshift z<0.2 brightest cluster galaxies. Because of the width, [NII] $\lambda\lambda$ 6548, 6583 Å emission is also observed with Hα.

In fall 2010, Dr. William Sparks of STScI, through a grant from the Director's Discretionary Research Fund at that same institution, purchased a set of four linear polarizing filters $(0°, 45°, 90°, 135°)$ to introduce a polarimetry mode for SOI. In Figure 1.7 we show the SOI imager with the location of the filter wheels. When taking polarized observations, the polarizers are placed in the wheel closest to the sky. The narrow-band and broad-band filters are placed in the second filter wheel, directly behind the first filter wheel.

---

[6] `http://www.ctio.noao.edu/~points/SOI/manual_software.htm`

[7] `http://www.ctio.noao.edu/soar/`

1.6.4 Two Micron All Sky Survey

The Two Micron All Sky Survey (2MASS) was a ground-based survey in the near-infrared wavebands of J, H, and K. Like ellipticals, BCGs have most of their ordinary mass as well as luminosity in their red stars, in particular, the evolved red giants. The blackbody spectra of these stars peak in this band making BCGs particularly bright in these wavelengths. In addition to the observations, extended source catalogs were created for sources found [Jarrett et al., 2003] which we were able to use for near-infrared measurements of the stellar mass of BCGs in ACCEPT clusters.

1.6.5 Spitzer Space Telescope

The Spitzer Space Telescope [Werner et al., 2004], one of NASA's Great Observatories, was originally the Space Infrared Telescope Facility (SIRTF) and launched in 2003. Spitzer is currently in its warm mode because it no longer has cryogenic coolant. It can only use its two shortest wavelength detectors, at 3.6 and 4.5 μm, because the thermal noise is too high for longer wavelength detections. Prior to that, it observed both near- and mid-infrared emission from 3.6 to 160μm. The telescope is fairly small with a primary mirror of just 85 cm in diameter.

1.6.5.1 Infrared Array Camera

The Infrared Array Camera (IRAC) operates in four separate bands: 3.6, 4.5, 5.8, and 8.0 μm [Fazio et al., 2004]. These bands are plotted in Figure 1.8. Typically all four bands are taken during an observation, so if a galaxy was observed by IRAC, we will have data for all four wavebands. The two shortest wavelength bands are near the peak of the blackbody for a red

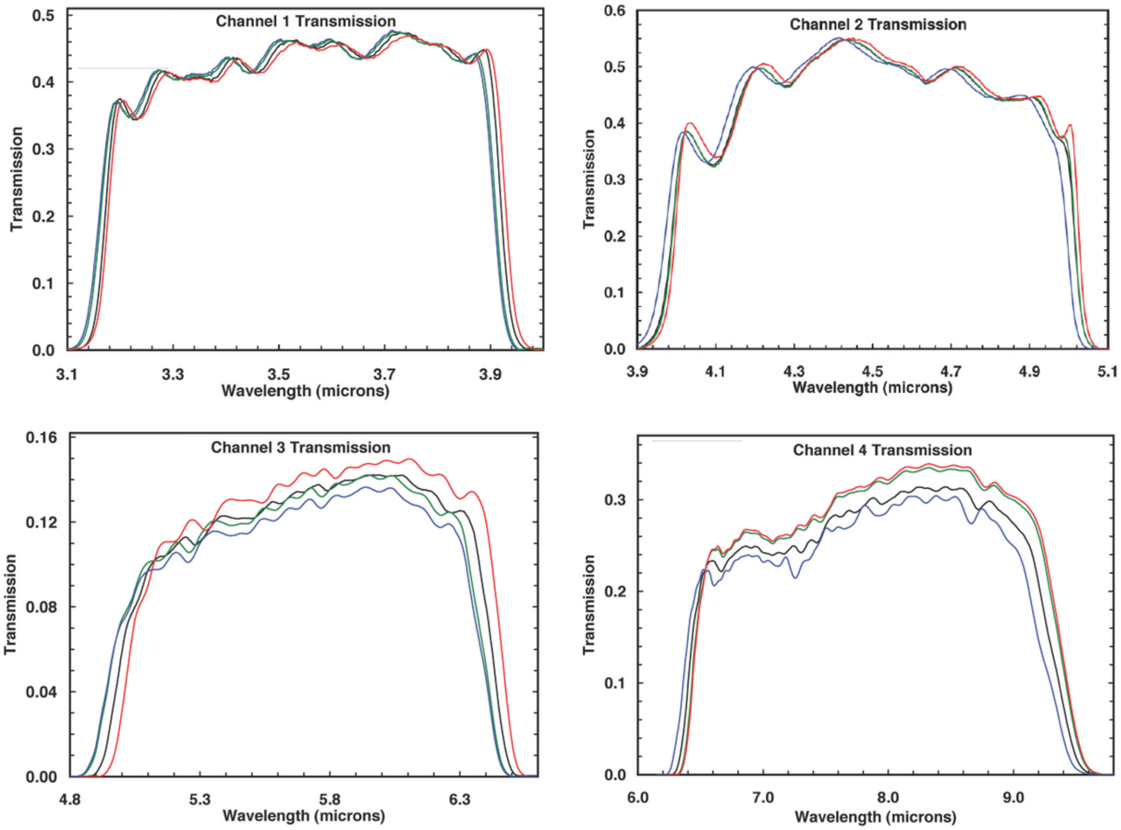

Figure 1.8 IRAC Bandpass. These are the Spitzer IRAC near-infrared band-passes. These curves describe the spectral response of the entire telescope system throughput and quantum efficiency. These curves can be used to make flux and color corrections between wavebands. Figure from the *Spitzer* Documentation and Tools[8].

giant star and are ideal for observing evolved stellar populations in elliptical galaxies. These complement the near-infrared 2MASS observations and should fit to a single blackbody. The next two bands are centered at 5.8 and 8.0 μm where there is almost no emission from a stellar blackbody. Instead these are centered on molecular features of PAHs which have been observed in many star-forming galaxies.

---

[8] `http://irsa.ipac.caltech.edu/data/SPITZER/docs/irac/calibrationfiles/spectralresponse/`

1.6.5.2 Mid IR Photometer System

The Mid-IR Photometer System (MIPS) has three detectors at 24, 70, and 160 μm all of which are diffraction limited [Rieke et al., 2004]. In addition to cold dust emission, the 24 μm band is good for detecting obscured AGN, which have their soft X-ray and UV emission re-radiated in the mid-infrared [Donley et al., 2008]. In nearby galaxies, the 70 μm filter covers the blackbody peak of $\sim$ 40 K, near a peak of continuum emisson for many star forming regions. The 160 μm band is centered on the fine structure transition of [C II] 158 μm (singly ionized carbon; the brackets are added to indicate that it is forbidden, non-dipole, transition) which is an important coolant in the interstellar medium (ISM). The fields of view of the MIPS detectors are much smaller than that of IRAC. Also, the 70 and 160 μm observations required special cooling modes so there are fewer observations of BCGs in those wavebands. While there are some star formation indicators, such as PAHs, in the IRAC bands, the majority of dust is seen in the mid-infrared covered by MIPS and these observations give us a better estimate of the total star formation.

1.7 Outline of Dissertation

This thesis investigates the physical mechanisms that drive the interactions between the hot ICM of the galaxy cluster and the cool condensed gas in some brightest cluster galaxies. In each of the subsequent chapters we examine different wavelengths and cluster samples.

In Chapter 2 we present the results from the paper Hoffer et al. [2012a]. In this paper we investigated the total star formation in brightest cluster galaxies which are in galaxy clusters in the ACCEPT sample [Cavagnolo et al., 2009]. We use the *GALEX* telescope, which operates in the UV, to look at the un-obscured star formation while we use the

Spitzer Space Telescope in the near- to mid-IR to investigate star formation that is obscured and re-radiated from the obscured UV photons in the near- to mid-IR.

In Chapter 3 we dive into greater detail of a single galaxy cluster, RXJ 2014.8-2430, which is the coolest X-ray core in the REXCESS cluster catalog [Böhringer et al., 2007a]. We examine observations from *Chandra* to look for possible X-ray cavities and shocks near the cluster core. We find sloshing in the core but do not find X-ray cavities and simulate cluster observations to set the limit on what X-ray cavities we may have missed based on the limits of our observations. We use SOAR Telescope spectra and imaging to investigate the optical line emission in the BCG, from SOI with narrow band Hα imaging and Goodman for optical spectroscopy across the BCG. Relative emission line ratios, as well as a gradient in the emission line velocities, present a picture of the gas dynamics of the emission in the BCG, which appear to be either falling in or getting pulled out of the cluster.

In Chapter 4 we move in a slightly different direction and discuss the SOAR polarimetry pilot project. For the pilot project, we present polarization maps of some famous polarized sources, including nebula and AGN. We show that not only is SOI capable of measuring polarization using a set of four polarizers, but it can place tight limits on the polarization of extended sources as well. To this end, we investigate the polarization of the Hα filaments taken from narrow band data in the M87, the brightest cluster galaxy in the nearby Virgo cluster. We place upper limits on the polarization in the off-nucleus filaments and discuss the limits of the physical mechanisms, primarily conduction, allowed to illuminate the optical filaments. There is also discussion on the steps and calibrations necessary to observe in the polarimetry mode on SOI.

We conclude the results of the work in Chapter 5 and discuss implications of these studies as well as some remaining questions which still exist and how they may be answered.

We include appendices for tables from Chapter 2. In this thesis we assume a flat ΛCDM cosmology with $H_0 = 70$ km s^{-1}Mpc^{-1}, $\Omega_\Lambda = 0.7$, and $\Omega_M = 0.3$ [Spergel et al., 2007].

Chapter 2

Infrared and Ultraviolet Star Formation in Brightest Cluster Galaxies

[1]

We present infrared (IR) and ultraviolet (UV) photometry for a sample of brightest cluster galaxies (BCGs). The BCGs are from a heterogeneous but uniformly characterized sample, the Archive of *Chandra* Cluster Entropy Profile Tables (ACCEPT), of X-ray galaxy clusters from the *Chandra* X-ray telescope archive with published gas temperature, density, and entropy profiles. We use archival *Galaxy Evolution Explorer* (*GALEX*), *Spitzer* Space Telescope, and Two Micron All Sky Survey (*2MASS*) observations to assemble spectral energy distributions (SEDs) and colors for BCGs. We find that while the SEDs of some BCGs follow the expectation of red, dust-free old stellar populations, many exhibit signatures of recent star formation in the form of excess UV or mid-IR emission, or both. We establish a mean near-UV (NUV) to *2MASS* K color of 6.59 ± 0.34 for quiescent BCGs. We use this

---

[1] This section has been previously published in the Astrophysical Journal Supplement under the same title [Hoffer et al., 2012a]. Contributing co-authors of this paper are Megan Donahue, G. Mark Voit, and Amalia Hicks of Michigan State University and Ramon Barthelemy of Western Michigan University.

mean color to quantify the UV excess associated with star formation in the active BCGs. We use both fits to a template of an evolved stellar population and library of starburst models and mid-IR star formation relations to estimate the obscured star formation rates. We show that many of the BCGs in X-ray clusters with low central gas entropy exhibit enhanced UV (38%) and mid-IR emission (43%) from 8-160 microns, above that expected from an old stellar population. These excesses are consistent with on-going star formation activity in the BCG, star formation that appears to be enabled by the presence of high density, X-ray emitting intergalactic gas in the the core of the cluster of galaxies. This hot, X-ray emitting gas may provide the enhanced ambient pressure and some of the fuel to trigger the star formation. This result is consistent with previous works that showed that BCGs in clusters with low central gas entropies host Hα emission-line nebulae and radio sources, while clusters with high central gas entropy exhibit none of these features. *GALEX* UV and *Spitzer* mid-IR measurements combined provide a complete picture of unobscured and obscured star formation occurring in these systems. We present IR and UV photometry and estimated equivalent continuous star formation rates for a sample of brightest cluster galaxies.

2.1 Introduction

The basic story underlying our current models for the formation of galaxies and clusters of galaxies is that baryonic matter falls into dark matter potential wells, cools to make cold molecular clouds, which then form stars and supermassive black holes. The state of the gas as it falls, the morphology of the accretion, the source of the dust that catalyzes formation of molecular clouds, the physical processes determining the gas temperatures and phases are all uncertain. Simply put, we do not know the full story of how intergalactic gas eventually forms stars and black holes.

Brightest Cluster Galaxies (BCGs) provide unique opportunities for the investigation of the role of hot intergalactic gas in galaxy formation, and in particular its role in affecting the evolution of the star formation and active galactic nucleus (AGN) activity in the central galaxy in the most massive dark matter halos in the universe. The intergalactic gas bound to a massive cluster of galaxies – its intracluster medium (ICM) – outweighs the stars in those galaxies by a factor of 5-10 [e.g., David et al., 1990a, Arnaud et al., 1992, Gonzalez et al., 2007]. The BCGs in the centers of X-ray clusters where the gas has a short cooling time (or equivalently, low gas entropy) exhibit signs of activity (e.g. radio sources, emission-line nebulae, excess blue or ultraviolet light) that are rare in BCGs in other clusters of galaxies [Hu et al., 1985, Burns, 1990, Cavagnolo et al., 2008b, Rafferty et al., 2008, Sanderson et al., 2009, Sun, 2009]. The activity in the BCGs of this category of clusters has been presented as evidence that hot ICM condenses into cold dusty gas that subsequently forms stars. Such BCGs may be hosting real-life versions of late-time ($z < 1$) accretion onto supermassive black holes in central galaxies; but the role of the hot ICM in AGN or star formation activity is not entirely clear.

The simplest hypothesis for how hot gas cools when it is confined to a massive dark halo fails. The first X-ray observations of the ICM in galaxy clusters indicated that some clusters have a high central gas densities and central cooling times shorter than the age of the universe(e.g., Fabian and Nulsen [1977]; Cowie and Binney [1977]). In this scenario, such gas cools slowly, loses pressure support, compresses, allowing gas from the outer parts of the cluster to settle gently into the center. The inferred mass accretion rates could be as large as 1000 solar masses per year [Fabian, 1994a]. Such clusters were dubbed “cooling flows.”

However, higher resolution X-ray spectroscopy showed that the luminous emission lines one would expect from gas cooling smoothly from 10^8K to non-X-ray emitting temperatures were not present [Peterson et al., 2003]. Nevertheless, such clusters do exhibit cool cores with radii $\sim 50 - 100$ kpc, where $kT_{core} \sim 1/2 - 1/3$ of that found in the outer radii. These clusters are now often called "cool core" clusters.

With spatially resolved X-ray spectroscopy, cool core clusters can be classified by the distribution of gas entropy of the galaxy cluster. The cluster entropy is a thermodynamic quantity. Conveniently, in a gas of pure hydrogen emitting thermal bremsstrahlung radiation, the cooling time can be written down solely in terms of the gas entropy. The gas entropy S is proportional to the logarithm of the quanitity $K = \mathrm{T_X}\ \mathrm{n_e}^{-2/3}$, conventionally reported in units of keV cm^2. Donahue et al. [2006] radially fit entropy profiles with a functional form $\mathrm{K(r) = K_0 + K_x(r/r_x)}^{\alpha}$, where $\mathrm{K_0}$ is the central entropy in excess above the power law fit. Cavagnolo et al. [2008b] extended this procedure to the entire *Chandra* archive, creating the Archive of *Chandra* Cluster Entropy Profile Tables[1] (ACCEPT). Galaxy clusters with high central entropy often contain quiescent brightest cluster galaxies (BCGs) or exhibit evidence for significant merger or interactions. The empirical boundary between clusters which occasionally host active BCGs and clusters which never host them is $\mathrm{K_0} \sim 30$ keV cm^2, an entropy associated with an ICM cooling time of ~ 1 Gyr [Voit et al., 2008]. Furthermore, about 70% of the BCGs in those cool core clusters host radio sources, and about half of those host extended emission-line nebula characteristic of low-ionization nuclear emission-line regions (LINERs; but are more extended) [Heckman et al., 1989, Crawford et al., 1999, Donahue et al., 2010]. Cavagnolo et al. [2008b] and Rafferty et al. [2008] have shown that only those BCGs inhabiting clusters with low central gas entropies (short central gas cooling

---

[1] `http://www.pa.msu.edu/astro/MC2/accept/`

times, high central gas densities) present low-ionization emission-line nebulae (Hα), blue gradients, or radio sources.

In this paper, we look for signatures strongly associated with star formation, ultraviolet (UV) excesses and mid-infrared (mid-IR) emission from dust, in the ACCEPT sample of well-studied X-ray clusters. Since even an evolved stellar population emits some UV (and mid-IR), we characterize the stellar content of the BCG using Two Micron All Sky Survey (*2MASS*) K-band photometry and photometry from the IRAC instrument on the *Spitzer* Space Telescope, short-wavelength 3.6 and 4.5 micron bands, where available. To estimate the contribution of recent star formation we measure the ultraviolet (UV) emission with the *Galaxy Evolution Explorer* (*GALEX*) observations. The UV samples the peak of emission in short-lived O and B stars, thus tracking recent, unobscured star formation. Most of the star formation in the universe occurs hidden within cold, dusty molecular clouds. The dust in these clouds absorbs the UV and optical light of buried stars and re-emits this light as mid-IR thermal radiation typical of dust at ~ 100 K. Some of this reprocessed emission emerges in the form of features, such as the emission complexes associated with polycyclic aromatic hydrocarbons (PAHs) [Donahue et al., 2011]. Puzzlingly, powerful H_2 features appear to be nearly ubiquitous in systems with Hα nebulae, at levels unlikely to be associated with typical star formation processes [Elston and Maloney, 1994, Jaffe and Bremer, 1997, Donahue et al., 2000, 2011, Egami et al., 2006]. Even colder dust (20-30K) in the far-IR has been seen with *Herschel* [Edge et al., 2010a][Edge et al., 2010b], and Edge [2001] detected significant masses of CO.

The measurements of star formation in BCGs based on UV or mid-IR information to date have been relatively limited. For example, Catinella et al. [2010] report that star formation efficiency varies little over a wide range of galaxy masses in a massive galaxy sample. However, while that sample includes 190 massive galaxies observed with *GALEX* and *Arecibo*, it has very few BCGs. Donahue et al. [2010] assessed the UV properties of the BCGs in a representative sample of 30 X-ray selected clusters from the Representative XMM-Newton Cluster Structure Survey (REXCESS) [Böhringer et al., 2007a], while most UV studies are of a limited set of the most extreme emission-line BCGs [e.g., Hicks et al., 2010, O'Dea et al., 2010]. Quillen et al. [2008] and O'Dea et al. [2008] studied 62 BCGs with *Spitzer*, selected for their luminous Hα. To expand upon these studies, we present an assessment of the UV, near-IR and mid-IR properties of BCGs in a well-studied sample of X-ray clusters. This sample is larger and more diverse than previous studies, as it includes quiescent BCGs along with the most extreme cool-core BCGs. In Section 2 we briefly describe the original X-ray cluster sample, and give an overview of the *GALEX* and *Spitzer* observations. We describe how the BCGs are identified. In Section 3 we discuss the data reduction process for the images in the *Spitzer*, *GALEX*, and *2MASS* archives. Our discussion and analysis of the data is in Section 4. We present estimates of the equivalent continuous UV and IR star formation rates in this section. UV colors are compared to those in Wang et al. [2010]. We present a summary of the observations, detections, and emission excesses in Table 2.1. We conclude the paper in Section 5. For all calculations the assumed cosmology is $H_0 = 70\text{km s}^{-1}\text{ Mpc}^{-1}$, $\Omega_M = 0.3$, $\Omega_\Lambda = 0.7$.

2.2 Observations

2.2.1 *Chandra* X-Ray Observations

The original galaxy cluster sample is from the ACCEPT database [Cavagnolo et al., 2009], which includes 239 galaxy clusters. This sample is a selection of all galaxy clusters in the

Table 2.1. Summary of Observations and Detections

Waveband	Observations	Observations ($K_0 \leq 30$keV cm^2)	Detections	Excess
NUV	168	84	112	32[a]
4.5 micron	76	52	76	13
8.0 micron	76	52	76	43
24 micron	98	56	94	24[b]
70 micron	65	46	32	32
160 micron	33	21	16	16

[a] Defined to be NUV-K color less than 6.25, which is at least one sigma bluer than the mean of the quiescent BCGs.

[b] Defined to be a 24 micron to K band ratio greater than 0.113, which is at least one sigma greater than the mean of the quiescent BCGs.

Note. — Refer to appropriate section of text for definitions of Detections and Excess.

Chandra archive as of August 2008 that met a minimum flux criterion. The clusters were selected to construct entropy profiles and provide central entropy estimates. To be able to accurately measure the entropy profiles, temperature gradients were required to have a precision better than $\Delta \mathrm{kT_X} \approx \pm 1.0$ keV. Cavagnolo et al. [2009] therefore required at least three concentric annuli with a minimum of 2500 counts each. The search resulted in 317 observations of 239 galaxy clusters. Six groups from the flux-limited Highest X-ray Flux Galaxy Cluster Sample (HIFLUGCS) sample [Reiprich and Böhringer, 2002] were added to the collection and a number of clusters with analysis complications were removed. (All additional objects are listed in Cavagnolo et al. [2009].) This sample is not a formally complete sample, but, by and large, these clusters were not selected to be included in the Chandra program because of the UV and mid-IR properties of their brightest cluster galaxies. An interestingly large fraction of these clusters now have been observed by GALEX and Spitzer, and so the time is right for a uniform analysis of the X-ray, UV, and mid-IR properties of the BCGs in the sample.

2.2.2 *2MASS* Observations - BCG identification

We used the *2MASS* archive and previous literature to determine the locations of the the BCGs in these galaxy clusters (Table A.1). The brightest cluster galaxies were initially identified by their *2MASS* position. The locations of the BCGs were determined using a visual inspection (including source brightness and morphology) with *2MASS* J-band images $5' \times 5'$ in size centered on the X-ray centroid to determine the brightest galaxy in the cluster. This visual inspection was followed up with NASA/IPAC Extragalactic Database (NED)[2] and the Set of Identifications, Measurements, and Bibliography for Astronomical Data (SIMBAD)[3] object searches within $2'$ of the X-ray centroid to verify the redshifts of the candidate BCGs. All objects in the *2MASS* Extended Source Catalog [Jarrett et al., 2003] were checked for redshift information and any other indication that they are the brightest galaxy in the cluster. Some BCGs were too distant to have associated *2MASS* catalog entries. The BCGs of these distant clusters were identified using a literature search for journal articles indicating the location of the BCG in the cluster, and are named by their right ascension and declination. For the clusters in the Sloan Digital Sky Survey (SDSS) footprint, color information and brightness in the optical (u'g'r'i'z') from the data release 7 (DR7) were used to verify the BCG selections [Leisman et al., 2011]. In a small number of cases we revised the original selection of *2MASS* location (Abell 2034, RXJ1022.1+3830, 4C+55.16, Abell 2069, Abell 368, and Abell 2255). Table A.1 gives each cluster and the *2MASS* coordinate

---

[2] `http://nedwww.ipac.caltech.edu/`

[3] `http://simbad.u-strasbg.fr/simbad/`

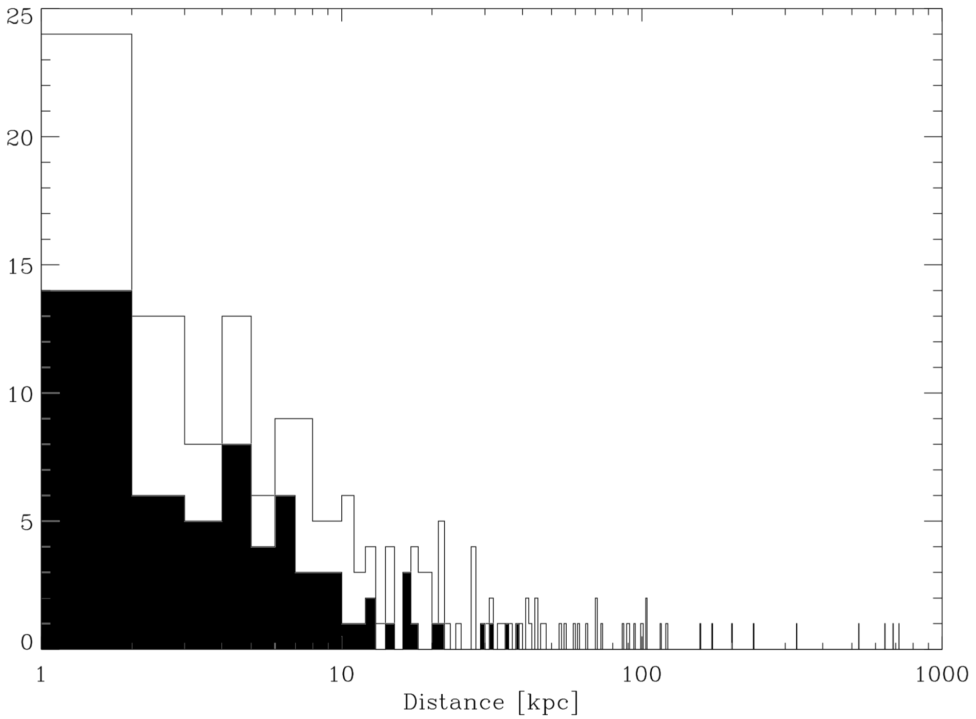

Figure 2.1 BCG Centroid Distance. The projected physical distance, in kpc h_{70}^{-1}, between X-ray centroid and the BCG we identified. All BCGs with an RA and Dec, not just those with *GALEX* and *Spitzer* data are plotted here. The the shaded region highlights BCGs in low K_0 clusters. In high central entropy systems, 37% of BCGs lie within 10 kpc of the X-ray centroid, while the percentage is increased to 74% for low central entropy systems. All BCGs which lie greater than 40 kpc away from their X-ray centroid are in high K_0 clusters.

for the brightest cluster galaxy.

In Table A.2 we list the physical separation of the BCGs from the X-ray centroid of their host galaxy clusters. While most BCGs lie near the X-ray centroid of their galaxy cluster, consistent with their identification as cD galaxies, there are a few that are very far from the center. The physical distance between the X-ray centroid and the BCG is plotted as a histogram in Figure 2.1. The BCG we identified is twice as likely to be within 10 projected kpc of its X-ray centroid in low entropy clusters (74%) compared to high entropy clusters (37%). Note that all BCGs in a low K_0 system are within 40 kpc of their cluster's X-ray centroid.

2.2.3 *GALEX* Observations

The Galaxy Evolution Explorer (*GALEX*) obtains images in the near UV (NUV) at $\lambda_{eff} =$ 2267 Å (bandpass with a full width at half maximun (FWHM) of 269 Å) and the far UV (FUV) at $\lambda_{eff} = 1516$ Å (FWHM of 616 Å) [Martin et al., 2005]. There are a total of 168 BCGs in our initial sample with *GALEX* observations in the *GALEX* archive as of 2011 October. We then searched the *GALEX* Release Six (GR6) catalog for a UV source within $5''$ of the *2MASS* BCG location. In the cases where there were multiple observations, the observation with the highest signal to noise was used. Table A.1 gives the *GALEX* object identifiers for each BCG detected. Note that not all observations will have an object identifier as the BCG may have gone undetected in the *GALEX* archive.

2.2.4 *Spitzer* Observations

We analyzed archival *Spitzer* Infrared Array Camera (IRAC) and the Multiband Imaging Photometer for SIRTF (MIPS) observations. IRAC has four near infrared wavebands at 3.6, 4.5, 5.8, and 8.0 μm [Fazio et al., 2004]. MIPS [Rieke et al., 2004] operates in the mid-IR and has three wavebands at 24, 70, and 160 μm. The *Spitzer* imaging observations selected for analysis were aimed within $1'$ from the X-ray centroid. The Astronomical Observing Request (AOR) numbers are given in Table A.1. There are 79 brightest cluster galaxies in ACCEPT with IRAC observations and 100 ACCEPT BCGs with MIPS observations as of 2010 December.

2.3 Aperture Photometry and Colors

2.3.1 *GALEX* UV Photometry

We used *GALEX* aperture photometry provided in the *GALEX* catalog and GALEXView[4]. We chose apertures to match *GALEX* measurements and derive colors with photometry from other catalogs (e.g. *2MASS*, SDSS) and with our *Spitzer* aperture photometry. The optimal aperture for the UV is determined by comparing the estimate of the total flux given in GALEXView to the circular aperture flux. The circular aperture chosen is the one with the flux measurement nearest to the estimated total flux value. For most BCGs the two largest aperture radii ($12.8''$ and $17.3''$) were used. The minimum allowed aperture radius was $9.0''$ to avoid aperture correction (the FWHM of *GALEX* observations are $\sim 4.5''-6''$). The *GALEX*-detected UV emission is usually centrally concentrated so generally, the UV emission lies within a radius of $9''$ even when the angular size, as seen in the optical, of the galaxy is larger. Therefore, the *GALEX* aperture size is an approximate upper limit on the size of the UV star formation region. Some of the UV light is produced by evolved stars [e.g., O'Connell, 1999] so we use the NUV-K color to estimate how much UV comes from recent star formation. We make photometric measurements within sufficiently large apertures to minimize the degree to which aperture corrections could affect our conclusions. The magnitudes are converted from the magnitudes given in the *GALEX* catalog to AB magnitudes using zeropoints of 20.08 magnitudes for the NUV and 18.82 magnitudes for the FUV [Morrissey et al., 2007]. The Galactic extinction corrections are applied from Schlegel et al. [1998] assuming a ratio of 3.1 for $\mathrm{A_V/E_{B-V}}$. The NUV correction assumed is $3.25\mathrm{A_V}$ and the FUV correction is $2.5\mathrm{A_V}$. UV photometry is presented in Table A.3.

---

[4] `http://galex.stsci.edu/GalexView/`

2.3.2 *GALEX* UV Upper Limits

To estimate the detection threshold for *GALEX* observations, we evaluated the cataloged fluxes of all the well-detected sources with a magnitude error < 0.35 ($S/N \gtrsim 3$) within 1° of the BCG targets. Our GALEX upper limits are based on detections of peaked sources, i.e. point sources and compact emission regions. A uniform, extended source that fills the aperture will have a higher detection threshold than this estimate. We plot these fluxes as a function of their individual exposure times in Figure 2.2. The estimated detection threshold is inferred from the upper envelope of these points, which is approximated here by curves $\propto t^{1/2}$. For the exposure times typical of the all-sky imaging survey (AIS) the estimate for the upper limit in AB magnitudes is $19 + 1.25 \times \log t_{NUV}$ for an exposure time t_{NUV} in seconds. Similarly the function for AB magnitude upper limit for the FUV is $18.5 + 1.25 \times \log t_{FUV}$. This relation underestimates the *GALEX* sensitivity for longer exposure times, longer than ~ 500 seconds. There are 9 BCGs (Abell 2319, 3C 295, Abell 611, Abell 665, Abell 1942, Abell 2631, CL J1226.9+3332, HCG 62, and Abell 2219) which had UV exposure times greater than 500 seconds and have a nondetection. For these objects we looked in the field and set the upper limit to be equal to the dimmest source that was detected (with a magnitude error less than 0.35). We report this estimated 3σ upper limit for all cases where the BCG was undetected and when the *GALEX* source flux had a large error (> 0.35 mag), indicating a highly uncertain detection. For BCGs with NUV upper limits, the *2MASS* fluxes are matched with a $7''$ aperture such that they are similar in size to the GALEX PSF.

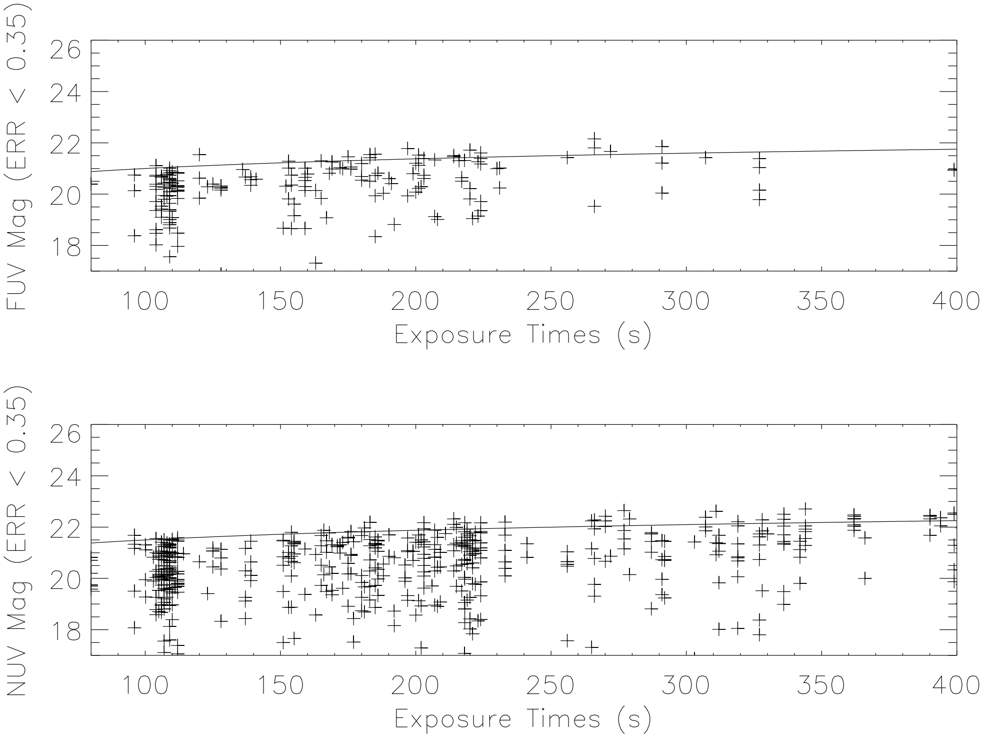

Figure 2.2 UV Magnitude Upper Limits. The UV magnitudes (AB scale) for all UV sources within 1 of the BCG locations (regardless of identity) with flux uncertainties less than 0.35 magnitudes. The upper envelope of this distribution serves as a basis for estimating the upper limit fluxes for undetected or poorly-detected BCGs for exposure times less than 400 seconds: $FUV_{UL} = 18.5 + 1.25\log_{10} t$ and $NUV_{UL} = 19.0 + 1.25\log_{10} t$. We considered all *GALEX* detections with magnitude errors > 0.35 to be poorly detected.

2.3.3 *Spitzer* Near and Mid IR Photometry

For the vast majority of the observations, *Spitzer* photometry was measured from the final pipeline product post-Basic Calibration Data (pbcd). The pipeline data were flux calibrated in units of MJy steradian^{-1} [Reach et al., 2005] from the IRAC pipeline version S18.7.0 and the MIPS pipeline version 16.1.0. For the four IRAC wavebands, fluxes were measured inside a circular aperture with a radius of $r = 14.3$ kpc h_{70}^{-1}. We wrote an IDL program to perform all aperture flux measurements for *Spitzer* [Donahue et al., 2010]. The circular aperture is centered on the BCG location in Table A.1. The backgrounds were computed from an annulus with an inner radius of $35''$ and an outer radius of $45''$ for objects which have an angular radius smaller than $35''$. For objects with flux beyond the nominal aperture, the background was computed with an annulus with an inner radius of 1.1× the radius for the object and an outer radius 1.3× the radius of the object. To estimate the mean background counts we fit a Gaussian to a histogram of counts per pixel in the background annulus. This procedure provides a background estimate that is robust to possible sources of contamination (e.g. foreground stars) that increase the counts in a small number of background pixels but do not significantly influence the mean of the Gaussian.

Most of the galaxies detected by MIPS are essentially point sources because the FWHM of the point spread function (PSF) for 24, 70, and 160 μm are $6''$, $18''$, and $40''$, respectively. We measure MIPS fluxes using the same IDL code. Since not all of the flux from the PSF falls in the aperture, MIPS aperture fluxes are corrected using the same aperture correction methods in §4.3.4 of the MIPS Handbook[5]. The 24 micron aperture radius is fixed at $13''$ with a background annulus of 15-$25''$ giving a flux correction factor of 1.167. Similarly, the 70

---

[5] `http://irsa.ipac.caltech.edu/data/SPITZER/docs/mips/mipsinstrumenthandbook/`

micron aperture radius is fixed at 35″ with a background annulus of 40-60″, and a correction factor, assuming a 30K source, of 1.22. The 160 micron observations were measured at an aperture radius of 40″ with a background annulus of 64-128″, and a correction factor of 1.752 (also assuming a 30K source). We also derived flux estimates using software provided by the *Spitzer Science Center*, APEX in MOPEX [Makovoz and Marleau, 2005], to cross-check our aperture flux measurements. The standard input parameters were used and residual images were created to assess whether the source was completely subtracted. For all sources with proper subtraction, the flux measurement from APEX was compared to the aperture measurement and we verified they were consistent within the cited errors. Only the flux values calculated from apertures are included in Table A.4. In Table 2.1 detections and excesses are equivalent for the 70 and 160 micron observations as we do not have an *a priori* belief that quiescent BCGs should exhibit 70 and 160 micron emission.

For the closest and, likely, spatially-extended BCGs, the fluxes from APEX were systematically lower than the aperture flux estimates. To determine whether any BCG had extended emission or contamination from unrelated point sources, we compared aperture-corrected flux measurements with 13″ and 35″ apertures, and we inspected the 24 micron images for point source contamination within the 35″ radius aperture. Visible contamination was classified as either insignificant, because the difference between the two aperture-corrected estimates was smaller than the statistical uncertainty of those fluxes, or significant. We inspected all detections for possible contamination inside 35″ but we only found potential contamination in the annulus between the 13″ and the 35″ radii (i.e. we saw no obvious sources of contamination inside 13″). Therefore, we do not expect contamination to affect the 24 micron point source flux measurements listed in Table A.4. However, the existence of any contaminating source seen at 24 microns is flagged for our 70 and 160 micron photometry in

Table A.4, which uses larger apertures. (Refer to the footnotes in Table A.4 for a description of the contamination categories.)

BCGs which did not have point source contamination visible at 24 microns but showed an increase in flux over that expected for a point source in the larger $35''$ aperture are considered extended. All the objects which have been identified as such are, unsurprisingly, nearby galaxies. Instead of correcting the fluxes of these objects as if they were point sources at 24 microns, the fluxes for these galaxies are reported for the large apertures we used for the IRAC photometry. (One exception, the BCG NGC 4636, was measured at a $35''$ radius instead because of significant point source contamination beyond this aperture.)

To more directly account for 70 micron contamination, if a 70 micron source was listed as a detection and the 24 micron measurement indicated contamination, the 70 micron image was inspected for contaminating sources. If a 70 micron detected source inside the aperture appears to come from an object other than the BCG (i.e. its centroid is consistent with that of a non-BCG galaxy) then the detection was downgraded to a conservative upper limit. However, these 70 micron upper limits are based on photometry using a smaller, $16''$ aperture radius with the corresponding point source correction of 1.94 to avoid including flux from extraneous point sources in the upper limit. The 70 micron upper limits estimated through this method are noted in the table. There are two BCGs, Abell 2744a and MS 04516-0305, that are contaminated at 70 microns as well as 160 microns. Upper limits for their 160 micron photometry were found using the same $16''$ aperture radius with the corresponding point source correction of 4.697.

The standard photometric error of 5% is used for the IRAC points as the systematic errors were always much larger than the statistical errors. For MIPS the standard errors are 10%, 20%, 20% for 24, 70, and 160 microns, respectively. These standard errors are usually good estimates except in the case of lower S/N detections for which statistical uncertanties are important (i.e. $S/N = 5 - 20$). We report the total errors (including statistical and systematic uncertainties) for MIPS with the flux measurements in Table A.4.

For MIPS, upper limits were estimated for detections that are below 5σ. The standard deviation of the observation was calculated in the same manner as Donahue et al. [2010]. If the standard aperture flux had a $S/N < 5$ the filtered data were used instead. The background on these data are better controlled, but the MIPS Handbook warns that low surface brightness emission in the filtered data will be lost. Therefore, the filtered data were only used when the standard source detection fell below the 5σ limit. Those filtered images that are still below the 5σ detection threshold were assigned a 5σ upper limit for that detection. If a BCG is undetected with the standard mosaic but is detected ($>5\sigma$) using the filtered data it is considered a filtered detection and is labelled as such in the Table A.4. There were many observations that were considered filtered detections in our first pass through the data, but were revised to upper limits because of 70 micron contamination from non-BCG sources.

For a few of the nearest and brightest BCGs there was an issue with the final data products in the *Spitzer* pipeline. In these cases, the BCG contained a spurious point source that was much brighter than the rest of the galaxy. These very bright artifacts proved to not be physical because the anomalous levels were not detected in the individual BCD frames. We mosaicked the individual BCD frames with the MOPEX software using the standard mosiacking procedure and settings. The new mosaic images did not exhibit the spurious point sources. The fluxes were then calculated from the new images and were in agreement with the original images if the point source was masked out. Those AORs which required remosaicking are noted in Table A.1.

2.3.4 *2MASS* Near IR Observations

2MASS J, H and K fluxes and errors are extracted from the *2MASS* Extended Object Catalog [Jarrett et al., 2003]. The catalog provides aperture photometry between $5''$ and $60''$ in radius. For a few large galaxies (e.g. M87, M49, NGC 4696) the aperture photometry was taken from the *2MASS* Large Galaxy Atlas. The measurements were converted from the system's Vega magnitudes to Janskys using the AB magnitude conversions (0.9, 1.37, and 1.84 mag for J, H, and K bands, respectively) provided in Cohen et al. [2003]. We correct *2MASS* magnitudes for Galactic extinction: $A_K = 0.112A_V$,$A_J = 0.276A_V$, $A_H = 0.176A_V$ [Schlegel et al., 1998]. In order to derive flux ratios normalized to emission dominated by the old stellar population sampled in the near-infrared, we matched apertures in the near-IR with those at other wavelengths. Therefore we estimated *2MASS* photometry (presented in Table A.5) for each source in three apertures: (1) the *GALEX* aperture for $NUV - K$, (2) the IRAC aperture of $r = 14.3h_{70}^{-1}$ kpc for IRAC to near-IR flux ratios, and (3) the 24 micron aperture (for K-band only). After extinction and k-correction, Figure 2.3 shows that the BCGs have no trend in their K band luminosity (the mean is $1.6^{+0.7}_{-0.4}\times 10^{44}$ erg $\mathrm{s}^{-1}\mathrm{h}_{70}^{-2}$) as a function of redshift or K_0 of these galaxy clusters.

2.4 Discussion

2.4.1 UV Excess and Color

The UV excess is determined by comparing $NUV - K$ colors, plotted in Figure 2.4 against excess entropy K_0 from Cavagnolo et al. [2009]. The baseline for quiescent BCGs is visible in this figure. The BCGs with excess UV emission, over and above the UV found in quiescent

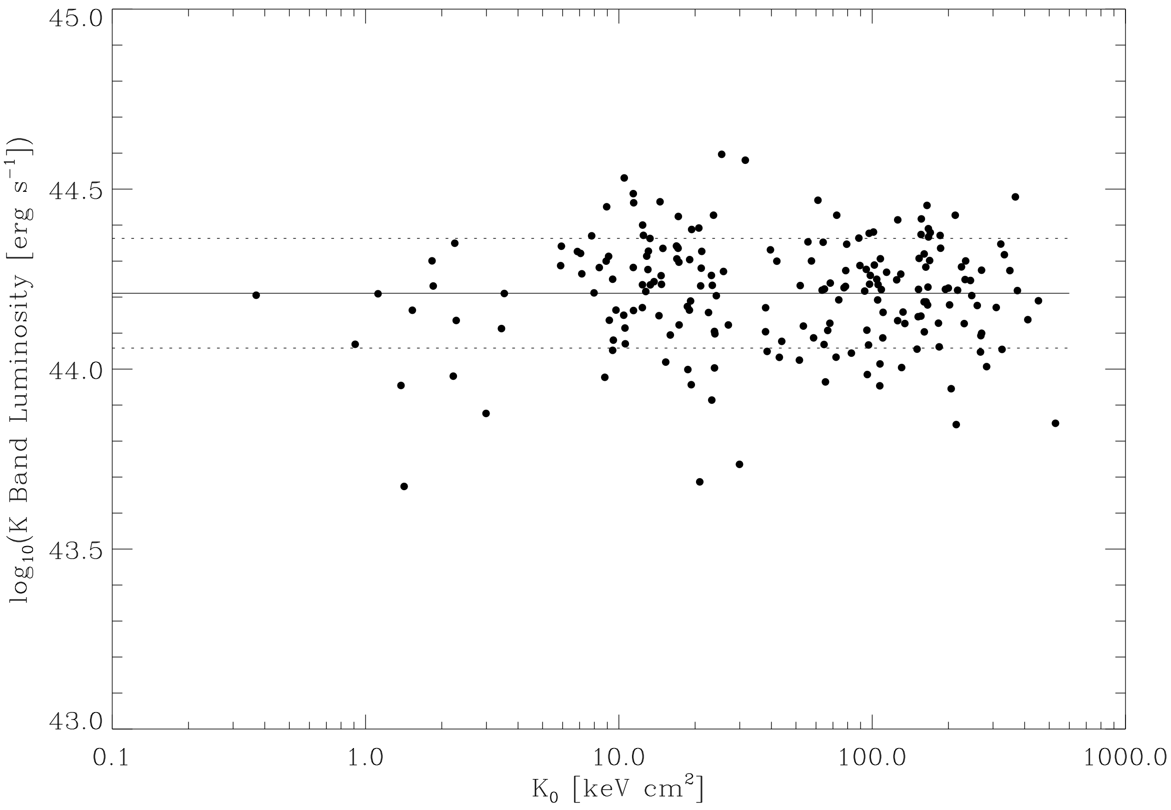

Figure 2.3 K band Luminosity. The K band luminosity is calculated from the flux inside 14.3 kpc h_{70}^{-1} kpc radius. The luminosities are k-corrected assuming passive evolution. The solid horizontal line represents the mean (1.6×10^{44} erg $s^{-1}h_{70}^{-2}$) of the data points while the dotted lines are the 1σ error ($+0.7\times 10^{44}$ erg $s^{-1}h_{70}^{-2}$, -0.4×10^{44} erg $s^{-1}h_{70}^{-2}$) on the mean.

BCGS, are only in the low K_0 galaxy clusters in the ACCEPT sample. While we find no BCGs with excess UV emission in galaxy clusters with high central entropy, there are many quiescent BCGs in low central entropy clusters. From our sample we estimate the typical $NUV - K$ color for quiescent BCGs from the mean and standard deviation of all BCGs with central entropies above 30 keV cm^2. We derive a mean color of inert BCGs is 6.59 ± 0.34. In contrast, the mean color for BCGs in clusters with central entropies less than 30 keV cm^2 is 6.11 ± 0.99. We define a color excess $\Delta_\mathrm{c} = 6.59 - (\mathrm{NUV} - \mathrm{K})$. This excess will be used in § 2.4.3 to estimate the equivalent continuous star formation rate. The color excess is simply defined such that blue light in excess of quiescent BCGs in high entropy clusters can easily be translated into a UV luminosity associated with continuous unobscured star formation. BCGs are considered to have a NUV excess in Table 2.1 if their NUV-K color is at least 1σ bluer than the mean color of inert BCGs. We see that 38% of low central entropy clusters in our sample have a NUV-K excess. The BCGs with the bluest colors are in Abell 426, Abell 1664, and RX J1504.1-0248 which have colors around 3.0.

We plot the $FUV - NUV$ and $NUV - K$ colors for BCGs in Figure 2.5. Contamination from line emission from Lyα may occur if the redshifted Lyα line is included in the FUV bandpass (within the FWHM (269 Å) of the effective wavelength (1516Å) of the FUV filter), at redshifts between $0.15 - 0.36$. The right figure plots only nearby BCGs ($z < 0.15$) to address this possible effect. Excluding the BCGs which may be contaminated by line emission ($z > 0.15$), we do not detect a significant FUV-NUV color difference between bluer BCGs (with NUV-K colors less than 6.3) and redder BCGs (with NUV-K colors greater than 6.3). The mean of the FUV-NUV color for bluer BCGs is 0.73 ± 0.57 while the mean of redder BCGs is 0.79 ± 0.30.

Wang et al. [2010] uses GALEX and SDSS to measure colors on a sample of 113 nearby

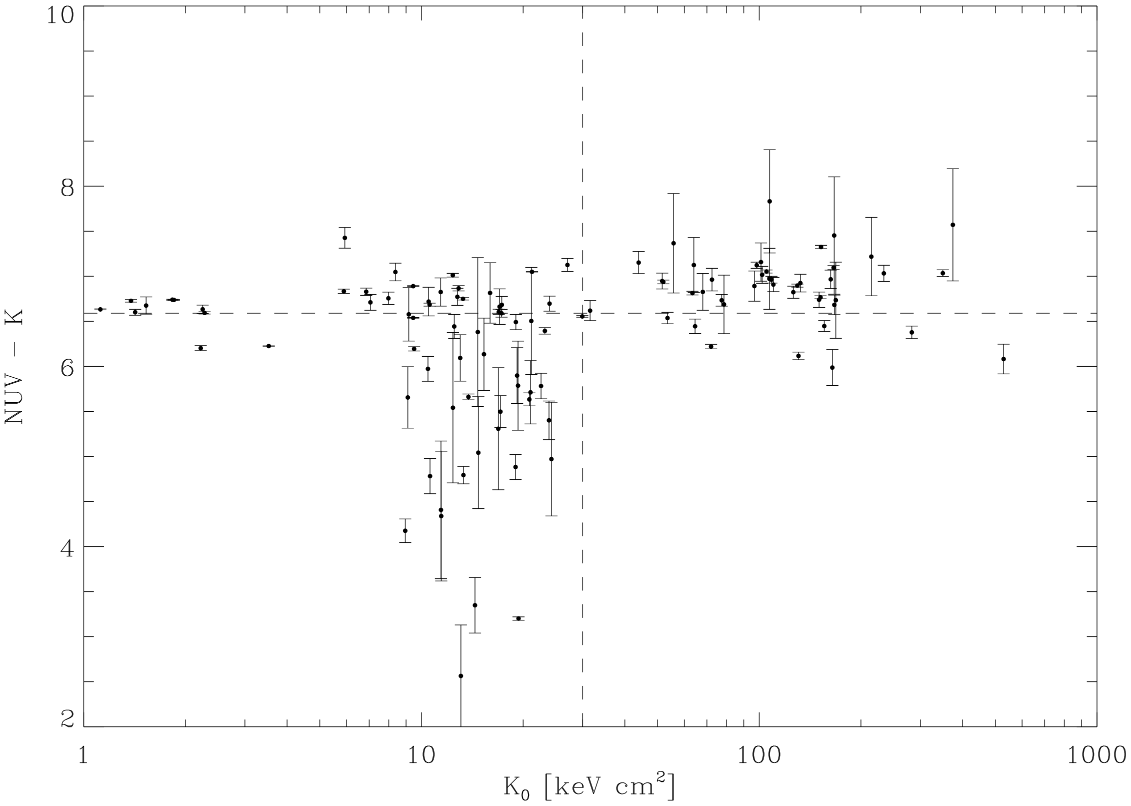

Figure 2.4 NUV-K Color. NUV-K as a function of cluster central entropy. The vertical dashed line is at 30 keV cm^2, our cutoff for the definition of low entropy clusters. Note the large color distribution for low K_0 objects, while the high entropy objects have a more consistent redder color. The K band fluxes have been k-corrected assuming passive evolution. The horizontal dashed line represents a NUV-K color of 6.59 magnitudes, the mean of the BCGs in clusters with with $K_0 \leq 30$ keV cm^2. There may appear to be a trend with the low entropy objects, but this is a selection effect where the lowest entropy objects that are observed are also the nearest objects.

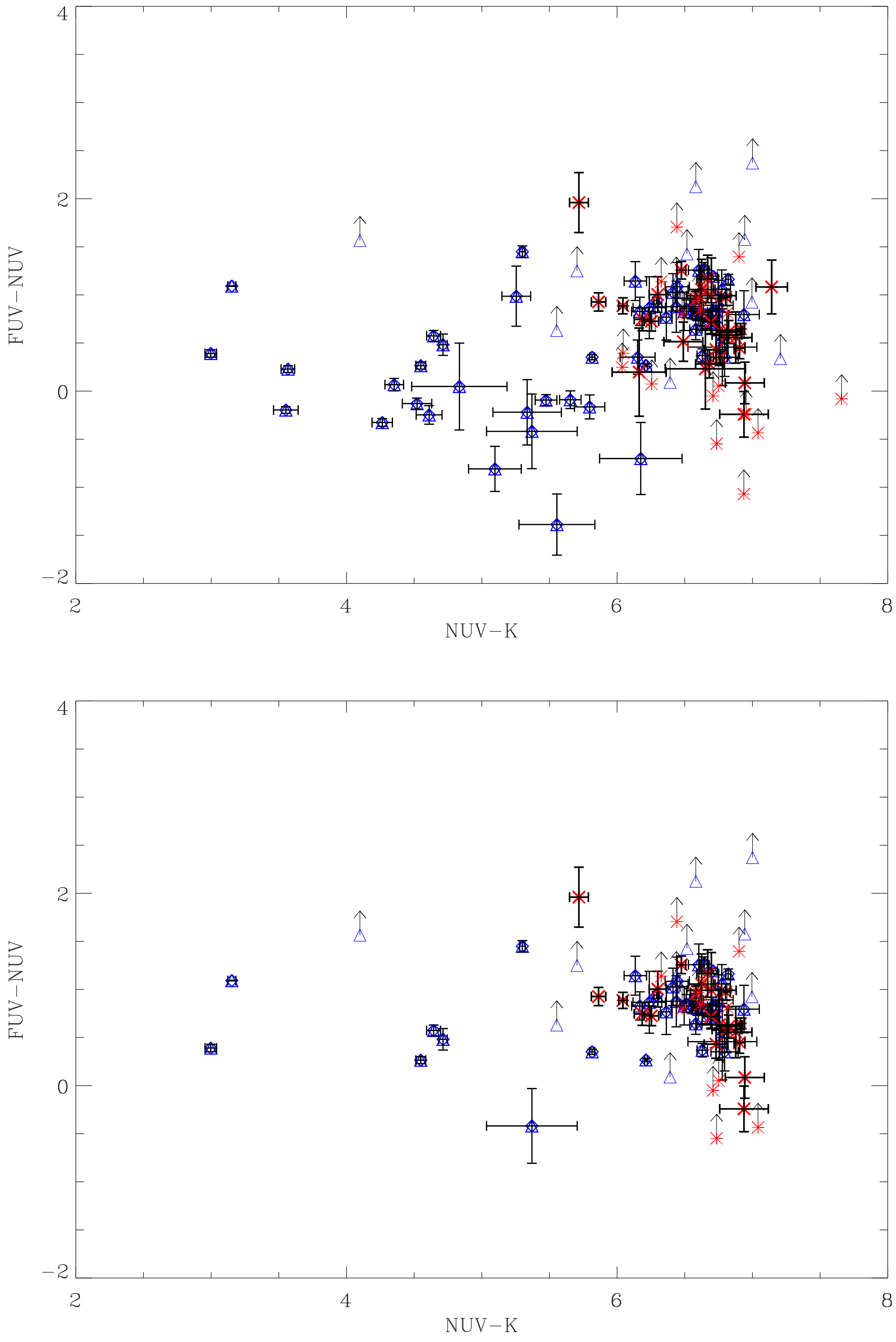

Figure 2.5 <u>FUV-NUV NUV-K Color</u>. The blue triangles are BCGs in low K_0 clusters ($\leq$ 30 keV cm^2) while the red asterisks are BCGs in high entropy clusters. The left plot includes all of the BCGs while the right plot only includes nearby ($z< 0.15$) BCGs demonstrating that the bluest FUV-NUV colors, in the left hand plot, are likely arising because of contributions from Lyα.

(z< 0.1) optically selected BCGs and compare them to a sample of field galaxies. Also, they compare their results to a sample of 21 X-ray selected BCGs from Rafferty et al. [2008] which included BCGs in both cool-core and non-cool-core clusters. From Figure 7 in Wang et al. [2010], the distribution of the FUV-NUV color is consistent with ours with a mean that better matches the photometry from their outer apertures (radius covers 90% of the light) than that measured within their inner apertures (radius covers 50% of the light). Similarly, their NUV-r colors are consistent with our NUV-K colors, after transformation between SDSS r and 2MASS K bands, assuming those bands are only affected by emission from the old stellar population.

2.4.2 IR Color

The ratios of 8.0 to 3.6 micron fluxes track the ratios of infrared emission from polycyclic aromatic hydrocarbons (PAHs), stochastically heated hot dust grains, and possibly rotationally excited molecular hydrogen and other emission lines [e.g., Donahue et al., 2011] to emission from stars. We plot these ratios as a function of redshift in Figure 2.6. The line shows the expectation for a passively evolving stellar population with an age of 10 Gyr at $z = 0$. After normalizing the ratio for the stellar population, we determine the total number that are at least 1σ above the normalized mean for BCGs in high K_0 clusters (1.014 ± 0.061) and refer to those as BCGs with excess 8.0 micron emission in Table 2.1. The points that lie well above this line are likely to have some form of hot dust and/or PAH emission as the observed IRAC 8.0 micron color is sensitive to only strong PAH features. In Figure 2.7 the IRAC ratio of 4.5 to 3.6 micron fluxes from *Spitzer* are plotted against redshift, similarly to the plot from Quillen et al. [2008]. Similar to what we have done for the 8.0 to 3.6 micron ratio, we normalize the 4.5 to 3.6 micron ratio for a passively evolving stellar population with an age of 10 Gyr at $z = 0$. We then determine a mean of the normalized ratio for BCGs in high K_0 clusters (1.048 ± 0.019). All BCGs at least 1σ in excess of the mean are considered to have excess 4.5 micron emission.

For both the 8.0 to 3.6 micron flux ratio and the 4.5 to 3.6 micron flux ratio, the only BCGs with excesses over and above a passively evolving old stellar population are those that inhabit clusters with low central entropies, as shown in Figure 2.7 and Figure 2.6. In Figure 2.8 the 8.0 to 3.6 micron ratio and the 4.5 to 3.6 micron ratio are strongly correlated ($r = 0.92$,15σ for objects with mid-IR detections and/or NUV-K excesses), which is expected if the excess 4.5 micron emission is generated by processes related to that producing the 8.0 micron emission. The functional fit plotted is

$$\log_{10}(\mathrm{F}_{8.0\mu\mathrm{m}}/\mathrm{F}_{3.6\mu\mathrm{m}}) = (0.153 \pm 0.002) + (5.422 \pm 0.021) \times \log_{10}(\mathrm{F}_{4.5\mu\mathrm{m}}/\mathrm{F}_{3.6\mu\mathrm{m}}). \quad (2.1)$$

Both the ratios have been normalized for passive evolution. As long as the IRAC calibration was consistent over time, these are precise relative flux ratios, independent of the flux calibration. The absolute flux ratios are precise to about 2%. The 8.0 and 4.5 micron bandpasses will include PAH and mid-IR emission line features associated with activity seen in cool core BCGs [Donahue et al., 2011]. The emission of dust-free, evolved stellar populations in these same bandpasses is similar to the Rayleigh-Jeans tail of a black body, decreasing steeply to longer wavelengths. We see two BCGs HCG 62 and Abell 1644 that show an excess in both normalized ratios however neither shows a NUV-K excess. Abell 1644 was not observed in MIPS and we expect to see a detection in the 70 micron waveband based on this correlation. HCG 62 has a 70 micron upper limit which may be related to the selection effect that it is a very low K_0 galaxy group. We assess the presence of a luminous dust component, likely to

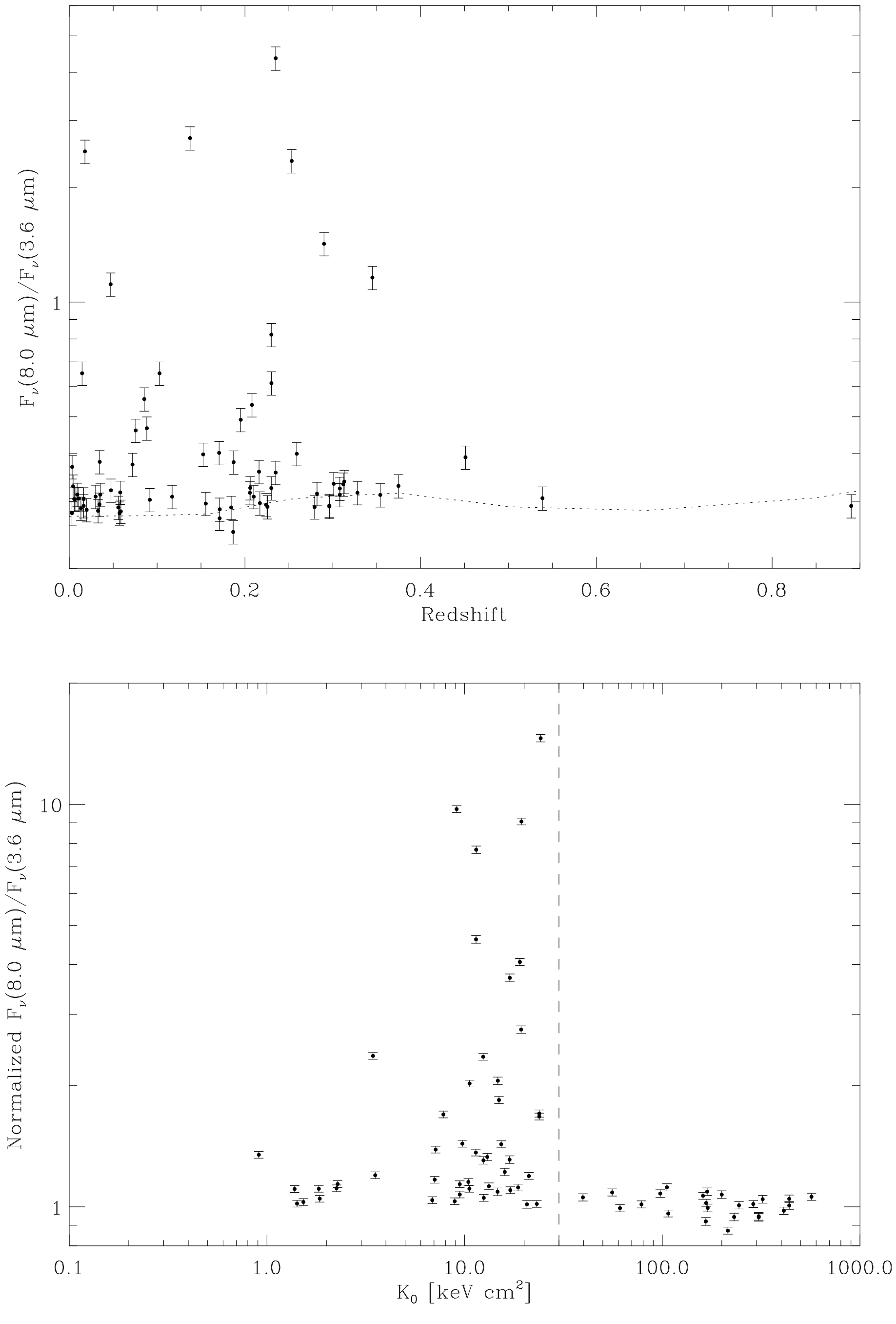

Figure 2.6 8.0-3.6 Infrared Ratio. Redshift dependence of 8.0 μm to 3.6 μm ratio. The dotted line represents the expected flux ratio for passively evolving stellar population that is 10 Gyr at $z = 0$. While IRS spectra of Hα-emitting BCGs show PAH features that would fall in the 8.0 micron bandpass [e.g. Donahue et al., 2011] the observed IRAC 8.0 micron color is sensitive to only strong PAH features. Below, the flux ratio has been normalized by the passive evolution model and is plotted against the central entropy of the cluster. The dotted line identifies the threshold 30 keV cm^2. There appears to be a deficit of excess-IR emitters in the low K$_0$ clusters, but this deficit is likely to be a selection effect since low K_0 can only be resolved in the most nearby groups.

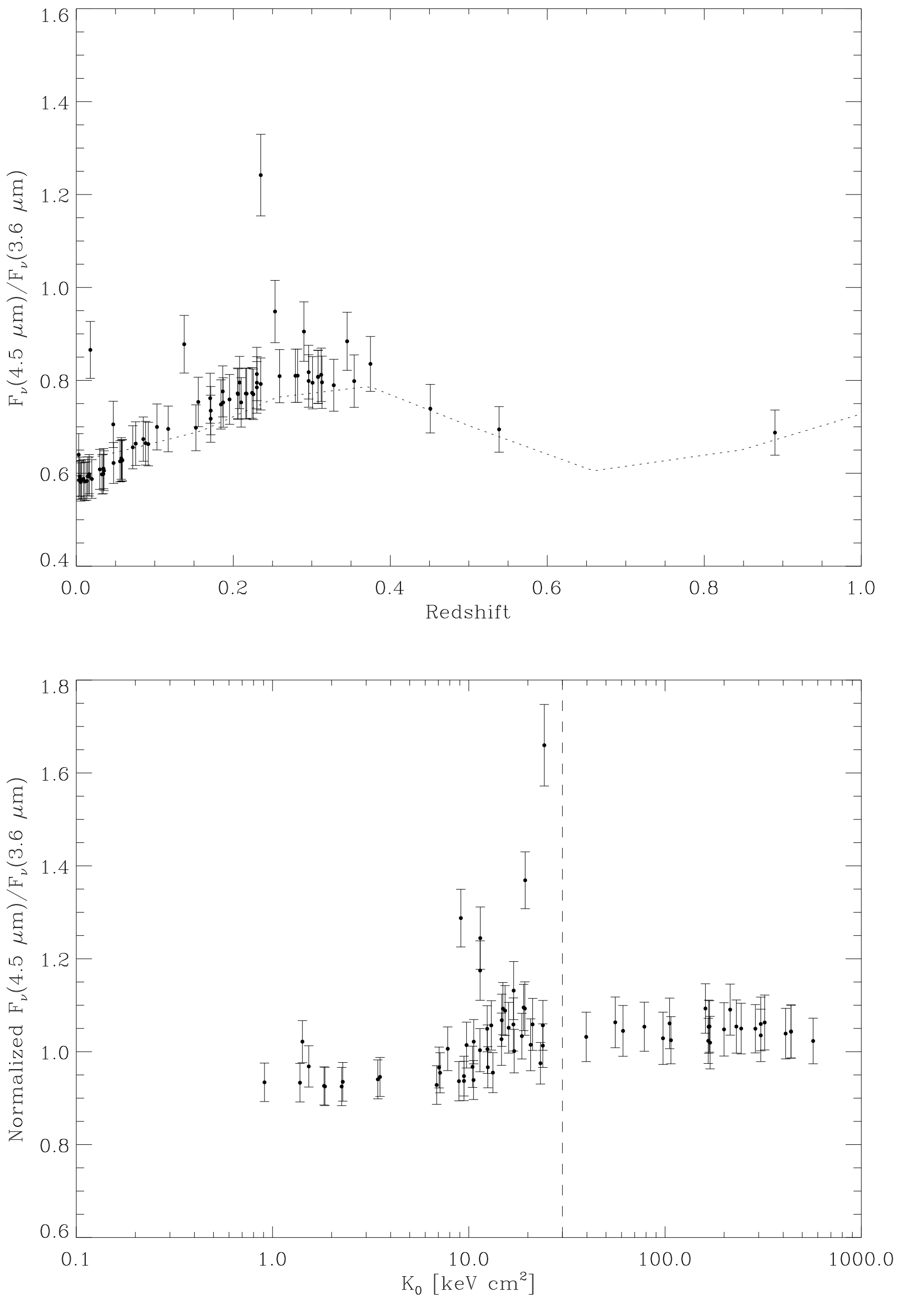

Figure 2.7 4.5-3.6 Infrared Ratio. The left hand figure shows the flux ratio between the 4.5 μm and the 3.6 μm flux is plotted as a function of redshift. The dotted line indicates a Starburst99 model for a passively evolving elliptical galaxy with a primarily old stellar population dominated by red giants, with an age of about 10 Gyr at $z = 0$. For most of the BCGs the IRAC 4.5 μm to 3.6 μm colors are consistent with those of a passively evolving population. In the figure below, the flux ratio has been normalized by the passive evolution model and is plotted against the central entropy of the cluster. The dotted line again identifies $K_0 = 30$ keV cm^2. It is interesting that the handful of BCGs (Abell 426, Abell 1068, Abell 1835, and ZwCl 0857.9+2107) with large excess 4.5 micron emission are located only in clusters with K_0 less than the threshold.

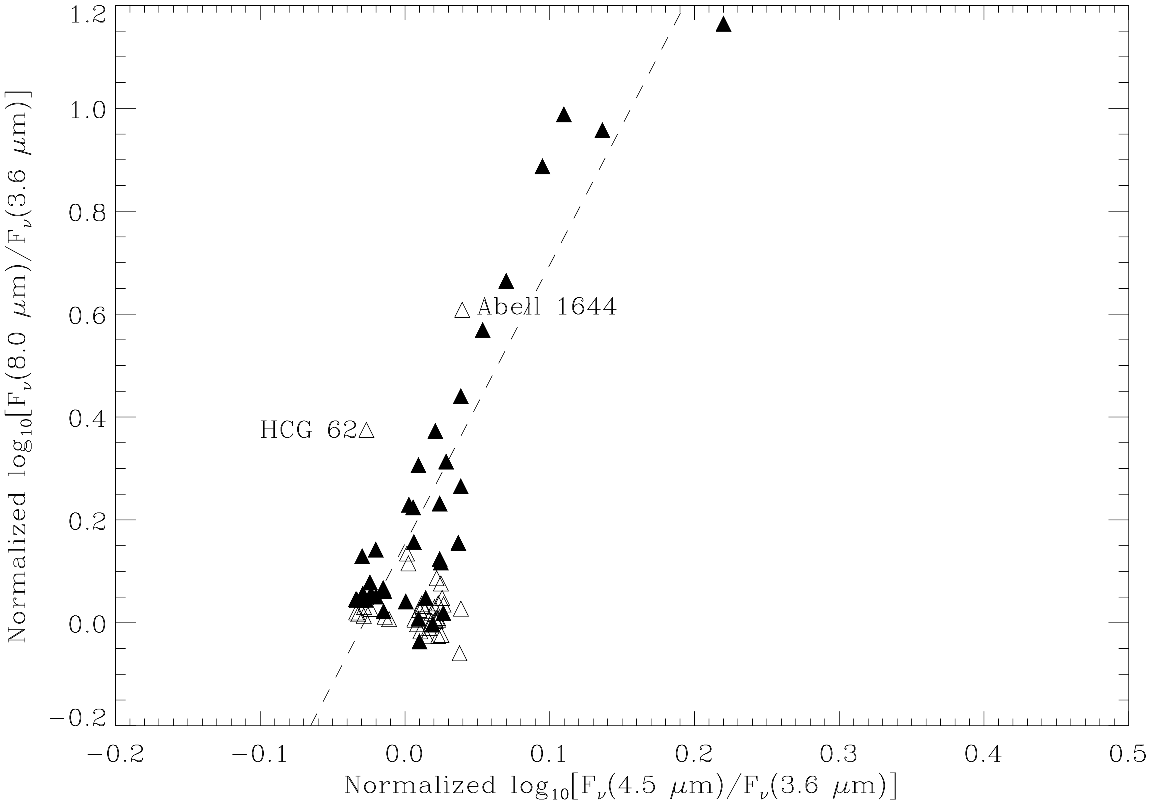

Figure 2.8 Infrared Ratio Correlation. 8.0 micron to 3.6 micron ratio and 4.5 micron to 3.6 micron ratio. Both ratios have been normalized for passive evolution. The 8.0/3.6 and the 4.5/3.6 ratios are strongly correlated ($r = 0.92(15\sigma)$ for objects with mid-IR detections and/or NUV-K excesses (shown as filled in triangles), which is expected if the excess 4.5 micron emission is generated by processes related to that producing the 8.0 micron emission. Dashed line is a fit to the data; see text. Abell 1644 and HCG 62 do not have blue NUV-K colors, HCG 62 is a 70 micron upper limit, and Abell 1644 wasn't observed by MIPS. Since these ratios use only IRAC data, the uncertainties in the absolute flux calibration are not included. As long as the IRAC calibration was consistent over time, these are precise relative flux ratios. The absolute flux ratios are accurate to about 2%.

be obscured star formation but also could be contributed by an AGN, by looking at the 24 micron to K-band (2.2 micron) flux ratio plotted against the central entropy in Figure 2.9. We note a similar pattern here as found in the UV excess plots (Figure 2.4), that the low K_0 galaxy clusters are far more likely to host BCGs with warm dust. The possible exception to this pattern is Abell 521, which is a high entropy cluster with an elevated 24 micron to K band flux ratio. However, as seen in Ferrari et al. [2006] there is a low entropy, compact, X-ray corona[Sun et al., 2007] (i.e. a "mini-cooling core") around the BCG in Abell 521, embedded in a cluster with otherwise high entropy. Excess 24 micron emission is estimated by determining the mean of the 24-K ratio of BCGs in high K_0 systems (excluding Abell 521) and any BCG with at least 1σ above this mean (0.063 ± 0.050) is considered to have excess 24 micron emission. We see that 43% of the cool cores in our sample have an excess in their 24 micron to K band ratio. The BCGs with the most extreme 24 micron to K band ratios are in ZwCl 0857.9+2107 and Cygnus A with a ratio of about 20. BCGs in Abell 426 and Abell 1068 also have large ratios around 10. All four objects likely have some AGN contribution. We see the scatter (i.e. standard deviation) in the ratio $\log_{10}(\mathrm{F}_{24\mu\mathrm{m}}/\mathrm{F}_{\mathrm{K}})$ is 0.81 for BCGs in low central entropy clusters.

We can compare IR ratios in BCGs to those of normal star-forming galaxies and starbursts, similar to Figure 1 in Johnson et al. [2007a]. The ratios for the BCGs are plotted in Figure 2.10 as well as the SINGS galaxies [Kennicutt et al., 2003]. Similar to their sample of a wide range of galaxies, the BCGs in our sample have the same colors as star-forming galaxies in SINGS. We note that some of the nearby BCGs have a higher ratio of 8 micron to 24 micron emission by a factor of 2. This ratio may indicate a relatively larger contribution from PAH emission over very warm dust. Also, this bandpass may include contributions from the S(4) transition of molecular hydrogen. Rotationally excited molecular hydrogen

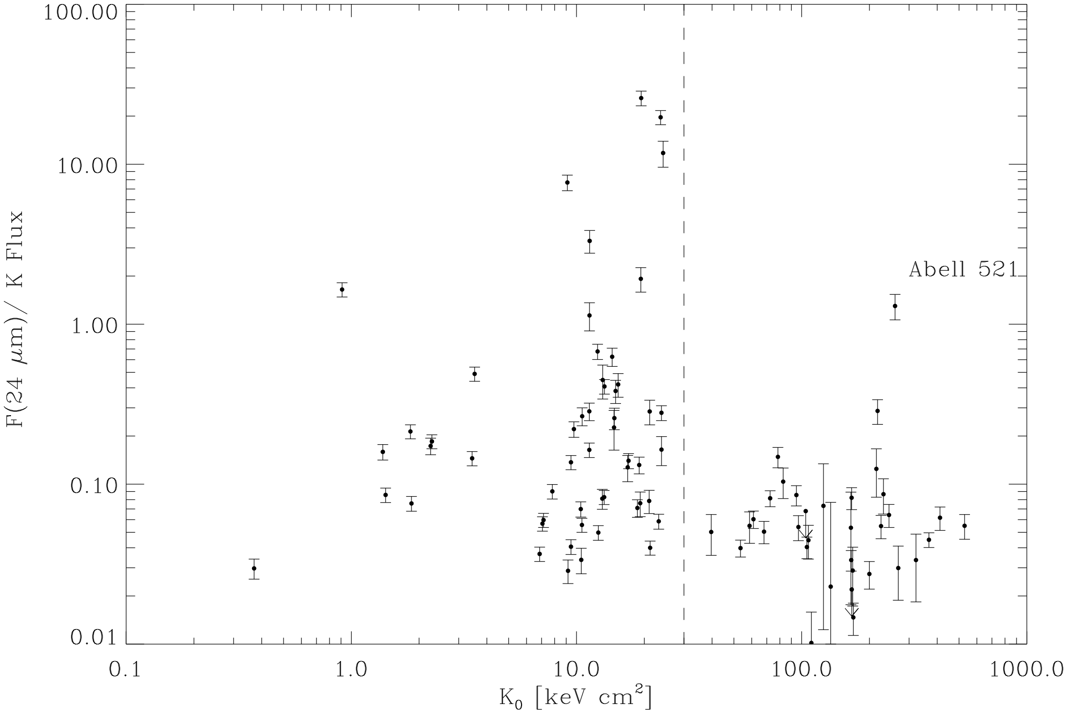

Figure 2.9 Mid-IR Color. 24 micron flux to K band flux ratio with central entropy of the cluster. BCGs with excess 24 micron flux inhabit clusters with low K_0, with the exception of Abell 521. Even though it is a high K$_0$ cluster, the BCG in Abell 521 is in a low entropy, compact, X-ray corona (i.e. a “mini-cooling core”) which can be associated with BCGs with radio sources and star-formation activity, like BCGs in low K$_0$ clusters of galaxies [Ferrari et al., 2006].

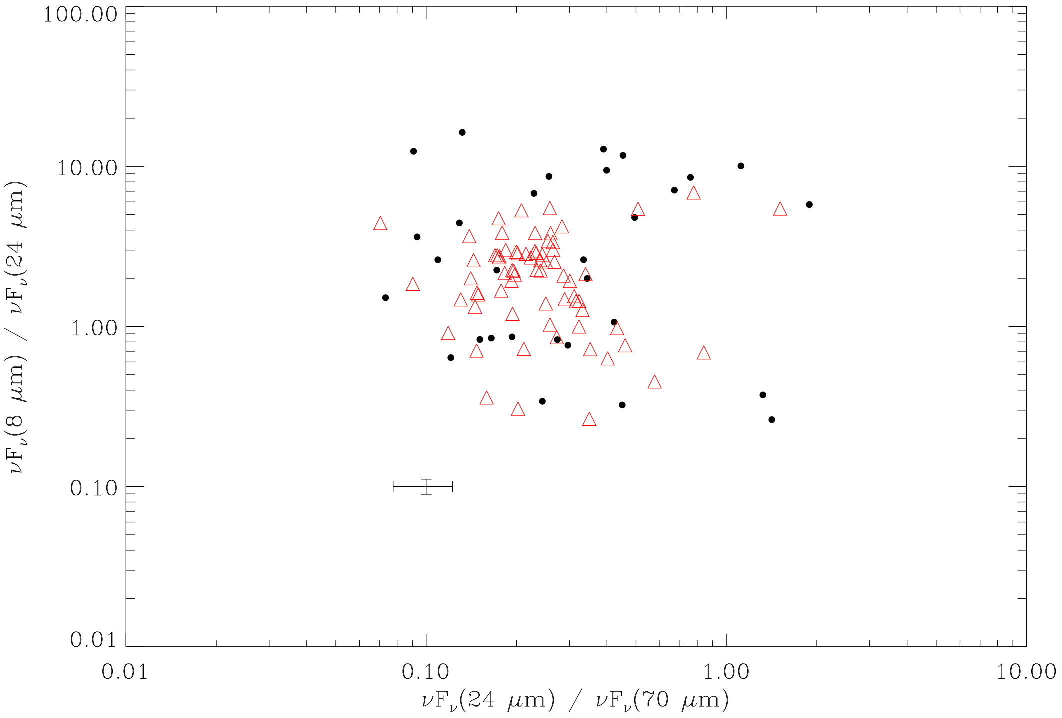

Figure 2.10 SINGS Galaxy Comparison. This plot is similar to Figure 1 in Johnson et al. [2007a]. The black dots are our BCGs and the SINGS galaxies [Kennicutt et al., 2003] are overplotted as red triangles. Ratios for objects with MIPS upper limits at 24 or 70 microns are not plotted but are consistent with the distribution of the detected galaxies. An error bar, representing the standard IRAC and MIPS systematic errors, is plotted to represent a typical error bar. Some nearby BCGs have slightly higher 8.0/24 micron flux ratios than SINGS galaxies, but similar 24/70 micron flux ratios.

lines are extremely luminous in some BCGs, and these same lines are not bright in star forming galaxies (Donahue et al. 2011). It is possible that some of the excess emission at the 8.0 micron may be contributed by molecular hydrogen.

2.4.3 Star Formation Rates (SFRs)

The UV color excess, Δ_c defined in § 2.4.1, can be used to estimate the excess UV luminosity due to unobscured star formation:

$$L_{SFR} = L_\nu(1 - 10^{-\Delta_c/2.5}), \tag{2.2}$$

where the specfic luminosity L_ν is converted from the NUV AB magnitude, corrected for Galactic extinction. The NUV k-correction for a star forming spectrum is negligible out to moderate redshifts [Hicks et al., 2010]. The unobscured star formation rate is then estimated from the relation in Kennicutt [1998] and listed in Table A.6. The total UV luminosity is estimated to be $L_{UV} \sim \nu L_\nu$ using $\nu = c/2267$Å. Upper limits are based on 3σ uncertainties in UV excesses.

The obscured star formation rate is estimated in two ways, (1) by fitting Groves et al. [2008] starburst models and a model of an old stellar population to the *2MASS* and *Spitzer* IRAC/MIPS infrared data points, and (2) from using calibrated conversions of IR luminosity (mostly 24 and 70 micron luminosities) to SFRs. In the first case, we present a sum of the two models, with independent normalizations. Star formation rates were determined for all BCGs with data from at least *2MASS* and the 24 μm band of MIPS. To estimate rest-frame IR luminosities based on the 24 and 70 micron fluxes, k-corrections were applied such that $L_{rest} = kL_{obs}$. The corrections were found using the best-fit Groves model for that individual galaxy and convolving it with the MIPS bandpass, both in the rest frame and the observed frame of the galaxy. The actual 70 micron corrections do not depend very much on the specific Groves starburst model. However,the 24 micron point usually falls around a minimum in the spectrum, which causes a larger scatter in the relation for a give redshift (up to 30%)

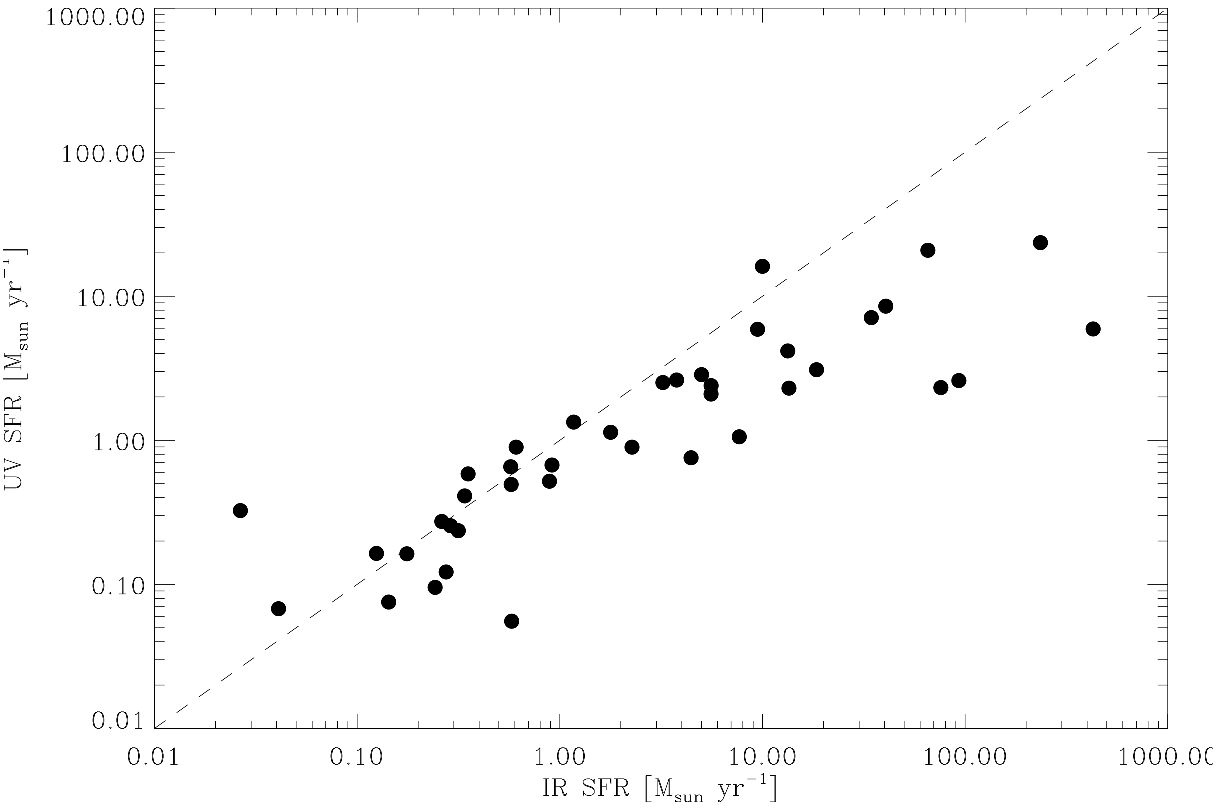

Figure 2.11 UV and IR SFR. The dotted line represents a line of unity. The UV SFR assumes a constant rate of star formation. The model-derived IR star formation rates are consistent with star formation rates measured with a MIPS 70 μm SFR estimate as shown in Figure 2.12. Those objects which fall below the line, BCGs with excess IR star formation, are similar to starburst galaxies, in the sense that for the most luminous star-forming galaxies, most of the star-formation is obscured.

The 24 micron k-corrections are in the range (0.125-1.056), the 70 micron k-corrections are in the range (0.738-1.879). The total IR luminosity, L_{dust}, is estimated by integrating the total scaled starburst model over $\lambda\lambda$8-1000μm. We plot the UV star formation rate against the IR star formation rate in Figure 2.11.

Calibrated conversions for star formation rates from 24 and 70 micron luminosities were used from Calzetti et al. [2010]. The 70 micron luminosity conversion to a SFR was from Equations (21) and (22) from this paper, depending on the luminosity of that galaxy. The 24 micron SFR relation was from Equation (6) which is from Wu et al. [2005]. From Figure 2.12

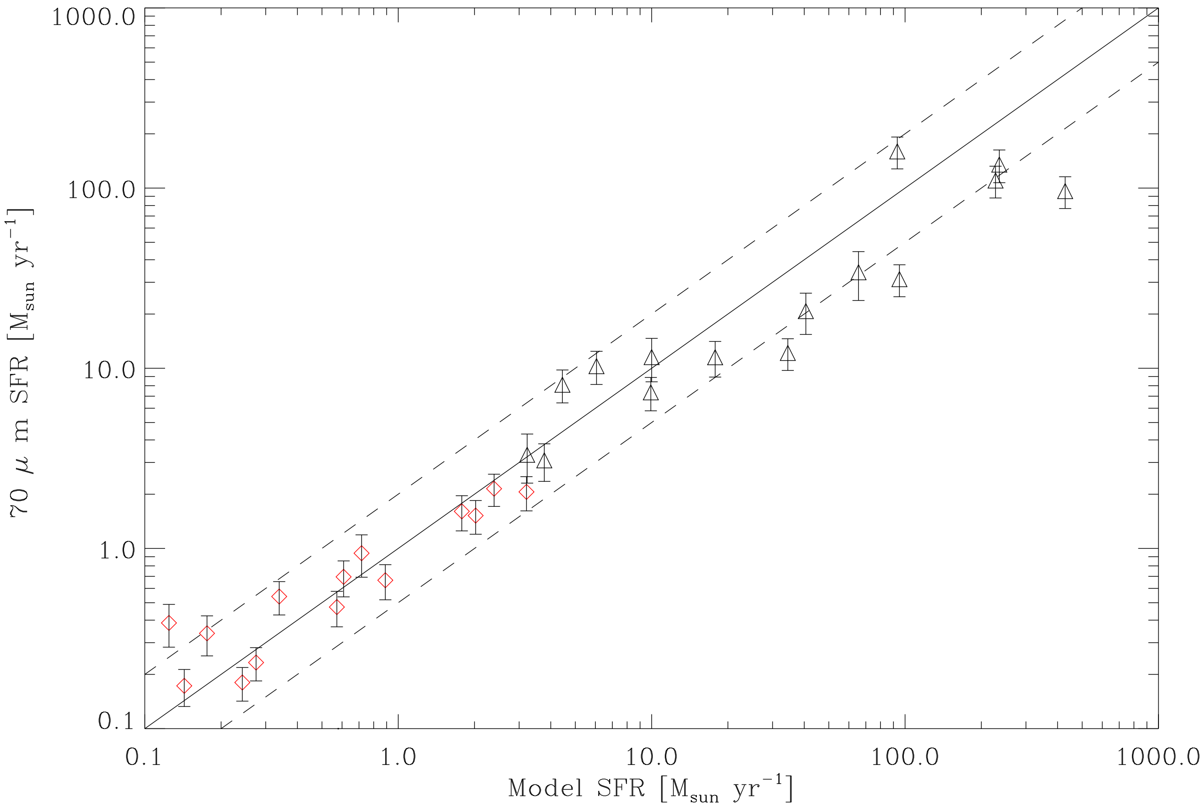

Figure 2.12 Comparison of model IR SFR to single band 70μm IR SFR. We compare the estimates from the Groves model star formation rates to the star formation rate estimates using the 70 micron luminosity in the left plot. The line represents a line of unity, not a fit. The dotted lines represent the boundary for a difference of a factor of two in star formation rate. The black triangles represent the high luminosity relation given in Calzetti et al. [2010] while the red diamonds use their relation for galaxies with low IR luminosities (and therefore a larger amount of the IR flux is produced by dust heated by evolved stars rather than hot stars).

and Figure 2.13 we have a comparison between these conversions and the model calibrated star formation rate. The 24 micron luminosity is not as good at predicting the bolometric IR luminosity (and the integrated star formation) because it does not sample as close to the cold dust mid-IR emission peak as the 70 micron luminosity. The 70 micron flux is much closer to the peak and is likely a better estimate of the IR luminosity and the obscured SFR.

We estimate the IR excess IRX $= \log_{10}(L_{\rm dust}/L_{\rm UV})$ and plot it against the $FUV - NUV$

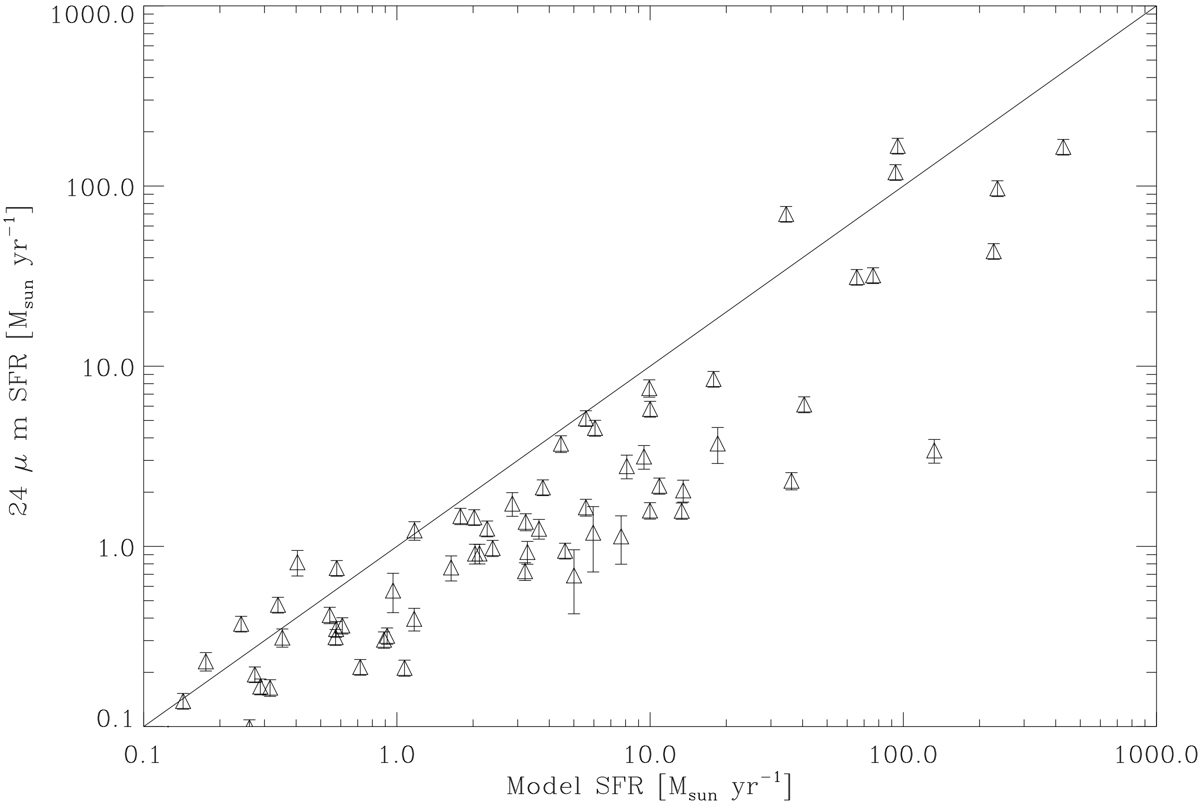

Figure 2.13 Comparison of model IR SFR to single band 24μm IR SFR. The plot is a similar plot to Figure 2.12 relating the 24 micron luminosity to the Groves model star formation rates. The 24 micron SFRs tend to have lower estimates as the 70 micron luminosities are found nearer to the peak of the dust blackbody and therefore more representative of the total IR luminosity and SFR. For the most luminous 70 microns galaxies, it appears that the model fit tends to overpredict the SFR and luminosity relative to the 70 micron flux estimate.

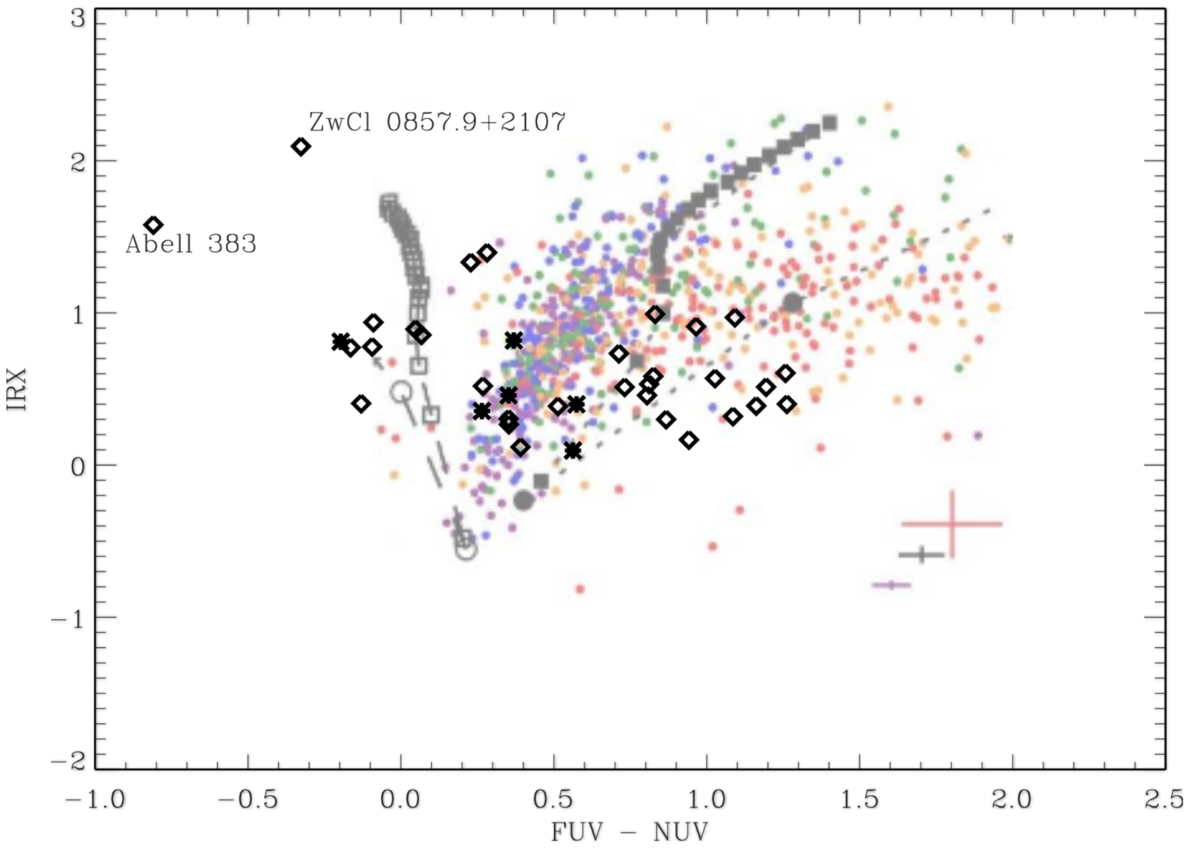

Figure 2.14 IR excess and UV color. The IR excess (IRX) is defined in Johnson et al. [2007a] to be the ratio of IR to UV luminosity. Objects from the cool core sample of Hicks et al. [2010] are marked with X's. Figure 6a from Johnson et al. [2007a] is plotted in the background on this graph.

color (Figure 2.14), similar to Figure 6 in the Johnson et al. [2007a] paper, which presents UV and IR data for a sample of star-forming disk galaxies and starburst galaxies. In an earlier comparison of BCGs with star-forming galaxies, Hicks et al. [2010] found that the cool core BCGs in their sample tended to be bluer in UV color and have a large scatter in IRX compared to those properties in the galaxies in Johnson et al. [2007a]. We do see the larger scatter in IRX for those BCGs that have a bluer UV color. We note that most of the BCGs in our plot are found in low central entropy clusters because those are the only BCGs with FUV, NUV, and *Spitzer* mid-IR detections.

2.4.4 Star Formation and Cluster Entropy Profiles

We have shown here and in previous works [e.g., Cavagnolo et al., 2008b, 2009, Rafferty et al., 2008], that BCGs in clusters with low central entropy (K_0) are the only BCGs to exhibit signs of vigorous star formation. The upper threshold for activity in BCGs appears to be around 30 keV cm^2. Table 2.1 presents the subsamples with excess emission. We investigate here to see whether the strength of the signatures of activity, the UV and mid-IR excess, exhibited any trend with the central entropy floor or other cluster property.

Here we take the derived star formation rates as simply indicative of the level of star formation activity. By assuming the star formation is constant, we have taken a nominal assumption about the conversion factors and the starburst models, and translated luminosities into SFRs. We are not claiming that the star formation is continuous. Distinctions between continuous star formations, simple single-burst models of a single age, and convolutions of more complicated star formation histories are well beyond the scope of broad-band photometric data and global measurements. For example, extremely recent star formation is best tracked with Hα, but the Hα fluxes available from the literature are typically from long-slit spectra, and therefore can underestimate emission line flux if some of it is located outside the central $2''$ or so. Hα can also be affected by dust extinction in heavily obscured regions; Hα can be produced by mechanisms other than by recombination in star formation regions. Mid-IR emission provides a pretty reliable assessment of the obscured star formation energy output, since it is like a bolometric measure of luminosity emitted by dust. At low star formation rates, the colder dust, heated by evolved stars can contribute to the longer wavelength emission, so the lowest IR SFRs in our sample (below about 0.1 solar masses per year) may be regarded as upper limits. The UV light from a galaxy is very sensitive to the presence of hot stars if some of their light escapes the galaxy. We do not attempt to correct the UV light for internal extinction, so the UV and the mid-IR are sampling complementary components of any star formation-related light.

A sum of the UV and IR SFRs is therefore a best estimate of something akin to the total star formation rate of the BCG, and even the most conservative interpretation is that they indicate the current luminosity of star formation in the BCG. We do not see any correlation between the entropy profile and the strength of star formation signatures (e.g. the UV or the mid-IR luminosities of the BCGs with various X-ray gas quantities, K_0 or the value of the entropy profile at 20 kpc ($K(r = 20 \text{ kpc})$)). In Figure 2.15 we plot the quantities of SFR and K_0. Upon first glance, there may seem to be a trend for the detected lowest entropy systems to have the lowest star-formation luminosities. However, these are lowest redshift groups in the ACCEPT sample, with lower luminosities and masses overall. They are quite nearby, so the ones that are well-observed by Chandra have entropy profiles that probe the sub kpc-scales. Excluding the groups (or including the upper limits for BCGs in groups without evidence for star formation activity) erases any semblance of a trend. To test that we were not missing a trend because the best fit K_0 could be biased high for the more distant clusters (see Cavagnolo et al 2009), we plot K_0 and SFR for the BCGs with z between 0.05 and 0.15. In this subsample, no trend is visible. Furthermore, the expected trend would be that the lowest entropy systems would have the largest star formation luminosities because the gas has the shortest detected cooling times. Therefore we see no evidence for a simple relation between central gas entropy or cooling time and the estimated SFR.

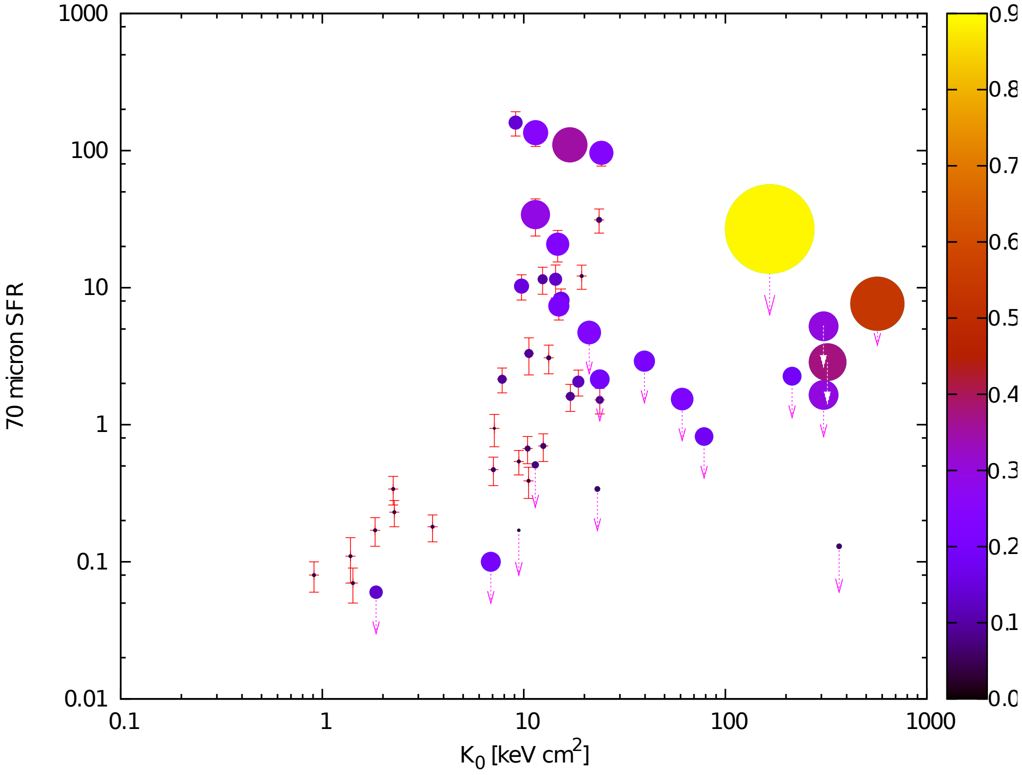

Figure 2.15 Relation between 70 micron SFR and central entropy. The objects are color coded and sized based on redshift (i.e. higher redshift, larger size). The color code ranges from redshift of 0.0 to 0.9. The "trend" that is seen in the lowest central entropy clusters is not a physical trend, but it is the same selection effect noted in Figure 2.4. Note that all BCGs in clusters with $K_0 > 30$ keV cm^2 in this plot have only upper limits.

2.4.5 ICM Gas Cooling and Star Formation in BCGs

While the presence of high density, high pressure intracluster gas seems to be a prerequisite for a BCG to host some star formation, role of the intracluster gas is not quite clear. The current paradigm suggests that some of the hot gas cools and forms stars, but a gas that has been at X-ray temperatures for some time has likely sputtered away any grains it may have had. The lifetime of a typical Galactic dust grain in 10^7 K gas is of order 10 million years [Draine and Salpeter, 1979]. Dust-free gas forms molecular hydrogen only very slowly [e.g., Bromm et al., 2009]. Voit and Donahue [2011] show that for BCGs with measured reservoirs of CO (and H_2), the gas residence time ($= M(H_2)/SFR$) for BCGs is very similar to that of star-forming disk galaxies at SFR$<$ 10 $M_\odot$ yr^{-1}, around a Gyr. For BCGs with rapid SFRs, the residence time is similar to that of starbursts with similar SFRs ($\sim 10^7 - 10^8$ yrs). They calculate that if much of the stellar winds and ejecta of evolved stars in the BCG are retained by the BCG, perhaps as a consequence of the higher intracluster pressures, this gas could fuel much of the existing star formation occuring at a steady rate. Certainly for BCGs with SFR$\sim$ 10 solar masses per year or less, the stellar ejecta is a source of material that has mass of similar order of magnitude to any source of cooled ICM gas.

However, for galaxies with gas reservoirs of 10^{10} solar masses or more, cooled ICM appears to be required to supply the molecular clouds. The stellar ejecta or contributions from the ISM of dusty galaxies [e.g. Sparks et al., 1989b] may provide dusty seeds that may mix with the ICM and significantly accelerate its cooling. The larger SFRs cannot be sustained at a steady rate, given the gas supply, and just as in starburst galaxies, must be a short-term situation. The gas may accumulate over a longer period. Given that $\sim 1/3$ of low redshift cool core galaxies exhibit Hα, a similar fraction of cool core BCGs (or possibly fewer, if some of the Hα emission is not related to SF) are in the star-forming state. Therefore, such galaxies could accumulate the ejecta of their stellar inhabitants into molecular clouds for Gigayears, then experience a burst once a threshold surface density of molecular hydrogen was achieved.

The empirical correlation between the presence low-entropy ICM and the star formation in the central BCG is incontrovertible. However, the common interpretation of this correlation that cooled ICM fuels the star formation has not been backed up by a physically plausible theory for how the hot ICM cools and makes cold and dusty molecular clouds. The resident stellar population is an obvious source of dust (and cool gas) that should not be neglected.

2.5 Conclusions

We present photometry for brightest cluster galaxies in the ACCEPT cluster sample, derived from *GALEX*, *Spitzer*, and *2MASS* archival observations. This sample includes 239 clusters which were well-observed by Chandra up until late 2008, with hot gas entropy profiles uniformly extracted [Cavagnolo et al., 2009]. We identified the BCGs in all of the clusters. In our BCG identification, it is twice as likely to be within 10 projected kpc of its X-ray centroid in low entropy clusters (74%) compared to high entropy clusters (37%).

Similar to what has been seen in other star formation indicators (e.g. Hα), galaxy clusters with low central gas entropies (also known as "cool core" clusters) are the only clusters to host BCGs with infrared and UV excesses above those from the old stellar population. The entropy threshold of 30 keV cm^2 is consistent with the entropy threshold identified by other work [Cavagnolo et al., 2008b, Rafferty et al., 2008, Cavagnolo et al., 2009]. We found 168 observations by the near UV imaging by *GALEX*, of which 112 BCGs were detected. We found a mean NUV-K (6.59±0.34) color seen in quiescent BCGs and use that to quantify excess UV emission in individual BCGs. Of the 84 clusters with low central gas entropy , 32 (38%) hosted BCGs with a UV excess, while none of the clusters with high central gas entropy did. The scatter (i.e. standard deviation) in the NUV-K AB color of BCGs in low entropy clusters is considerably higher at 0.99. We did not detect a difference between the mean UV color (FUV-NUV) of BCGs (not including those with possible Lyα contamination), within the error, for low and high entropy clusters.

Similarly, we detected excess infrared emission in some BCGs in low gas entropy clusters over a large range of infrared bands (e.g. 4.5, 8.0, 24, and 70 microns) and no excess in BCGs in high central entropy clusters. The mid-IR emission ratios for BCGs (including quiescent BCGs with mid-IR detections) are consistent with, and span a similar range to, galaxies studied in the Sloan Digital Sky Survey (SDSS) galaxies with a range of star forming properties by Johnson et al. [2007b]. For example, 24 of the obeserved 56 BCGs (43%) in low entropy clusters show excess 24 micron to K band emission. The standard deviation of the ratio $\log_{10}(\mathrm{F}_{24\mu\mathrm{m}}/\mathrm{F}_{\mathrm{K}})$ is 0.81 in these BCGs. We also see a strong correlation between excess 4.5 micron and 8.0 micron fluxes that may indicate correlated PAH emission in both of these bands, when the PAH emission is strong.

The excess emission seen in the UV can be used in conjunction with the IR emission to estimate a total star formation rate, accounting for both obscured and unobscured star formation. The UV and IR estimates give complementary information whereas Hα may be affected by contaminating contributions from other sources (e.g. dust extinction, shocks) or limited by technique (e.g. incomplete spatial coverage in long slit spectroscopy, contamination by N II in narrow band imaging). Additionally, the multi-wavelength coverage (as opposed to single band measurements) can help to further constrain possible sources of the excess emission. We see that the near-IR to far-IR emission is consistent with a combination of a starburst model and an old stellar population. Clear signs of these empirical correlations and significant dust emission in some low entropy clusters can help constrain star formation estimates in these BCGs. Aside from the previously noted upper threshold for activity at $K_0 = 30\text{keV cm}^2$, we do not detect a correlation between the level of luminosities or excesses with K_0 (or equivalently, central cooling time.) However, whether the gas fueling this activity comes from cooling of the ICM or other processes, is not so clear. A significant, massive evolved stellar population in these galaxies may produce dusty gas which may be confined by the hot gas and it may provide the seeds of condensation for the gas from the hot, and presumably dust-free, intracluster medium [Voit and Donahue, 2011].

Support for this research was provided by *Spitzer* contracts JPL RSA 1377112 (MSU RC065166) and JPL 1353923 (MSU RC065195). M. Donahue and A. Hicks were partially supported by a Long Term Space Astrophysics grant NASA NNG05GD82G (MSU RC062757). We would also like to thank Deborah Haarsma and Luke Leisman for their helpful discussion on BCG identification and Mark Voit for his comments on the text. This research has made use of the SIMBAD database, operated at CDS, Strasbourg, France. This research has made use of the NASA/IPAC Extragalactic Database (NED) which is operated by the Jet Propulsion Laboratory, California Institute of Technology, under contract with the National Aeronautics and Space Administration.

Chapter 3

Multiwavelength Study of the Extremely Cool Core Cluster RXJ 2014.8-2430

We present X-ray and Southern Astrophysical Research (SOAR) Telescope spectroscopic and narrow-band imaging for the most extreme cool-core cluster in the Representative XMM-*Newton* Cluster Structure Survey. Surprisingly, the *Chandra* imaging observations did not reveal bi-lateral X-ray cavities one might expect to see in an extreme cool core with a powerful radio source; cavities that commonly appear in other similar sources. We discuss the limits on the properties of a putative radio bubble associated with any undetected X-ray cavities. We place limits on any significant X-ray point source in the brightest cluster galaxy (BCG) where the X-ray peak is offset from central radio source. The data are consistent with a possible cavity system along the line of sight to the center of the cluster or with a possible sloshing signature. These observations lead us to conclude that either we are seeing a young radio source in a short-lived phase of activity or the radio source and its cavities in the X-ray gas are nearly aligned along the line of sight. The imaging and spectroscopy of SOAR reveal an extended, luminous optical emission line source. From our narrow band Hα imaging of the BCG, the central Hα peak is slightly offset from the *Chandra* data, consistent with a

sloshing hypothesis. However, we argue that any sloshing must be rather gentle in nature given the co-location of the Hα and stellar emission peak, the concentration of the X-ray emission peak and the distribution of metals.

3.1 Introduction

The first evidence that a radio AGN could disturb the X-ray atmosphere of clusters of galaxies was seen with the High Resolution Imager on board ROSAT [Boehringer et al., 1993], in a historic observation of the Perseus cluster. This image showed two depressions in the X-ray surface brightness map, bracketing the central AGN. Early *Chandra* observations of nearby clusters revealed similar patterns of cavities around radio sources in brightest cluster galaxies (BCGs) [McNamara et al., 2000, 2001]. These cavities have generally been found to be filled with radio emission, though often it is too faint to be detected in shallow radio surveys and other short observations at 1.4 GHz [Bîrzan et al., 2012]. Long-wavelength radio observations and deeper observations of the Perseus cluster by Fabian et al. [2000] revealed older and larger cavities farther out in the cluster, filled by low-frequency radio emission presumably from an aging population of relativistic electrons.

Previous to these observations, astronomers had assumed that the rate of kinetic energy emerging from radio AGN would be similar to their radiative luminosities, that is, low. The assumption that there was no source of energy to counterbalance the prodigious release of radiative energy from the gas led to the notion of a "cooling flow", where the entire gas atmosphere slowly compresses [Fabian and Nulsen, 1977, Cowie and Binney, 1977, Fabian, 1994b]. The lack of huge reservoirs of cold gas and the constraints on star formation rates at least an order of magnitude lower than the cooling flow rate put the simple cooling flow model into doubt. The door was closed on this model by high resolution spectroscopy made by the Reflection Grating Spectrograph on board the *Newton* X-ray Multi Mirror (XMM) telescope [Peterson et al., 2003]. These observations showed that the strong X-ray emission lines from gas around 10^7 K ($\sim$0.9 keV) predicted by the simple cooling flow model were not present at their predicted strength.

Nevertheless, the problem remained: how can the gas radiate so brightly and so commonly (about half of all X-ray luminous clusters have cool cores)? The discovery of cavities commonly associated with AGN in the atmospheres of cool cores posed a "smoking-gun" answer. This scenario was bolstered by the discovery that the size of the cavity and the X-ray gas pressure confining the cavity were consistent with the energy lost by the cluster cooling core, using the buoyant rise time as the relevant time scale [McNamara et al., 2005, McNamara and Nulsen, 2007, Bîrzan et al., 2008]. To prevent the ICM in a cool core from catastrophically cooling it is possible for the central supermassive black hole of the brightest cluster galaxy (BCG) in its active galactic nucleus (AGN) phase to quench cooling [e.g Binney and Tabor, 1995, Churazov et al., 2001]. The AGN might accomplish this heating through the creation of X-ray cavities ("bubbles") which buoyantly rise from the cluster center (e.g. Brüggen [2003], Brüggen and Kaiser [2002]). Bîrzan et al. [2004] found a strong correlation of AGN jet power with the X-ray cooling rate in clusters and groups, with some scatter. This correlation suggests that mechanical energies from X-ray cavities are in the range of $1pV$ to $16pV$ per cavity in order to quench the cooling suggested by the central entropy of the cluster. The correlation between AGN jet power and X-ray luminosity suggests that radio bubble formation scales strongly with the amount of cooling.

The emission-line nebulae associated with these cool cores provide another diagnostic for the physical processes occurring there. The origin of the gas in these dusty, optically-luminous filaments is not clear [Voit and Donahue, 2011], and the processes that excite the optical emission are similarly mysterious. For some filaments, photoionization by hot stars may well be the dominant source of excitation, but some additional source of heat might be required to explain the brightest forbidden line emission simultaneously with the lack of He II recombination lines [Voit and Donahue, 1997, Donahue and Voit, 2004, Ferland et al., 2009, Sparks et al., 2009, Werner et al., 2013]. Nevertheless, the emission line nebulae are providing significant clues to unlocking the cool core mystery: they only appear in clusters with cool cores, that is, clusters with low central gas entropy, short cooling times [Cavagnolo et al., 2009] Cool core cluster nebula extend up to 70 kpc from the cluster core [e.g. McNamara et al., 1996]. Typically, the morphology of the BCG's Hα correlates well with the morphology seen in the soft (< 1 keV) X-ray emission [e.g. Sparks et al., 2004, Fabian et al., 2006, Werner et al., 2010].

In this paper we present observations taken with the *Chandra* X-ray Observatory and the Southern Astrophysical Research (SOAR) telescope of the galaxy cluster RXJ 2014.8-2430 (RXJ 2014.8-2430), which is the strongest cool core clusters in REXCESS. The REXCESS sample [Böhringer et al., 2007b] is a representative z$\sim$0.1 sample of 31 clusters spanning a wide range in luminosity, mass, and temperature. It was designed to avoid bias in X-ray morphology or central surface brightness. These observations were followed up with a short (20 ks) *Chandra* observation to complement the XMM data by studying the cluster core with arcsecond resolution. From the XMM data, Croston et al. [2008] find RXJ 2014.8-2430 is strongly peaked and has the shortest central cooling time (computed within 0.03r_{500}) of the sample at 0.550 ± 0.026 Gyr and is 15% shorter than the central cooling time for the next coolest cluster. Donahue et al. [2010] determined an Hα luminosity of 6.4×10^{41} h_{70}^{-2} erg s^{-1}), which is twice as large as that of any other cluster in REXCESS. Additionally, it has a moderate (in relation to other REXCESS clusters with radio sources) radio source in the center [Condon et al., 1998] and its minimum star formation rate based on UV XMM optical monitor data uncorrected for dust extinction is 8-14 $M_{\odot}$ yr^{-1} [Donahue et al., 2010].

For all calculations, the assumed cosmology is $H_0 = 70$ km s^{-1} Mpc^{-1}, $\Omega_M = 0.3$, $\Omega_\Lambda = 0.7$. Pratt et al. [2009b] obtained a redshift estimate of RXJ 2014.8-2430 from its X-ray spectra, $z = 0.1538$ with no uncertainty reported. We use the redshift determined from optical spectroscopy, z = 0.1555 ± 0.0003, by Donahue et al. [2010]. Using that updated redshift, the angular scale is 2.694 kpc/$''$ and the luminosity distance is 741.8 Mpc [Wright, 2006].

Table 3.1. Observations

Telescope	Filter	Exposure	Date	ID	PI
SOAR/SOI	CTIO 7580/85	3×1200s	2010 September 6th		Donahue
	CTIO 7384/84	3×720s			
SOAR/Goodman	600 l/mm grating	3×1200s	2012 July 25th		Donahue
		3×1200s			
Chandra/ACIS-S		20 ks	2009 August 25th	11757	Donahue
XMM/MOS1+MOS2		26.7 ks	2004 October 8th	201902201	Boehringer

Note. — Summary of observations used in this work.

3.2 Observations and Data Reduction

3.2.1 Chandra X-ray Observation

The 20 ksec *Chandra* observation of RXJ 2014.8-2430 was taken on August 25, 2009 (ObsID 11757) as part of the *Chandra* Guest Observers program. Observation details are listed in Table 3.1. Observations were taken with the *Chandra* Advanced CCD Imaging Spectrometer centered on the back-illuminated ACIS-S3 chip in VFAINT mode. The data were reprocessed with CALDB 4.4.6 and CIAO 4.3. We used deep background files scaled to match the high energy (9.5-12.0 keV) background count rate measured in a large source-free region in the data [Hickox and Markevitch, 2006]. Point sources around the cluster were identified by hand and removed. To estimate the centroid, we used the procedure from Cavagnolo et al. [2008a] and with a relaxed cool-core cluster with a slight asymmetry in the cluster core, this method determined an X-ray peak that is coincident with the peak pixel ($0.492'' \times 0.492''$) in the clean and point source-subtracted image. The X-ray center is RA $20^h 14^m 51.65^s$, Dec $-24^d 30^m 21.1^s$.

We fit a 2×2 binned cluster 0.5-7.0 keV flux map with elliptical profiles using the *ellipse* [Jedrzejewski, 1987] function in IRAF [Tody, 1993]. We estimated the centroid shift $w = \frac{1}{R_{max}} \times \sqrt{\frac{\Sigma(\Delta_i - <\Delta>)^2}{N-1}}$ where N is the total number of apertures considered and Δ_i is the separation of the centroids computed within R_{max} and within the i^{th} aperture. Using our elliptical profile fit, our centroid shift parameter $w = 0.018 \pm 0.508$, is statistically consistent with no centriod shift. For comparison, Maughan et al. [2012] chose $w = 0.006$ (with respect to R_{500}) to separate relaxed from unrelaxed clusters in their sample of 114 clusters with *Chandra* ACIS-I observations. This centroid shift cut was found to distinguish well the cool-core (CC) from non-CC clusters, with only 3 CC clusters in their sample having $w > 0.006$.

For our ellipse fit, the R_{max} is 74 kpc, much smaller than the cluster's R_{500} measured by XMM.

To search for structure, we constructed an unsharp masked image using the same process as Randall et al. [2009] where we took the exposure-corrected 2×2 binned broadband image of the cluster, smoothed it by a one pixel ($0.98''$) Gaussian, and divided that by the same image smoothed by a ten pixel ($9.8''$) Gaussian. The unsharp masked image, seen in Figure 3.1, shows a clear decrement of a spiral structure around cluster center and an excess at the cluster center with no obvious X-ray cavities.

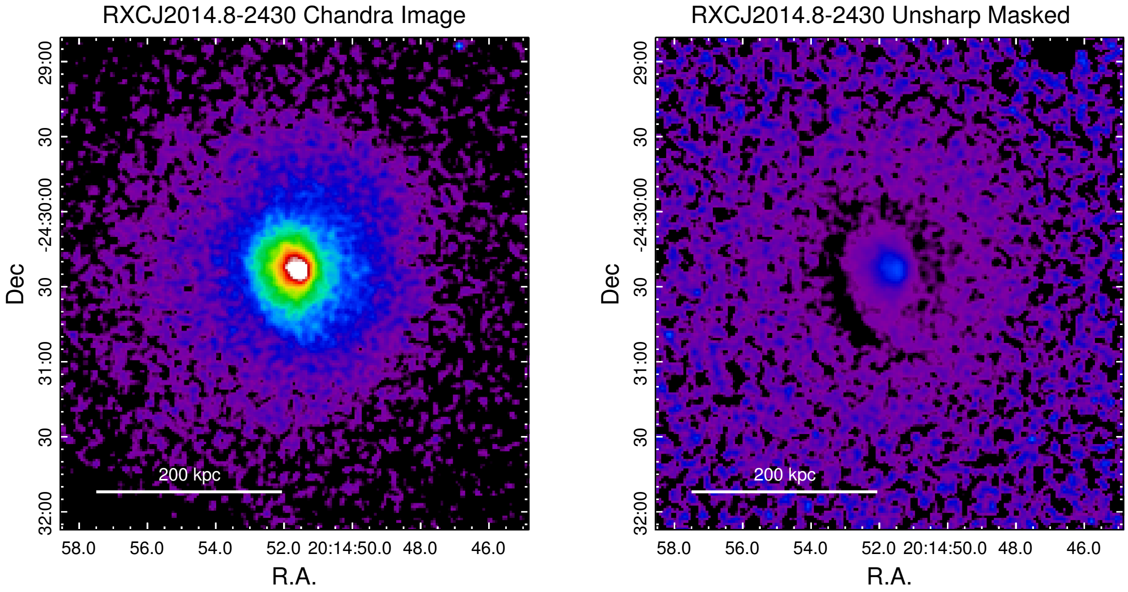

Figure 3.1 X-ray Image of Cluster. **Left:** *Chandra* X-ray image of RXJ 2014.8-2430 shown on a square root scale, roughly following projected density. Right is west and north is up. **Right:** Unsharp masked X-ray image of RXJ 2014.8-2430 shown on the same scale as the image on left.

We fit a 2D elliptical β model profile,

$$I(r) = I_0 \left(1 + \frac{r}{r_0}\right)^{3\beta - 0.5} \tag{3.1}$$

from the 2×2 binned image filtered on the energy range 0.5-7.0 keV. The model was fit in Sherpa and we allowed all the parameters, including the center, to vary; fitting the model with the Cash statistic. The parameters for the 2D β model fit (with 1σ errors) are: r_0=5.53″ ± 0.08″, I_0=83.5 ± 1.6 counts pixel^{-2}, ellipticity of 0.098 ± 0.006, β=0.998 ± 0.002 . The position angle of the major axis of the ellipse points directly north at -0.8° ± 1.7°. The major axis angle is equivalent to a 0° position angle for the IRAF ellipse fit, which agrees over most of the cluster. We use the residual image to look for any additional deviations from a smooth β model profile.

X-ray spectra were extracted using *specextract* in the energy range 0.3-11.0 keV over annuli centered at the X-ray peak with at least 2500 counts. Analysis is restricted to the ACIS-S2 and ACIS-S3 chips. We used the Mewe-Kaastra-Liedahl (MEKAL) model [Mewe et al., 1985, 1986, Kaastra and Mewe, 1993, Liedahl et al., 1995] for hot, X-ray emitting plasmas, highly ionized, in thermal and ionization equilibrium to find the temperature and metal abundance in XSPEC 12.6.0 [Arnaud, 1996]. For concentric annuli, the metallicity parameter for the central bin is independent and all subsequent metallicity parameters are tied across pairs of consecutive annuli. For all spectral fits, the Galactic foreground extinction is fixed at $N_H = 7.4\times10^{20}$ cm^{-2} from Dickey and Lockman [1990]. The Galactic foreground column density as well as the Grevesse and Sauval [1998] relative solar abundances are fixed parameters for the PHABS model used for Galactic extinction. We fit the unbinned spectral data with the Cash statistics [Cash, 1979] implementation in Xspec (modified c-stat).

We fit the projected temperature and metallicity of the annuli and the resultant temperature, deprojected electron density profile, pressure profile, and entropy profile. In this procedure we have made the approximation that the projected temperature is approximately equal to the deprojected temperature. We calculate the cluster entropy from the temperature and density profiles, then use the functional form from Donahue et al. [2006], K(r) = K_0 + K_{100}(r/100 kpc)$^{\alpha}$, to fit the entropy profile. The central entropy, K_0, found for the cluster RXJ 2014.8-2430 is 11.6 +/- 3.9 keV cm^2, K_{100} = 159.0 ± 57.2, and $\alpha = 1.284 \pm 0.002$ (χ^2_{red} = 0.725). In additon to extracting annuli, we also extracted and fit X-ray spectra of regions on and off of the Hα filaments. The counts, temperatues, and metallicities for the X-ray regions overlapping the Hα regions are shown in Table 3.2.

Table 3.2. Hα region X-ray Boxes

Region (—)	RA (—)	Dec (—)	Box Size (arcsec^2)	Net Counts (—)	T$_X$ (keV)	Metallicity (—)
Hα center	$20^h14^m51.610^s$	$-24^d30^m21.24^s$	20.00	1204	$3.51^{+0.45}_{-0.37}$	$0.91^{+0.57}_{-0.41}$
Hα offcenter 1	$20^h14^m51.820^s$	$-24^d30^m18.51^s$	30.96	1433	$4.15^{+0.64}_{-0.49}$	$0.37^{+0.39}_{-0.29}$
Hα offcenter 2	$20^h14^m51.364^s$	$-24^d30^m24.63^s$	39.26	1962	$3.21^{+0.29}_{-0.26}$	$1.10^{+0.46}_{-0.35}$
Off Hα 1	$20^h14^m51.391^s$	$-24^d30^m16.39^s$	28.26	747	$4.04^{+0.87}_{-0.64}$	$0.36^{+0.49}_{-0.31}$
Off Hα 2	$20^h14^m51.791^s$	$-24^d30^m26.81^s$	41.10	1861	$4.81^{+0.73}_{-0.57}$	$0.50^{+0.42}_{-0.33}$
Off Hα 1+2 tied	—	—	69.37	2608	$4.45^{+0.48}_{-0.41}$	$0.47^{+0.27}_{-0.21}$
Offcenter Hα 1+2 tied	—	—	70.22	3395	$3.63^{+0.26}_{-0.25}$	$0.98^{+0.32}_{-0.28}$
Offcenter Hα 1+2+center tied	—	—	90.22	4599	$3.65^{+0.23}_{-0.20}$	$1.13^{+0.29}_{-0.25}$

We used the same procedures of Donahue et al. [2014] to fit the cluster with the Joint Analysis of Cluster Observations (JACO) [Mahdavi et al., 2007, 2013]. From the JACO fits, the XMM parameters are: M_{2500}=1.76 ± 0.05 $\times 10^{14}$ $M_{\odot}$, c_{2500}=4.8 ± 0.15, $fgas_{2500}$=0.126 ± 0.002, r_{2500}=473 ± 5 kpc, r_{500}=0.94 ± 0.01 Mpc. The Chandra parameters are: M_{2500}=3.0 ± 0.2 $\times 10^{14}$ $M_{\odot}$, c_{2500}=2.3 ± 0.13, $fgas_{2500}$=0.098 ± 0.003, r_{2500}=564 ± 11 kpc; r_{500}=1.19 ± 0.03 Mpc. The radial profiles for temperature, electron pressure, entropy, and electron density are presented in Figure 3.2. The radial profile for the metallicity is presented in Figure 3.3. Uncertainties listed are 1σ (68%), statistical only, errors. We note that the JACO-Chandra HSE mass estimate for r_{500} is somewhat closer to the r_{500} of 1.15 Mpc estimated for this cluster by Pratt et al. [2009a] assuming the M_{500}-Y_X relation from Arnaud et al. [2007]. The data are binned by 25 counts per energy bin and χ^2 minimization statistic is used for the JACO fit. There are 24 radial bins for *Chandra* and 35 radial bins for XMM. JACO doesn't deproject in the classic sense, it forward-models, that is it assumes a 3-d parametric mass model, and, separately, fits a non-parametric model of concentric shells of constant-T and density gas, then projects the predicted spectra in rings of concentric annuli [Mahdavi et al., 2007, 2013].

3.2.2 SOAR Hα Imaging and Spectra

Narrow band optical imaging was taken on the Southern Astrophysical Research (SOAR) Telescope with the SOAR Optical Imager (SOI) [Walker et al., 2003] on September 6, 2010. A series of three exposures each with an exposure time of 1200 seconds was taken with the narrow band filter (7580/85) that was centered on the redshifted Hα (7572 Å). A second set of three exposures of 720 seconds each was taken with a narrow band continuum filter (7384/84) to determine continuum emission contribution to the "on band" image. We flux

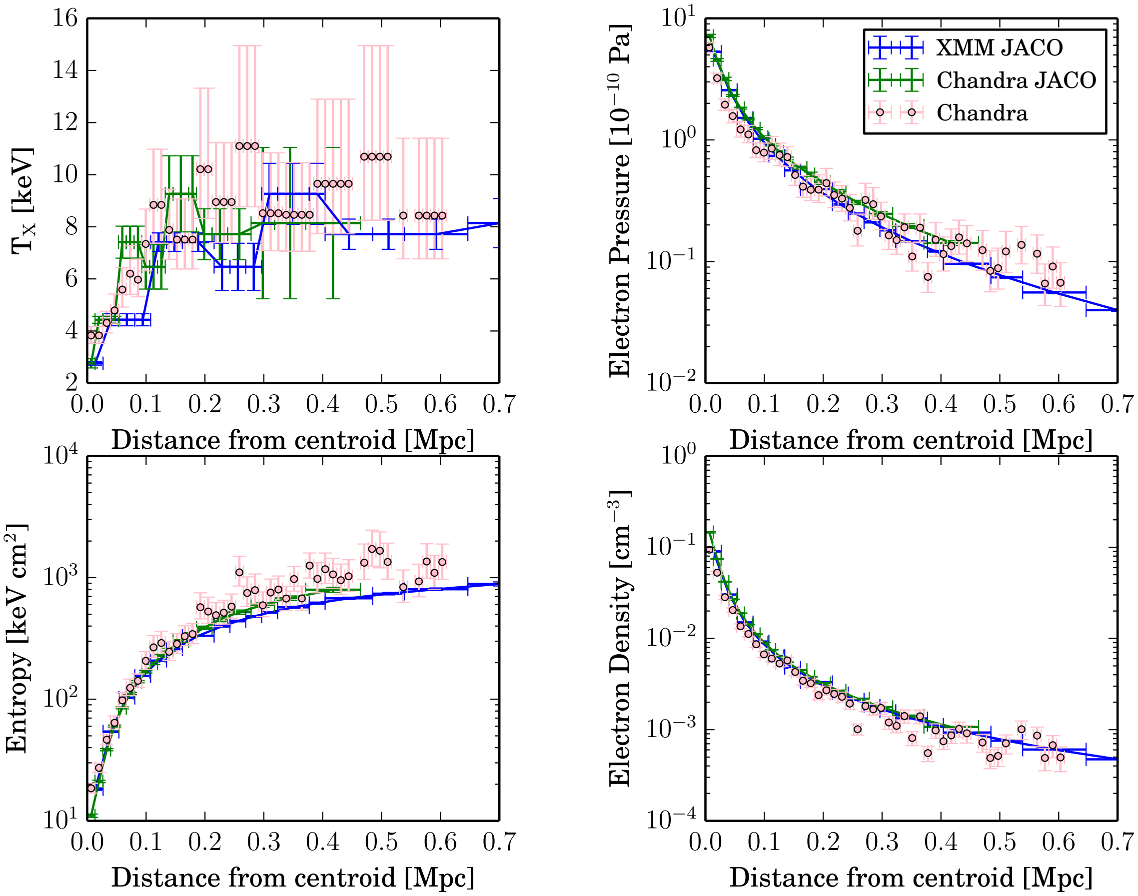

Figure 3.2 ACCEPT style profiles. We plot the temperature (projected for the non JACO analysis labeled "Chandra"), electron density, electron pressure, and entropy for the cluster as a function of physical distance from the cluster center. The horizontal error bar describes the width of the annulus where the Xspec model was fit. The error bars from JACO are 68% uncertainties assuming statistical-only errors determined with MCMC procedure while the non JACO Chandra data are 90% uncertainties.

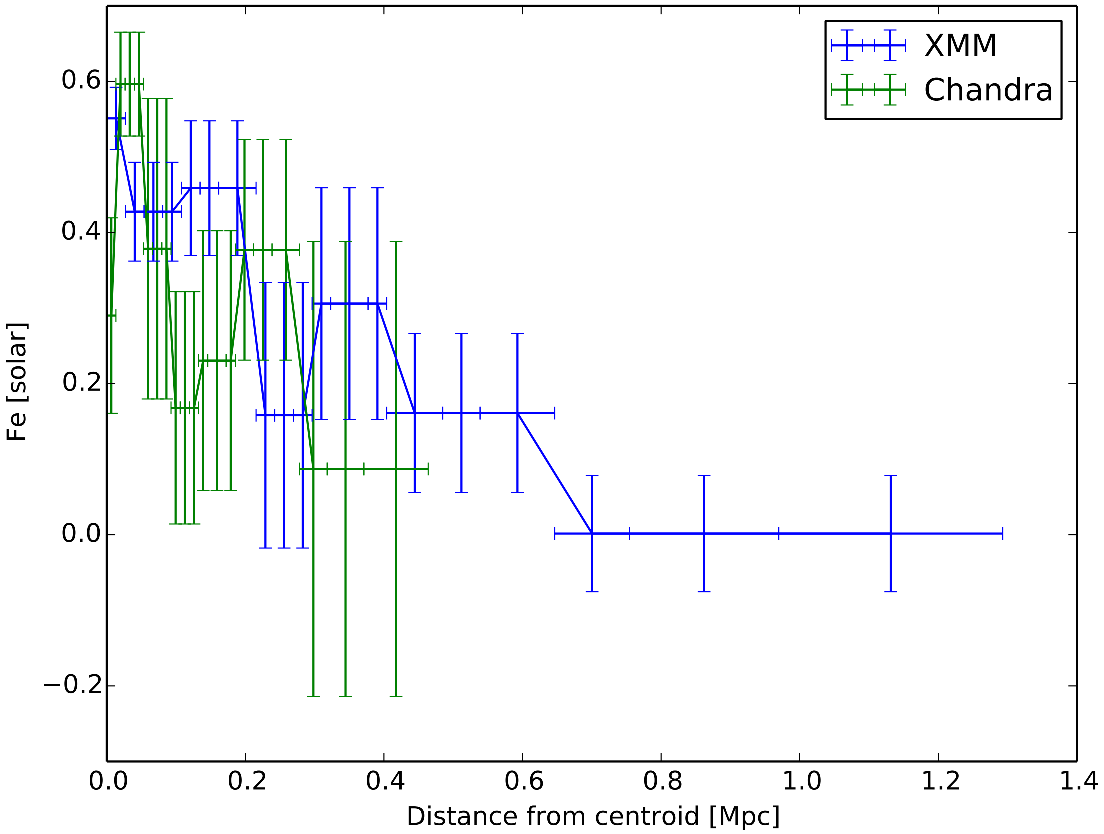

Figure 3.3 JACO Metallicity. We plot the JACO analysis for the metallicity of the cluster using both the XMM and *Chandra* data as a function of physical distance from the cluster center. The horizontal error bar describes the width of the annulus where the Xspec model was fit. The error bars from JACO are 68% uncertainties assuming statistical-only errors determined with an MCMC procedure.

calibrated the combined image with the spectrophotometric star LTT 7379 [Hamuy et al., 1994]. The images were aligned to the world coordinate system (WCS) using stars from the Two Micron All Sky Survey (2MASS). The resulting images are aligned to within $0.2''$ astrometric tolerance in right ascension and $0.3''$ tolerance in declination. To correct the image from foreground Galactic extinction we used an E(B-V) = 0.1491 and assumed A_V/E(B-V) = 3.1 [Schlegel et al., 1998]. We calculated a total Hα+[NII] luminosity of $189 \pm 6 \times 10^{40}$ erg s^{-1} for the cluster inside a circular aperture with a radius of $8''$ (21.5 kpc) and centered it on $20^h14^m51.57^s$ $-24°30'22.3''$ to avoid a poorly subtracted star near the galaxy. We took a background from an $8''$ radius circle of blank sky centered on $20^h14^m54.29^s$ $-24°30'13.8''$. The net Hα image is presented in Figure 3.4 with the *Chandra* X-ray contours overlayed.

Optical spectra of the BCG were taken with the Goodman spectrograph [Clemens et al., 2004] on July 25th, 2012. The Goodman spectra were taken with the 600 ℓ/mm grating (~2600 Å coverage) centered on 6500 Å with the $1.68''$ wide slit, which corresponds to an approximate rest wavelength range of 4510 Å−6760 Å. We observed the BCG at a position angle 110° east of north, aligned with the elongation of the central Hα region, and centered on the brightest pixel of the BCG.

We reduced the 2D spectra using the standard IRAF spectral reduction routines in the NOAO *onedspec* and *twodspec* packages. FeAr and quartz lamps were observed before and after each observation. The CCD on Goodman exhibits severe spectroscopic (multiplicative) fringing from the interference patterns of the monochromatic light. The fringing is approximately 20% peak-to-peak in wavelengths beyond 7000 Å, with spacing of ~35 Å between the peaks of the fringes. To make a fringe correction frame we normalized the overall response in the quartz flat to a third order spline. We did not detect variations in the fringe pattern between the before and after quartzes: normalized fringe frame variations were <

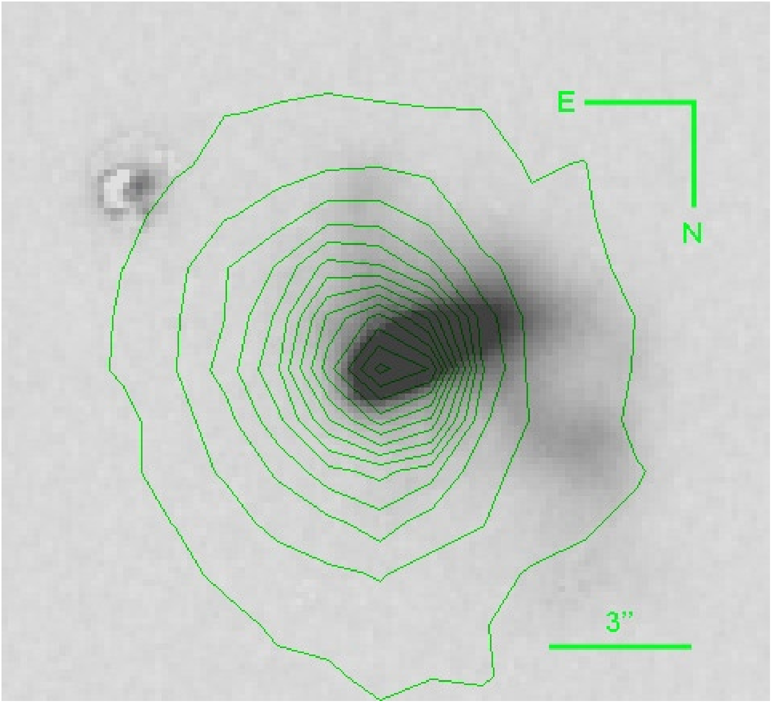

Figure 3.4 Continuum subtracted Hα image of the BCG of the cluster. The *Chandra* X-ray surface brightness contours (0.5-7.0 keV) are plotted on the SOI Hα, continuum subtracted, image. The X-ray contours are compressed perpendicular to the diffuse Hα wings of the BCG. The seeing has a FWHM $\sim 0.8''$.The scale of $3''$ is approximately 8 kpc for the cluster. The feature in the upper left hand corner is a residual from an imperfectly-subtracted star image.

0.5%. We were able to reduce 20% peak-to-peak fringing down to 2% by dividing by the normalized fringe image. For wavelength calibration we identified lines in the FeAr lamp (contaminated with Helium) spectra. We verified the centers of the night sky lines in the object frames($\lambda\lambda$5577, 5889, 6300, 6363, 6863, 6923, 7276, 7316, and 7340 Å) were within 1 Å of our wavelength solution. We flux calibrated the spectra using the *APALL* super-task with observations of the spectrophotometric standard star LTT 9491. To examine emission features in the spectra we extracted 3 pixel ($0.45''$) wide 1D spectra. The results of these spectra are in Table 3.3.

Table 3.3. Goodman Spectral Line Fits.

Spectral Line (—)	**Region Center**[a] **(Pixels)**	**Line Center** (Å)	**EQW** (Å)	**Flux** (10^{-16} erg s^{-1} cm^{-2})	**FWHM** (Å)
Hβ	800	5616.82 ± 0.3	-24.7 ± 1.7	2.367 ± 0.16	8.882 ± 0.9
OIII 5007		5786.24 ± 2.28	-7.7 ± 2.9	0.7731 ± 0.3	12.44 ± 5.89
NI 5199		6006.91 ± 1.03	-10.9 ± 2.2	0.9945 ± 0.2	9.565 ± 2.88
OI 6300		7279.13 ± 0.4	-22.2 ± 1.5	1.974 ± 0.14	9.464 ± 0.99
Hβ	803	5616.55 ± 0.38	-20.0 ± 1.6	2.381 ± 0.19	9.636 ± 0.88
OIII 5007		5784.63 ± 2.05	-8.3 ± 2.1	1.007 ± 0.26	13.68 ± 4.03
NI 5199		6006.66 ± 1.25	-9.0 ± 1.7	1.023 ± 0.19	10.61 ± 2.61
OI 6300		7279.21 ± 0.58	-15.4 ± 1.5	1.735 ± 0.17	11.22 ± 1.29
Hβ	806	5616.07 ± 0.45	-13.9 ± 1.1	2.056 ± 0.16	9.529 ± 0.62
OIII 5007		5784.11 ± 0.94	-6.8 ± 1.8	0.9873 ± 0.27	10.95 ± 3.62
NI 5199		6006.35 ± 1.92	-7.4 ± 1.5	0.9811 ± 0.19	12.14 ± 2.94
OI 6300		7278.44 ± 0.55	-14.0 ± 1.5	1.76 ± 0.18	10.98 ± 1.02
Hβ	809	5615.08 ± 0.6	-11.6 ± 0.9	1.974 ± 0.16	9.94 ± 1.08
OIII 5007		5783.43 ± 0.91	-9.3 ± 1.4	1.546 ± 0.24	13.76 ± 2.75
NI 5199		6006.43 ± 1.05	-7.2 ± 1.4	1.075 ± 0.22	11.65 ± 2.22
OI 6300		7277.94 ± 0.83	-12.8 ± 1.3	1.83 ± 0.19	12.67 ± 1.26
Hβ	812	5614.27 ± 0.52	-12.3 ± 1.1	2.264 ± 0.21	10.11 ± 0.93
OIII 5007		5782.22 ± 0.73	-11.2 ± 1.0	2.014 ± 0.19	13.27 ± 1.9
NI 5199		6005.64 ± 1.53	-5.1 ± 0.9	0.8571 ± 0.15	9.897 ± 2.94
OI 6300		7276.64 ± 0.75	-13.8 ± 1.2	2.104 ± 0.18	13.85 ± 1.35
Hβ	815	5613.0 ± 0.59	-12.8 ± 0.9	2.37 ± 0.16	10.53 ± 1.05
OIII 5007		5781.22 ± 0.49	-12.5 ± 1.2	2.228 ± 0.22	12.23 ± 1.0
NI 5199		6005.62 ± 1.08	-5.8 ± 1.7	0.9444 ± 0.27	12.98 ± 4.4
OI 6300		7276.48 ± 0.81	-11.5 ± 1.4	1.714 ± 0.2	13.53 ± 2.05
Hβ	818	5612.06 ± 0.32	-14.6 ± 1.2	2.415 ± 0.21	9.398 ± 0.93
OIII 5007		5779.17 ± 0.37	-13.2 ± 1.0	2.168 ± 0.16	8.645 ± 0.89
NI 5199		6004.6 ± 2.76	-5.0 ± 1.4	0.7397 ± 0.2	13.97 ± 5.03
OI 6300		7275.74 ± 1.63	-8.3 ± 1.7	1.148 ± 0.23	13.45 ± 2.92
Hβ	821	5611.1 ± 0.28	-13.3 ± 1.4	1.895 ± 0.21	8.033 ± 1.04

Table 3.3 (cont'd)

Spectral Line (—)	**Region Center**[a] **(Pixels)**	**Line Center (Å)**	**EQW (Å)**	**Flux** (10^{-16} **erg** s^{-1} **cm**$^{-2}$)	**FWHM (Å)**
OIII 5007		5778.52 ± 0.33	-12.3 ± 1.1	1.791 ± 0.16	6.875 ± 0.76
NI 5199		6005.0 ± 3.3	-4.6 ± 2.3	0.5812 ± 0.3	12.49 ± 9.32
OI 6300		7275.75 ± 2.5	-10.0 ± 1.8	1.056 ± 0.19	18.93 ± 5.98
Hβ	824	5611.33 ± 0.63	-10.2 ± 1.4	1.189 ± 0.17	8.039 ± 1.42
OIII 5007		5778.55 ± 0.45	-10.4 ± 1.1	1.239 ± 0.13	6.552 ± 0.95
NI 5199		6005.31 ± 3.61	-6.2 ± 2.2	0.6171 ± 0.22	15.48 ± 9.44
OI 6300		7274.81 ± 3.82	-9.7 ± 3.1	0.7907 ± 0.25	22.96 ± 13.93
Hβ	827	5612.19 ± 1.51	-8.9 ± 2.3	0.7779 ± 0.2	11.85 ± 3.72
OIII 5007		5779.16 ± 1.37	-7.2 ± 1.4	0.6745 ± 0.13	8.567 ± 1.92
NI 5199		6006.36 ± 7.97	-2.9 ± 5.5	0.2399 ± 0.46	8.206 ± 10.71
OI 6300		7272.52 ± 15.44	-3.3 ± 5.4	0.2379 ± 0.38	15.7 ± 27.14
Deblended Hα+NII					
NII 6548	778	7568.33 ± 2.01	-33.4 ± 6.7	0.6347 ± 0.13	9.687 ± 3.17
Hα		7586.6 ± 0.71	-111.0 ± 16.6	2.168 ± 0.33	13.43 ± 1.89
NII 6548	781	7568.33 ± 0.91	-27.0 ± 5.6	0.7375 ± 0.15	9.106 ± 2.52
Hα		7585.78 ± 0.39	-86.9 ± 9.0	2.414 ± 0.25	10.35 ± 0.88
NII 6548	784	7568.54 ± 0.47	-31.7 ± 5.7	1.029 ± 0.18	9.581 ± 1.94
Hα		7585.56 ± 0.29	-96.4 ± 5.0	3.102 ± 0.16	9.341 ± 0.53
NII 6548	787	7568.5 ± 1.26	-35.2 ± 5.0	1.237 ± 0.18	10.63 ± 2.66
Hα		7585.2 ± 0.21	-110.4 ± 6.5	3.983 ± 0.24	8.732 ± 0.59
NII 6548	790	7568.14 ± 0.45	-45.8 ± 3.9	1.816 ± 0.15	9.71 ± 1.12
Hα		7584.96 ± 0.13	-129.2 ± 3.0	5.236 ± 0.12	9.063 ± 0.31
NII 6548	793	7567.73 ± 0.35	-47.6 ± 3.4	2.293 ± 0.17	10.26 ± 0.75
Hα		7584.68 ± 0.14	-131.5 ± 3.5	6.353 ± 0.17	9.238 ± 0.31
NII 6548	796	7567.25 ± 0.46	-39.3 ± 3.2	2.641 ± 0.22	10.3 ± 0.86
Hα		7584.32 ± 0.09	-112.1 ± 2.9	7.643 ± 0.2	9.663 ± 0.29
NII 6548	799	7567.18 ± 0.38	-29.9 ± 2.1	2.742 ± 0.19	10.2 ± 0.63
Hα		7584.15 ± 0.11	-92.1 ± 2.2	8.255 ± 0.2	10.12 ± 0.24
NII 6548	802	7567.38 ± 0.58	-30.5 ± 2.2	3.098 ± 0.22	13.99 ± 1.43
Hα		7584.17 ± 0.17	-86.0 ± 2.4	8.539 ± 0.24	10.77 ± 0.24

Table 3.3 (cont'd)

Spectral Line **(—)**	**Region Center**[a] **(Pixels)**	**Line Center** **(Å)**	**EQW** **(Å)**	**Flux** **(10^{-16} erg s^{-1} cm^{-2})**	**FWHM** **(Å)**
NII 6548	805	7566.03 ± 0.68	-25.0 ± 3.1	3.171 ± 0.39	13.99 ± 1.37
Hα		7583.59 ± 0.19	-67.8 ± 2.1	8.501 ± 0.27	12.53 ± 0.5
NII 6548	808	7565.3 ± 1.29	-26.7 ± 4.1	3.737 ± 0.58	17.35 ± 2.15
Hα		7582.56 ± 0.28	-67.0 ± 3.8	9.128 ± 0.52	13.66 ± 0.66
NII 6548	811	7563.2 ± 1.25	-22.8 ± 2.2	3.621 ± 0.35	16.26 ± 2.14
Hα		7581.34 ± 0.35	-70.2 ± 3.2	10.83 ± 0.49	15.16 ± 0.33
NII 6548	814	7560.82 ± 0.42	-8.7 ± 2.1	1.327 ± 0.32	8.786 ± 1.3
Hα		7579.15 ± 0.23	-59.6 ± 2.0	8.754 ± 0.3	14.39 ± 0.48
NII 6548	817	7558.29 ± 0.79	-7.8 ± 2.2	1.038 ± 0.29	8.08 ± 2.12
Hα		7576.12 ± 0.1	-33.8 ± 2.1	4.387 ± 0.27	6.527 ± 0.3
NII 6548	820	7558.12 ± 0.59	-9.6 ± 2.5	1.12 ± 0.29	8.056 ± 1.92
Hα		7575.67 ± 0.08	-38.2 ± 2.3	4.319 ± 0.26	5.815 ± 0.28
NII 6548	823	7558.58 ± 1.02	-13.4 ± 4.9	1.167 ± 0.43	11.34 ± 2.98
Hα		7575.63 ± 0.19	-34.5 ± 4.9	2.957 ± 0.42	6.483 ± 0.67
NII 6548	826	7557.72 ± 2.0	-5.6 ± 1.9	0.4371 ± 0.15	8.918 ± 3.99
Hα		7575.72 ± 0.5	-11.6 ± 3.9	0.8754 ± 0.29	5.318 ± 1.46

---

[a] The table is organized by $0''.45$ region starting with the easternmost region.

All fluxes and equivalent widths, computed using *splot*, are calculated in the observer's frame such that we can also estimate redshifts in each of the lines to track variation of the velocities of different elements in the cluster. We use a Gaussian profile to fit each of the lines and the *splot* bootstrap resampling (100 realizations) method to compute errors on the Gaussian profile fits. We estimated our background and continuum subtraction from a linear fit of two continuum points $\approx$ 20Å from the outer edges of each measured emission line. The error on the continuum was from the root mean square from an emission-free region. We fix this at $\sigma_0 = 4.196\times10^{-18}$ erg cm^{-2} s^{-1} Å^{-1} over the range 5600-7600Å.

We estimated the redshift of the stellar emission by Fourier cross-correlating the continuum emission in RXJ 2014.8-2430 to the spectrum of an elliptical galaxy SDSS J120028.87-000724.8 (z = 0.0813±0.0002). Using the *fxcor* task in IRAF, we shifted the SDSS spectrum to the baseline estimated redshift (0.1555) of RXJ 2014.8-2430. We binned the SDSS spectrum to match the lower spectral resolution SOAR spectrum. We extracted a 40 pixel wide spectrum for RXJ 2014.8-2430 centered on our nominal center. The correlation result was based on an emission-line-free range between 6100-7100 Å from stellar absorption lines and the error is based on results from 1000 randomly selected re-sampled sections 200 Å wide. We find a velocity shift to the baseline estimate of, -10.57 km s^{-1} ± 29.10 km s^{-1}, which is statistically consistent with zero shift from the nominal emission line redshift.

3.2.3 X-ray AGN Limits

We place an upper limit on the X-ray flux of an AGN point source using the CIAO tool *celldetect*. The events were restricted to the $0.5 - 7.0$ keV energy range and the search was limited to fixed cell sizes of 1 pixel and 3 pixels near the cluster center. The local cluster background was estimated (13.67±4.54 counts pixels^{-2}) from a $5''$ circle near the center of the cluster. We did not find any $< 3\sigma$ detections of compact sources within $10''$ of the cluster center. Using the CIAO *aprates* task we calculated a 3σ upper limit on the counts expected on an AGN point source. The algorithm[1] determines confidence intervals based on a Bayesian background-marginalized posterior probability distribution function of possible source counts. We assume the possible point source will nearly have all of its flux in a single cell and the background is the mean value computed within $5''$ of the center. Our 3σ upper limit of 17 counts for a point source above the local background of extended cluster emission in the core of the cluster, corresponding to a limit of $< 1.55\times10^{-14}$ erg cm^{-2}s^{-1} (at $\bar{E}$=2 keV), corresponding to an 0.5-7.0 keV X-ray luminosity of $< 5.39\times10^{42}$ erg s^{-1} for a power-law (α=1) point source at the cluster redshift.

3.3 Discussion

3.3.1 Radio Bubble Limits

Given the central entropy of the cluster and the existence of a strong central radio source, the apparent lack of a bubble may be surprising. The additional lack of radio lobes would suggest that any potential cavities may be small and new or along the line of sight. In order to estimate the size of a bubble expected in such a source, we used the relation in Rafferty et al. [2006]. As in Rafferty et al. [2006], we define the X-ray cooling radius to be that within which the gas has a cooling time less than 7.7×10^9 years, which is the cosmic time elapsed since $z = 1$ to the present epoch for the cosmology adopted in this paper. Rafferty et al. [2006] consider this cooling time representative of the time it has taken the cluster to relax

---

[1] The details are found in `http://cxc.harvard.edu/csc/memos/files/Kashyap_xraysrc.pdf`.

and establish a cooling flow. We use the same Xspec model fits in Section 2 and include a fit with the MKCFLOW model added and fix the low temperature to 0.1 keV. Similar to the modeling for the MEKAL model fits, the metallicity is tied across pairs of annuli, outside of the central region. The high temperature, metallicity, and temperature for the MKCFLOW model are tied to the simultaneously fit MEKAL model. However, outside of the cooling radius the MKCFLOW normalization is set to zero. We calculate the luminosity of each annulus after fitting using *lumin* in Xspec in the extrapolated range of 0.1 to 100 keV to estimate the bolometric luminosity. We estimate the bolometric luminosity $L_{bol} = 19.7 \times 10^{44}$ erg s^{-1} in the range 0.11555 - 100.0 keV rest frame over the total MEKAL model inside all annuli (675 kpc). This luminosity is reasonably consistent with the bolometric luminosity calculated from XMM ($L_X = 21.06 \pm 0.07 \times 10^{44}$ ergs^{-1} within $R_{500} = 1155.3 \pm 4$ kpc) which was over a slightly larger area. Using the technique from Bîrzan et al. [2004] we define the cooling time for each of the annuli using $t_{cool} = 3nkT_X/2n_e n_H \Lambda(T,Z)$, where $\Lambda(T,Z)$ is the X-ray emissivity as a function of temperature and metallicity. We solve for $\Lambda(T,Z)$ assumed by the MEKAL model using the normalization from the MEKAL model and the bolometric luminosity. We assume a fully ionized plasma such that the total number density $n = 2.3 n_H$. We compute the cooling radius at a distance from the cluster centroid such that the cooling time is less than 7.7×10^9 years. For this cluster the cooling radius is 105 kpc ($39''$). Inside this aperture we have a luminosity $L_X(< r_{cool}) = 4.71 \times 10^{44}$ erg s^{-1}.

We use the relation in Figure 6 of Rafferty et al. [2006] to estimate the $P_{cav} \sim 5 \times 10^{44}$ erg s^{-1} (assuming a γ=4/3 for relativistic particles which gives a 4pV enthalpy) for a possible AGN source given our X-ray luminosity inside the cooling radius. With the bubble in pressure equilibrium with the X-ray gas ($\sim 5 \times 10^{-10}$ erg cm^{-3} near the core) and a bubble age of 10^7 years (Bîrzan et al. [2004] estimate ages for bubbles seen ranging from 0.5-15 $\times 10^7$ years) we would expect a pair of spherical bubbles to each have a radius of $(3\mathrm{P}_{cav}t_{cav}4\pi P_X)^{1/3}$ $\sim 5''$, where P_X is the X-ray pressure and t_{cav} is the time the cavity has been expanding. Assuming the typical range of enthalpies from 1pV to 16 pV gives a factor of 5 in bubble power in either direction. A lower power assuming a lower enthalpy of 1pV would give a bubble pair with radii $\sim 3''$. The largest bubbles expected would have radii $\sim 9''$ in size. Bîrzan et al. [2004] indicate that this relation between radio power and X-ray luminosity is a limit on how much work the radio source could contribute to the system to compensate for the cooling, it is not necessarily required. Their figure plots assumed total enthalpy levels of the cluster from 1pV to 16pV which is the range observed clusters fall in if heating and cooling are balanced.

3.3.2 X-ray Cavity Toy Model

It is possible that bubbles have formed aligned with the center of the cluster, along our line of sight. Such bubbles might be difficult to detect in projection. We create a toy model to help determine potential sizes ($3'' - 9''$) of cavities which could not have been missed along our line of sight in *Chandra* data. We use a β model with the gas density, $\rho(r)$, from Sarazin [1988] in the form $\rho(r) \propto (1 + (r/r_0)^2)^{-3\beta/2}$ and use the fit parameters from the Sherpa fit to the 2×2 binned data. We create a 3D grid with 512 pixels ($1''$/pixel) per side and apply the β model from the center of the grid with added Poisson noise. We compute the emission measure (EM$\equiv \int n_e n_p \, dl$) from the 3D model by taking the square of each element and summing along an axis. We expect the projected form $f(b) \propto (1 + (b/r_0)^2)^{-3\beta+1/2}$ from the projected model [Sarazin, 1988]. We scale the amplitude of the projected image such that the projected image has the same amplitude as the fit from the 2D β model. Before projecting the images, a pair of simulated bubbles can be added along the line of sight by

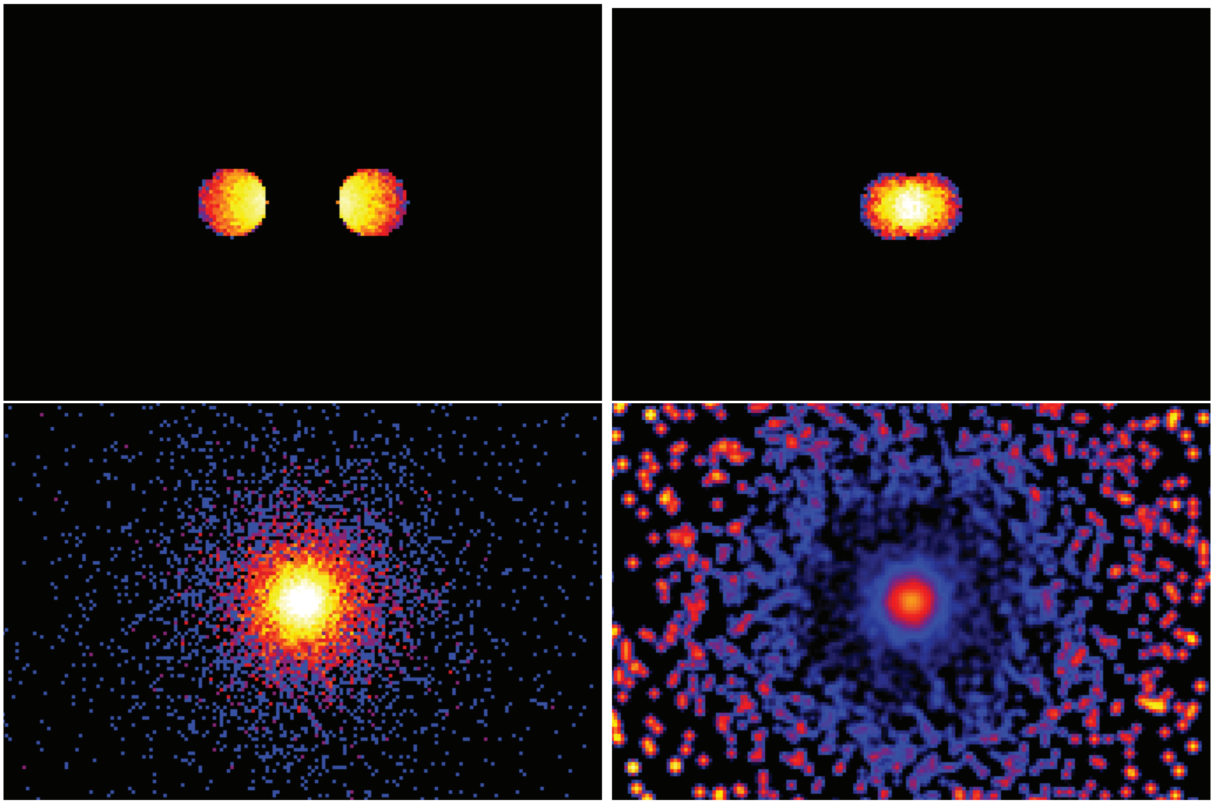

Figure 3.5 X-ray Cavity Toy Model. The top two panels are a pair of 10″ cavities with the left image presented in the plane of the sky and the right image presenting the cavities nearly along our line of sight. The color scales for the cavity images indicate the relative amount of counts removed from the β model by introducing these cavities. The lower left image applies the cavities of the second image to the simulated cluster. The lower right image is an unsharp masked of the lower left image.

introducing empty spheres of different radii and distances from the cluster center.

In Figure 3.5 we show an example of a pair of cavities 10″ (on the larger side of what we would have estimated for an X-ray cavity from the radio power), equivalently 26.94 kpc, in radius on the plane of the sky with their inner edges 10″ from the cluster center. The second image is the same bubble pair but it is rotated such that the pair is now along our line of sight but the center of each bubble is offset, in the plane of the sky, by 5″ from the cluster center. The third image is the β model with the pair of 10″ cavities nearly along the line of sight. The fourth image is the unsharp masked image of the cluster in the third image.

To determine if a cavity created along the line of sight is significant, we compare the total counts in the flattened cluster image with a pair of cavities to the flattened image of the same cluster without cavities. The region of comparison is restricted to a circular aperture equal to the cavity size. In Figure 3.6 we show the significance of detection between the two given a Poisson count error. For a pair of cavities to be at a detection threshold of 5σ or better, the cavities would have to be no more than 20 kpc from the cluster core. The lack of such detections in our data mean we can rule out the existence of cavities larger than about 8 kpc within 20 kpc of the core. Using the cluster sound speed in the cluster core, $v_{cs} = \sqrt{\gamma k T_X / \mu m_H}$, with $\gamma = 5/3$ and $\mu = 0.62$, it would take a cavity ≈45 million years to reach 20 kpc. With an expected cavity lifetime of less than 100 million years, it is possible for cavities on the small end ($\sim 3''$) of the expected size to exist in this cluster along our line of sight without being detected in the X-ray image. Cavities of this size would only be detected if they existed within 22 kpc of the core. Detecting smaller cavities is limited by the effective resolution and also by the knowledge of the inner gas profile. A bubble squarely along the line of sight would flatten the surface brightness distribution, making it hard to tell the difference between that and a surface brightness distribution lacking a bubble but having a small core. So a single small (<8 kpc) bubble would be harder to see even if it were near the cluster core where the contrast would be high.

It may be possible that a sloshing motion, which is over a region similar in size to the predicted bubble, in addition to creating the edge seen in the image, could also be washing out the decrement from the cavities. In this case, we might miss a cavity which would otherwise be more obvious.

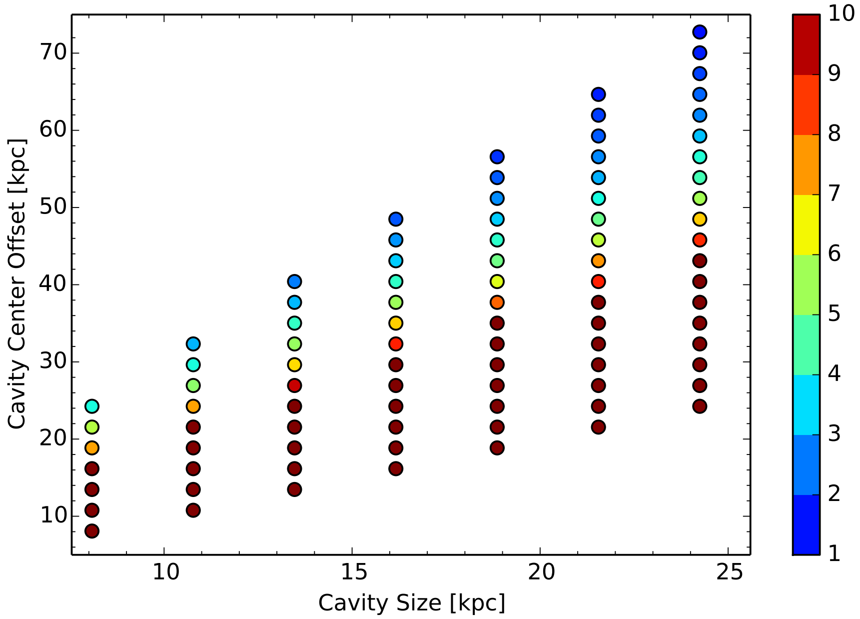

Figure 3.6 Toy Model Fits. We plot an array of simulated cavity model configurations. The predicted detection significance of each cavity configuration is indicated by the color scale. The cavity center offset is the distance of the inner edge of the cavity from the center of the cluster, while the cavity size is the diameter of the cavity. For the smallest cavities (8 kpc $\sim 3''$) we can place a 5σ upper limit on a cavity within a distance of 20 kpc ($\sim 8''$). More distant cavities of this size would be difficult to detect in our data.

3.3.3 Sloshing in the Cluster Core

Walker et al. [2014] showed that both the XMM and *Chandra* data demonstrate structure in the surface brightness as well as cold fronts which are qualitatively similar to simulations of sloshing in cluster cores due to minor mergers. From the *Chandra* data, they identified the same east-west pair of cold fronts we identify here. However, it is clear in our *Chandra* unsharp masked image in Figure 3.1 that the inner cold front (CF1 in Walker et al. [2014]) wraps clockwise up to the north and back down to the west of the core. Additionally, from the XMM data, they find an excess “swirl” pattern reaching out to 800 kpc from the center of the cluster. In comparison to sloshing observed in other clusters, sloshing at this distance (approximately half the virial radius) hasn’t been seen before. At this point in the cluster, they also found a surface brightness discontinuity where they measure cold, low entropy gas. Give the widely different scales of sloshing and the fact that the cool core is not disturbed, they conclude that these must be two independent sloshing events.

While there are indications of sloshing in the cluster core, there are a few inconsistencies seen between this cluster and other clusters which have core sloshing. As mentioned in the introduction, sloshing cores have been shown in observations to distribute metals from the cluster center and flatten the metallicity profile [Simionescu et al., 2010, de Plaa et al., 2010]. Additionally, the position of the X-ray peak is likely to be offset from the location of the BCG as the X-ray gas sloshes around the cluster core. RXJ 2014.8-2430 has a peaked metallicity (Figure 3.3) as well as alignment of the X-ray centroid (from §3.2.1) with the Hα and stellar emission. We compare the morphology of RXJ 2014.8-2430 to the various simulated clusters in ZuHone et al. [2010]. They find that as the subclusters fall into the cluster core there is a brief period where the X-ray emission is compressed and the luminosity increases, as seen in their Figure 17. From their Figure 10, the gas peak is within 10 kpc of the galaxy cluster potential minimum for the first 1 Gyr. After the gas peak shifts away due to sloshing, the peak returns to within $>$ 10 kpc from the galaxy cluster potential minimum approximately every 500 Myrs. Also, they find that in the presence of viscosity as well as the addition of a large BCG potential (their Figure 26) in the cluster core will decrease the core heating expected from sloshing. Based on the suggestions of these simulations, we may be observing RXJ 2014.8-2430 during a special, but not necessarily early, period of a minor subcluster merger. Alternatively, a recent sloshing event in the cluster core could give the structure seen in the core, but the sloshing was too gentle to disperse the metals in the core.

3.3.4 Velocity structure in the BCG Optical Emission Lines

The Hα + [NII] is brighter over a larger area so we were able to extract 17 regions of 3 pixels each from the 2D calibrated spectral image discussed earlier. For the Hα + [NII] complex, we deblend the features by simultaneously fitting the Hα line with the two [NII] lines using *deblend* in splot. However the [NII] λ 6584 is contaminated by a bright sky line and, similar to Donahue et al. [2010] we use the line measurements for the [NII] λ 6548 line and multiply by a factor of three (the constant [NII] line ratio fixed by atomic physics) to determine the [NII] λ 6584 value for computing abundance ratios. Using these values, the ratios, like ratios of similar regions in nearby clusters of galaxies (e.g. Heckman et al. [1989]), fall into the lower right side of the BPT diagram [Baldwin et al., 1981] which is used to diagnose the difference between ionization by hot stars and a Low Ionization Nuclear Emission Region (LINER). We note, however, that unlike a LINER, which is unresolved point-like, this emission line region is extended and unlikely to be heated by the radiation coming from an AGN, based on arguments similar to those presented in Heckman et al.

[1989]: a lack of ionization gradient that would indicate a central ionization source, presence of extended emission with nearly constant line ratios, relatively constant velocity widths of fairly modest width. From a sample of brightest cluster and brightest group galaxies in the Sloan Digital Sky Survey, von der Linden et al. [2007] found that most have emission line ratios which place the galaxies onto the LINER region of the BPT diagram. The [OIII]/Hβ ratio is flat across the cluster, but the [NII]/Hα ratio, in Figure 3.7, dips down by a factor of two at the center of the BCG. This increase in the Hα to [NII] ratio could indicate a weak radio source in the core, in line with the idea that the "young" radio source in the cluster is at an early time in its kinetic energy output.

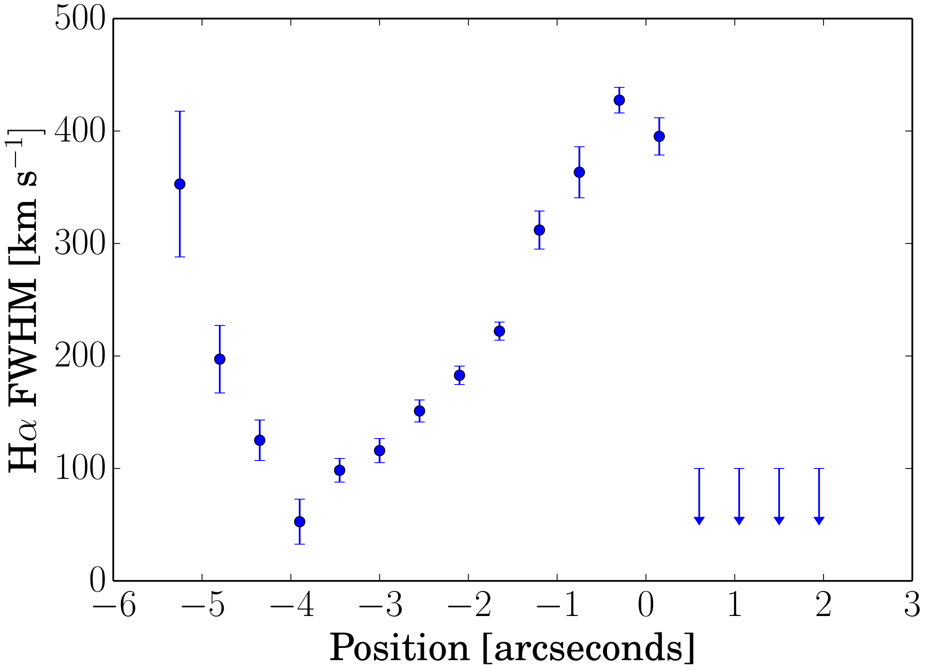

Figure 3.7 Goodman Spectra Velocities. We plot the velocity widths of the Hα, which have the component of instrumental velocity removed in quadrature. To the right of center, the velocity widths are unresolved upper limits with widths less than the instrumental velocity.

For the extracted X-ray spectra in the regions on and off Hα, presented in Table 3.2 the regions with the Hα emission are surrounded by X-ray emitting gas that is slightly cooler and that hot gas has a higher metallicity than those regions that are not coincident with the Hα wings. In general, we see in Figure 3.3 that the cluster has a strong metallicity gradient and a metal rich core in the X-ray gas. Unlike what has been seen in some other clusters (e.g. Sparks et al. [2004]), the structure in the soft (< 1 keV) X-ray, which has a mostly symmetric core to the broadband X-ray image, does not align with the Hα structure of an elongated core with perpendicular wings.

We calculated an instrumental velocity width of 294 km s^{-1} based on the width of unsaturated FeAr lines in the calibration spectra. The instrumental velocity we find is similar to the expected spectral resolution for our instrument setup[2]. To estimate the true velocity width, we subtracted the instrumental velocity from the observed velocity width in quadrature. We compared the spatial position of the continuum emission to the spatial position of the Hα by extracting 25 Å regions around the center of the Hα as well as an equivalent width area of emission blueward of the Hα + [NII] complex. The continuum and Hα have a similar peak, within $0''.3$ of 812 pixels which was the nominal center pointing. While the emission in the Hα is not as spatially symmetric as the continuum light, we do see that the peak of the Hα emission and the continuum emission are co-located with the X-ray peak to within $1''$.

In Figure 3.8 we compare the redshifts of different emission and absorption lines. Relative to the center, there is a velocity gradient along the central Hα. We compare that to the 90% confidence interval (0.1531 ± 0.0017) on a fit for the redshift from the *Chandra* spectra using the same Xspec models but freeing the redshift parameter while requiring it to be the same for all cluster spectra. Given the patterns in the velocity structure, the gas is likely infalling or outflowing. The optical velocity structure doesn't look like a rotating disk since

---

[2] `http://www.goodman-spectrograph.org/observers.html`

it is one-sided and the disk would have to be off-center from the peak of the emission, even though the emission peaks are aligned. However, we can't tell whether the velocity gradient is indicative of gas infall or outflow.

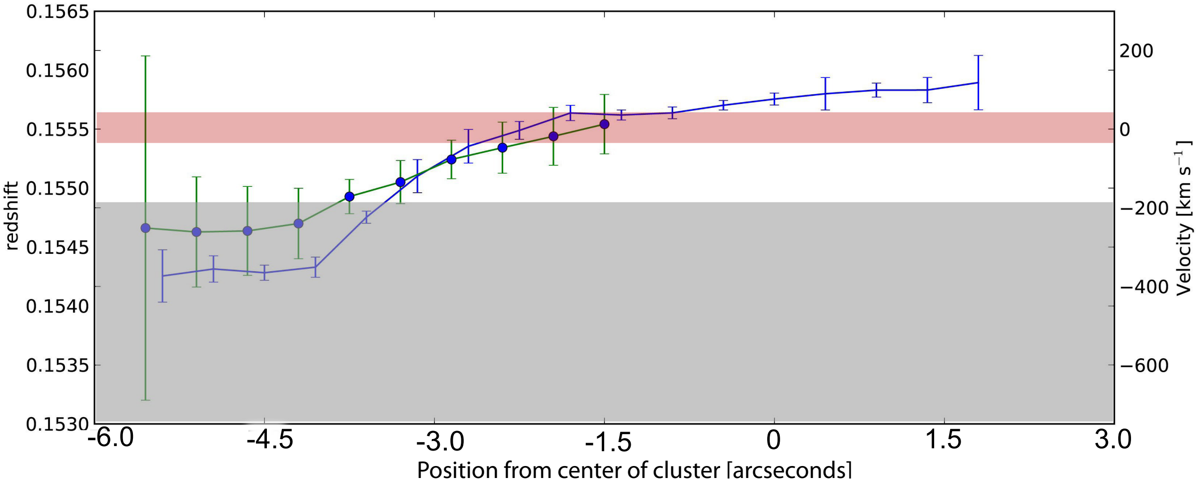

Figure 3.8 Goodman Spectra Velocities. Redshifts and equivalent line of sight velocities with respect to the redshift 0.1555. The green data points with circles in the points are averages from Hβ, [OIII] 5007, [NI] 5199, [OI] 6300. The blue line is the average from Hα and [NII] 6548. The gray band marks the 90% confidence range for the Chandra redshift fit from using the same Xspec models but freeing the redshift parameter while requiring it to be the same for all cluster spectra. The narrow red band marks the cross correlation center for the stellar absorption spectra.

Voit and Donahue [2011] estimate that the stellar mass loss of stars in BCGs may be as high as 8 $M_{\odot}$ per year, which is at least as large as star formation rates in most BCGs. This gas from stellar mass loss is also predicted to remain cool and may be a source of emission line gas, such that some of the emission line gas seen in the BCG of RXJ 2014.8-2430 could originate from stellar mass loss. While this theory predicts the emission line gas would have a similar velocity to the stars in the BCG, sloshing in the cluster core could affect the relative motions of the gas and stars in the BCG. In the presence of sloshing caused by a minor merger through the center of the cluster, the ISM of the BCG would be affected by the interactions in the ICM more than the stars. Therefore, the emission line gas from stellar mass loss may achieve a different velocity distribution than the stellar velocity distribution. With a velocity gradient that spans almost ±200 km s^{-1} and spans the range of the best-fit mean velocities of both the ICM and the BCG stars, the true sloshing speed is likely high. We are only measuring radial velocities while the sloshing signatures we observe are in the plane of the sky, therefore the true, three dimensional sloshing speed is likely much higher than the radial velocity.

3.4 Summary

We conduct a multi-band analysis of the cool core cluster RXJ 2014.8-2430. Prior observations show this cluster is a strong cool core and also demonstrates strong emission in other wavelength regimes. The decrements we see in the β model fits as well as the unsharp mask image are indicative of a possible pair of cavities just offset from our line of sight as well as sloshing in the core. In models presented by ZuHone et al. [2010] it is likely that the sloshing in the cluster has only begun recently. On the other hand, we see a very strong metallicity peak in the core of the cluster such that the metallicity in the central tied bin is supersolar which is inconsistent with the suggestion that sloshing will transport metals from the center of the cluster to the outskirts, effectively flattening the profile of the metallicity profile [Simionescu et al., 2010, de Plaa et al., 2010]. However, it is possible to decrease the effects of sloshing with additional viscosity in the core as well as larger potential from the inclusion of a massive BCG. If the sloshing distance at this point is not much larger than the first couple bins any of these possible effects would be contained.

We see evidence for sloshing in the cluster core which, given its low central entropy, may be obscuring bubbles. The east-west sloshing compression is in the same orientation as the elongation of the central Hα and the fact that the north and south wings of the Hα are both behind the brightest knot in the center of the Hα, near the centroid of the X-rays but ahead of the X-ray peak, suggests that the X-ray gas is moving past the galaxy or the galaxy is moving through the X-ray gas. There is a significant velocity gradient along the elongated central Hα region and this emission line gas is either falling into or getting pulled through the galaxy.

We do not find evidence for an X-ray AGN, based on the lack of a point source in the X-ray images consistent with what was found by Donahue et al. [2010] in the UV. Our analysis of the optical line-emission results, and the bright central source in the radio suggest a weak AGN.

From the expectation of our X-ray cooling flux, we would expect a significant pair of bubbles which could be washed out by the sloshing in the core but we may also be in a unique position in this cluster's evolution where the radio source might just be turning on and only starting to create X-ray cavities.

Looking at the optical emission, we see that the Hα is elongated in the same direction the cluster is thought to be sloshing. From the optical spectra we see a gradient of ~ 400 km s^{-1} across the central ellipsoidal Hα region. There is a velocity gradient that indicates a likelihood the emission line gas is either infalling or getting pulled out of the BCG, depending on which side of the galaxy we are looking from. There are also Hα "wings" which are north and south of the central Hα gas, pointing away from the center of the emission.

We would also like to thank the CIAO/Sherpa X-ray school and techs for their assistance during the *Chandra* Summer School as well as through the CXO helpdesk. We also acknowledge the SOAR operators Daniel Maturana, Patricio Ugarte, Sergio Pizarro, and Alberto Pasten who helped us during our nights. Support for this work was provided by the National Aeronautics and Space Administration through Chandra Award Number GO0-11018X (MSU RC065171) issued by the Chandra X-ray Observatory Center, which is operated by the Smithsonian Astrophysical Observatory for and on behalf of the National Aeronautics Space Administration under contract NAS8-03060.

Chapter 4

Polarization Pilot Project for the SOAR Telescope

4.1 Introduction

Electromagnetic radiation consists of electric and magnetic field components perpendicular to the direction of motion. In the plane perpendicular to the direction of motion, the electric field vector is typically oriented at arbitrary angles, however, it is possible for the electric field vector to have a preferred orientation. The situation where we observe light with an electric field vector with a preferred orientation is known as polarization.

While there are many types of astrophysical sources which may be polarized, their sources of polarization fall into two categories: intrinsic polarization of light and polarization of light induced by external media. A light source is intrinsically polarized if the light is being generated by a process which creates an electric field with a preferred orientation. On the other hand, a light source, which produces random electric field angles can appear to the observer as polarized if the light is scattered or passes through certain materials.

4.1.1 Sources of Astrophysical Polarization

Many polarization studies are conducted in the near- to far-infrared because light at these wavelengths are not as attenuated by dust, which preferentially absorbs and scatters higher energy photons such as starlight. Infrared light can get through, but carry with it the polarization signature of having been scattered by aligned dust grains. Young stellar sources, which are enshrouded by gas and dust rich nebula, such as T Tauri and Wolf Rayet stars, can show significant amounts of polarization ($> 20\%$) [Bastien, 1982]. Even weakly magnetized regions with charged particles and charged dust grains may exhibit strong polarization if random thermal motions are insufficient to scramble the alignment of the grains [Davis and Greenstein, 1951]. At longer wavelengths (sub-millimeter to radio) polarization of the light from colder molecular gas as well as polarization of the light from active galactic nuclei (AGN) can be observed [Angel and Stockman, 1980]. In radio observations of AGN, the power-law spectrum characteristics of synchrotron radiation is observed from high energy particles spiralling along the magnetic field lines of the AGN jet. These jets of intrinsically polarized radio emission can extend several kiloparsecs in length.

Many processes also produce polarized light in optical ($\sim 4000 - 8000$Å) wavelengths. The polarization of emission of dust obscuring and scattering light around young stars can easily be measured in the optical as well. The optical synchrotron from AGN jets as well as supernova remnants are also observed optically and show a similarly strong polarization signal (albeit, the orientation of the optical and radio synchrotron may be different) [e.g. Perlman et al., 1999]. Saturated thermal conduction [Cowie and McKee, 1977] in an ionized plasma, which is seen in solar flares [Henoux et al., 1983a] has intrinsically polarized emission. The process of saturated thermal conduction, which we will discuss in Section 4.5.1, has been suggested as a source of optical emission line filaments of brightest cluster galaxies. Therefore, if saturated conduction is present in the emission line filaments of BCGs we can expect the emission to be polarized.

4.1.2 Observing Astrophysical Polarization

There are three common types of setups for determining optical polarization. One type of polarizer, shown in the upper panel of Figure 4.1, is a rotating waveplate polarimeter which has a rotating retarder with a fixed linear polarizer. The intensity is measured as a function of the position angle and the position of the retarder. Since there is a small number of components, calibration is easy and it is possible to determine the angle of maximal polarization to high precision. However, to maximize the polarization signal through rotation, these setups must focus on single objects in small fields. The second type, shown in the lower panel in Figure 4.1 uses polarizers and beam splitters to simultaneously measure separate Stokes parameters. The ability to measure Stokes parameters simultaneously significantly reduces the polarization variation caused by variability in the sky and weather across observations; however it is a more involved setup, requires observation of brigher object, and additional calibration is needed between separate detectors.

The third method, employed by telescopes such as the Hubble Space Telescope (HST) and now the SOAR Telescope, is the use of a set of polarizing filters. The HST has a set of three filters constructed from polarized film at angles of 0°, 60°, and 120°. A system with polarization filters is much cheaper and much more portable than systems which requires rotating retarders or beam splitters. However, while the filter system works well in space, there are added complications for ground based observations. Due to variations in the sky, taking observations that are more spread out in time can lead to less consistent results. Variations in the sky can be mitigated by using a set of four filters at 45° increments because the Stokes parameters (Q,U, and I) can be determined from two separate pairs of observations, unlike a three filter system, which requires all three filters to measure each Stokes parameters. We present our setup for SOI in Figure 4.2.

4.1.3 Cool Core Clusters and Polarization

Some brightest cluster galaxies (BCGs) in cool core clusters have shown significant emission of cool ($< 10^4$ K) gas filaments, but the sources of such emission are still under debate. Additionally, deep observations by the Chandra X-ray telescope have shown that some of the soft X-ray (< 1 keV) emission in the intracluster medium (ICM) correlates with the optical Hα filaments in these clusters further supporting the idea that the Hα filament emission is powered, in part, by the X-ray gas. One large source of Hα emission is photoionization of hydrogen by recently-formed massive stars. Hα is correlated with other signatures of star formation, such as excess UV light and excess far infrared light from dust heated by hot stars. In recent years, there is a consensus that some amount of thermal conduction can reproduce the observations seen in BCGs in some cool core clusters. Thermal conduction is the process by which heat is transferred through particle collisions due to a temperature gradient. The interface between the ICM (10^7 K) and the intragalactic medium Hα filaments ($< 10^4$ K) is a strong temperature gradient which would be an obvious candidate for this type of interaction [Sparks et al., 1989a, Ferland et al., 2009].

There have been previous studies in solar physics which observe polarized emission in regions with strong temperature gradients where the process of thermal conduction is most efficient. Polarization levels for solar are emission, a hot X-ray gas similar in temperature to

---

[1] `http://www.ctio.noao.edu/soar/`

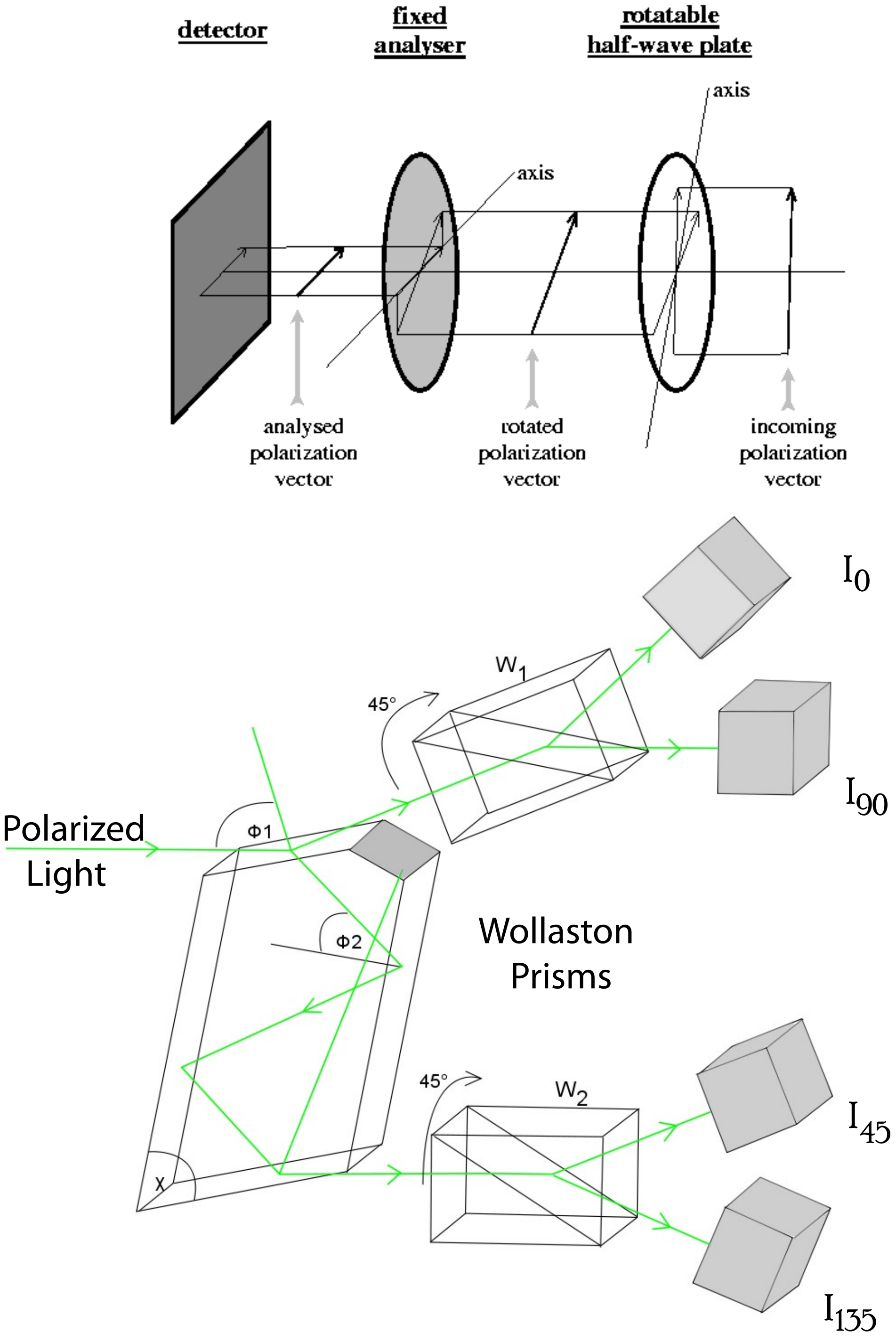

Figure 4.1 Polarimeter Designs. The upper figure is a standard single beam rotating retarder (typically a halfwaveplate) with fixed linear polarizer. The lower figure is a beam splitter design which has four detectors to measure full Stokes parameters simultaneously [Sheehan et al., 2010].

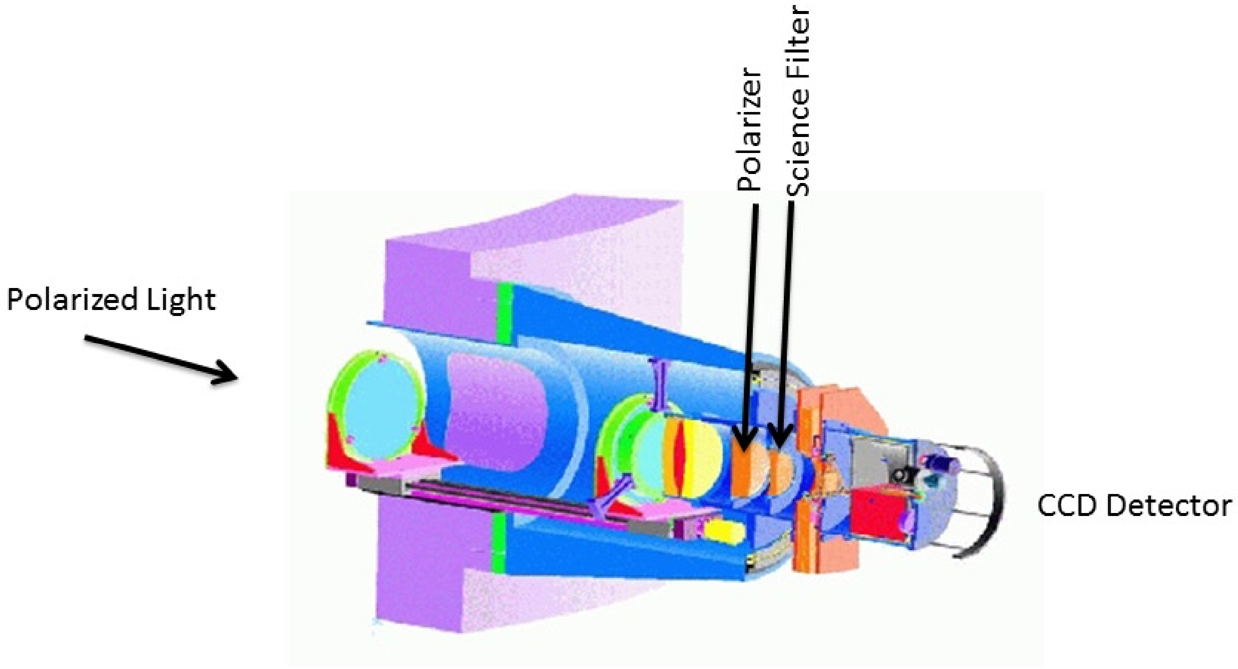

Figure 4.2 SOI Polarimetry Setup. The set up of the SOI instrument. The polarizers are placed in the filter wheel closest to the sky. The telescope feeds SOI sitting at Nasmyth focus. Variations in the sky can be mitigated by using a set of four filters at 45° increments because the Stokes parameters (Q,U,and I) can be determined as two separate pairs, unlike a three filter system which requires all three filters to measure each Stokes parameters. Image provided by the SOAR Telescope[1].

the ICM, indicate levels up to 20-30% [Henoux et al., 1983a]. In particular, polarization of Hα emission lines, give easily detectable polarization fractions of >5% in the regime where conduction is saturated [Henoux et al., 1983b].

Nearby BCGs like M87 (in the Virgo Cluster) have bright Hα filaments which can be easily observed with the SOAR Telescope and are excellent candidates for measuring possible polarization in galaxy cluster environments. Polarization measurements, or limits on polarization flux, on these nearby BCGs will help better constrain the physical processes which are relevant in the cores of galaxy clusters.

In Section 2, we discuss the observations as well as introduce the hardware used in the new polarimetry mode. In Section 3 we present the calibration and data analysis. We take both standard internal CCD calibrations (bias frames and dome flats) as well as on sky calibrations of polarized and unpolarized sources. The unpolarized sources are used to characterize the zero level polarization correction between the filters while the polarized sources are used to measure the precision of the polarization fraction and angle. Here we also discuss the variability we saw between nights and explain how we can obtain reliable polarimetry over multiple nights and the method we used to flag observations which likely had unreliable photometry. In Section 4 we present our science targets, brightest cluster galaxies (BCGs) with Hα filaments, and set upper limits on the amount of polarization in these filaments. In Section 5 we discuss the implications for the low levels of polarization in the Hα filaments in BCGs, which can help place limits on the conduction seen in the BCGs as well as what we may be able to expect from magnetic fields in BCG filaments. We conclude the paper in Section 6.

4.2 Observations

The Southern Astrophysical Research Telescope (SOAR) is a 4.1 m aperture telescope located on Cerro Pachón at an altitude of 2,700 meters (8,775 feet) above sea level, at the western edge of the peaks of the Chilean Andes. The SOAR Optical Imager (SOI) is composed of two 2048 pixel × 4096 pixel detectors. The field of view is $5' \times 5'$ (which corresponds to a physical size of 10.16cm × 10.16cm) with a physical chip gap $7.8''$ wide between the two detectors. Targets were offset, in all exposures, from the chip gap. We dithered the target to sit on at least three locations in a given observing sequence. We did not offset from the center of the field of view for our observations of globular clusters because the globular clusters covered the whole field of view. However, even for these observations, we made small (5-$10''$) dithers between each of three observations to minimize small-scale at fielding errors and the effect of bad pixels. If part of the emission (e.g. extended galaxy emission) was in the chip gap, we made sure to dither at least $10''$ east or west to prevent those locations from ending up in the chip gap for all 3 observations. For SOI, filters are installed in two filter wheels which hold up to five filters in each wheel. We used the standard SOI pixel binning of 2×2 because the binned pixel size ($0.15''$ pixel^{-1}) is still much smaller than the natural seeing (0.7-$1''$, so the point spread function (PSF) remains well sampled.

In fall 2010, William Sparks of STScI, through a grant from the Director's Discretionary Research Fund at that same institution, purchased a set of four linear polarizing filters (0°, 45°, 90°, 135°) to introduce a polarimetry mode for SOI. The 0° and 90° filters are cut from the same piece of glass as are the 45° and 135° filters. Since there are two filters (i.e. a polarizer and a narrowband or broadband filter) in the light path instead of one, the telescope focus is different than the focus with a single filter. Typically, the focus offset is about -100 ± 20 units from the focus setting for a single filter when a polarizer is in place. The focus was regularly monitored throughout the night and typically re-tuned twice during the first half of the night while the temperature inside the dome changed more rapidly, and a third time during the second half of the night. Prior to our November 23^{rd} 2011 night, we did not determine a separate focus which caused images which are slightly out of focus. The focusing error was originally missed as the seeing during those nights was poor ($> 1''$) which made it difficult to determine that a focus offset was needed. Data used in this chapter were acquired during three observing nights, only one of which is prior to November 23^{rd} 2011. The dates of the individual observations, filter selection, and exposure times are listed in Table 4.1. Since the experiment is a matter of determining small differences between paired observations, observations were reduced and analyzed separately for each night to independently verify polarization measurements and avoid being affected by significant changes in observing conditions.

Table 4.1. Polarization Observations.

Target (—)	α**(2000)** (—)	δ**(2000)** (—)	**Filter** (—)	**Exposure Time**[a] **(seconds)**	**Night Observed** (—)
Unpolarized Standards					
NGC 1851	$05^h14^m06.7^s$	$-40^\circ02'48''$	V	30×3	January 4th, 2013
			R	30×3	January 4th, 2013
			V	60×3	April 6th, 2013
			R	60×3	April 6th, 2013
NGC 1866	$05^h13^m39.1^s$	$-65^\circ27'56''$	V	60×3	April 6th, 2013
			R	60×3	April 6th, 2013
Polarized Standards					
HD110984	$12^h46^m44.83^s$	$-61^\circ11'11.58''$	V	2×3	April 7th, 2011
			V	2×3	April 6th, 2013
Crab Nebula	$05^h34^m32.0^s$	$+22^\circ00'52''$	V	120×3	January 4th, 2013
R Monocerotis	$06^h39^m09.95^s$	$+08^\circ44'09.7''$	V	60×3	January 4th, 2013
BCG Science Targets					
M87	$12^h30^m49.4^s$	$+12^\circ23'28''$	6600-75[b]	600×2	April 7th, 2011
			6129-140[c]	600×2	April 7th, 2011
			6600-75[b]	600×2	April 6th, 2013

---

[a] Exposure times are in the form N×M, where N is the time in seconds for each exposure and M is the number of dithers.

[b] This filter was used for a narrow band Hα filter for this target.

[c] This filter was used for a narrow band continuum filter for this target.

The four polarized filters were placed in the filter wheel closest to the sky. The filter wheel with the four polarizers had one open filter position to preserve the ability to take observations without a polarizer. The second wheel was used for up to five narrow or broadband filters. We used the broadband Bessell V and R filters regularly available on SOI as well as additional filters from the CTIO narrow band filter collection[2]. For a given science filter and dither position, exposures were taken in a consistent order (0°, 90°, 45°,then 135°). Additionally, all observations for a position were taken before dithering to the next position. For example, a galaxy requiring a Hα filter and a continuum filter had a series of four images taken with the Hα filter and each of the polarizers, then the continuum filter with each of the polarizers, and then moved to the next dither position to repeat the sequence. The paired observations through polarization filters differing by 90 degrees were taken as close as possible in time sequence to reduce the likelihood of intermittent weather affecting the measurement of the Stokes parameters. Statistically significant variations in the flux of unpolarized stars is an indication of clouds; these observations were not used in our analysis. Additionally, Stokes parameters were determined independently from each pair of observations and could be compared to Stokes parameters derived from subsequent dither sets. If one pair was significantly affected by clouds it was rejected from analysis.

4.3 Calibration and Data Analysis

4.3.1 Stokes Parameters

We used Stokes parameters to calculate the polarization percentage as well as direction of the electric field vector. The linear polarization vector drawings in Figure 4.3 as well

---

[2] http://www.ctio.noao.edu/instruments/filters/

as the following polarization equations are reproduced from Collett [2005]. S$_{LHP}$, S$_{LVP}$, S$_{L+45P}$, S$_{L-45P}$ are equivalent to the images taken with 0, 90, 45, and 135 degree polarizers, respectively. Using these four images we can calculate the following quantities:

$$Q = \frac{S_{LHP} - S_{LVP}}{2} \tag{4.1}$$

$$U = \frac{S_{L+45P} - S_{L-45P}}{2} \tag{4.2}$$

$$I_0 = \frac{S_{LHP} + S_{LVP} + S_{L+45P} + S_{L-45P}}{2}. \tag{4.3}$$

With the four images, the Stokes parameters Q and U can be measured independently. Similarly, independent measurements of I_0 can be made from:

$$I_{0+90} = S_{LHP} + S_{LVP} \tag{4.4}$$

$$I_{45+135} = S_{L+45P} + S_{L-45P}. \tag{4.5}$$

This comparison is important to test whether changes in the observing conditions happened on a short enough timescale to affect the relative flux from the source between the set of four images, independent of the sources polarization. From Q, U, and I_0 the polarization degree P as well as the polarization angle θ are:

$$P = \frac{Q^2 + U^2}{I_0} \tag{4.6}$$

$$Q = I\mathrm{cos}(2\theta) \tag{4.7}$$

$$U = I\mathrm{sin}(2\theta) \tag{4.8}$$

$$\theta = 1/2\mathrm{tan}^{-1}(\mathrm{U/Q}). \tag{4.9}$$

Since the inverse tangent function is bounded between (-$\pi/2$, $\pi/2$), the relative signs of the Stokes parameters Q and U can be used to convert the calculated angles to angles between 0° and 180°. We also compute the standard deviations for each of these parameters by using standard propagation of error:

$$\sigma_Q = \frac{\sqrt{\sigma^2_{S_{LHP}} + \sigma^2_{S_{LVP}}}}{2} \tag{4.10}$$

$$\sigma_U = \frac{\sqrt{\sigma^2_{S_{L+45}} + \sigma^2_{S_{L-45}}}}{2} \tag{4.11}$$

$$\sigma_{I_0} = \frac{\sqrt{\sigma^2_Q + \sigma^2_U}}{2} \tag{4.12}$$

$$\sigma_P = \frac{\sqrt{(Q\sigma_Q)^2 + (U\sigma_U)^2 + (\sigma_{I_0} P^2 I_0)^2}}{P I_0^2}. \tag{4.13}$$

Additionally we can measure the standard error on the mean of each of these quantities using the form $\sigma/\sqrt{n}$ as all Stokes parameters and regions are taken over identical areas. For

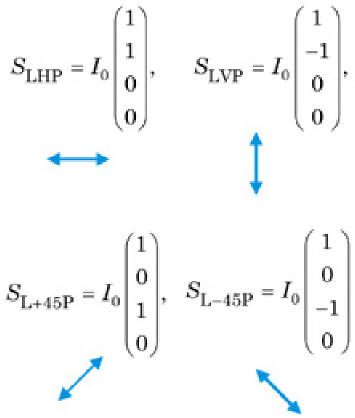

$$S_{\mathrm{LHP}} = I_0 \begin{pmatrix} 1 \\ 1 \\ 0 \\ 0 \end{pmatrix}, \quad S_{\mathrm{LVP}} = I_0 \begin{pmatrix} 1 \\ -1 \\ 0 \\ 0 \end{pmatrix},$$

$$S_{\mathrm{L+45P}} = I_0 \begin{pmatrix} 1 \\ 0 \\ 1 \\ 0 \end{pmatrix}, \quad S_{\mathrm{L-45P}} = I_0 \begin{pmatrix} 1 \\ 0 \\ -1 \\ 0 \end{pmatrix}$$

Figure 4.3 Stokes Parameters. The four linear polarization Stokes parameters are shown. S$_{LHP}$, S$_{LVP}$, S$_{L+45P}$, S$_{L-45P}$ are equivalent to the images taken with 0, 90, 45, and 135 degree polarizers, respectively. Using these four images we can calculate the Stokes parameters Q, U, and I$_0$. Where $Q = \frac{S_{LHP} - S_{LVP}}{2}$, $U = \frac{S_{L+45P} - S_{L-45P}}{2}$, and $I_0 = \frac{S_{LHP} + S_{LVP} + S_{L+45P} + S_{L-45P}}{2}$.

low values of polarization, degree of polarization is biased because it is a positive definite quantity. To compensate for this fact, a bias term ΔP can be subtracted from the measured polarization degree such that:

$$P_{unbias} = P - \Delta P \tag{4.14}$$

$$\Delta P = \sqrt{\sigma_Q^2 + \sigma_U^2}. \tag{4.15}$$

We allow this unbiased measure to be negative to keep our distributions symmetric.

4.3.2 Image Reduction

The images were initially reduced through the SOAR pipeline[3] written by Nathan DeLee. The SOI pipeline is a collection of *"IRAF CL"*[4] scripts that will subtract the zero-length

---

[3] `http://khan.pa.msu.edu/www/SOI/`

[4] IRAF (NOAO) V2.16 `http://iraf.noao.edu/`

exposure CCD bias then normalize the image based on the variation of the pixel-to-pixel response. The original image is a multi-extension FITS file from two CCD segments (four total extensions), which is combined into a single file corresponding to a simple FITS file with a physical chip gap. We edited the scripts from a previous version to allow for flat fielding using a dome flat with a polarizer and a science filter. We edited the image header World Coordinate System terms using a Two Micron All-Sky Survey (2MASS) star in the field as an astrometric reference star and confirmed the offset using other 2MASS stars in the field. Individual exposures were aligned and trimmed using the IRAF task imalign. Cosmic rays were removed using the L.A. Cosmic Laplacian edge detection routine [van Dokkum, 2001], which typically flags <1% of stars as cosmic rays while correctly identifying $\sim$ 98% of cosmic rays. Prior to taking observations of scientific targets, we take calibrations from a variety of sources. In addition to bias frames and dome flats, we acquire sky calibrations including: unpolarized standard stars, globular clusters, polarized standard stars, and polarized diffuse nebula. We use polarized and unpolarized standards (both stars and extended sources) from Turnshek et al. [1990].

4.3.3 Dome Flats

For a dome flat, a light is projected onto a white screen such that the light is scattered and should be unpolarized. Twilight flats, on the other hand, can be highly polarized (especially if taken with the telescope pointed opposite the direction of the setting or rising sun, as often is done) and therefore will be unreliable for use as a calibration source. The dome flats were taken for all combinations of astronomical filters and polarization filters used. We reduce the images by flat fielding with all matching combinations. To verify the flat field correction and quantify the errors on the correction, we observe unpolarized standard stars and globular clusters. We test the ratios of the 0 and 90 degree polarizers and the 45 and 135 degree polarizers using normalized dome flats in Figure 4.4 from the January 4th, 2013 night. The normalized dome flats are compared to verify there is no pixel-to-pixel variation in sensitivity to polarized light. We also compare the ratio of normalized V band 0 degree image from January 4th and June 4th 2013 in Figure 4.5. In both figures and both sets of filters there is a spread of ∼0.6% in the per pixel ratio and the ratios are also statistically consistent with one, similar to the spread in the individual, pre-combined flat images. However, we are unable to use the current dome flats to verify the telescope and dome flat light do not cause polarization at an overall throughput level.

To test whether there is an overall throughput polarization caused by the telescopes or dome flats we will need to take flats with the same filter configuration while rotating the camera assembly 90° and then back to the original orientation. The 90° rotation will verify whether the throughput of the telescope is polarized as the throughput for each polarizer should be equal to itself with a 90° rotation. Taking an additional observation back in the original orientation will verify that any differences in the rotated dome flats are not due to stability/variability in the brightness of the dome flat lamp itself. We plan to conduct this last test prior to prepping this work for publication, beyond the timescale for this thesis. For this work, we have controlled for any intrinsic polarization by observing unpolarized star fields as a null control, which we describe in the next section.

4.3.4 Unpolarized Calibration Targets

We observed unpolarized standard stars as well as globular clusters to estimate the zero point correction for the polarizers. We used the globular clusters as examples of unpolarized extended sources. Even though globular clusters are mostly unpolarized, some of the stars

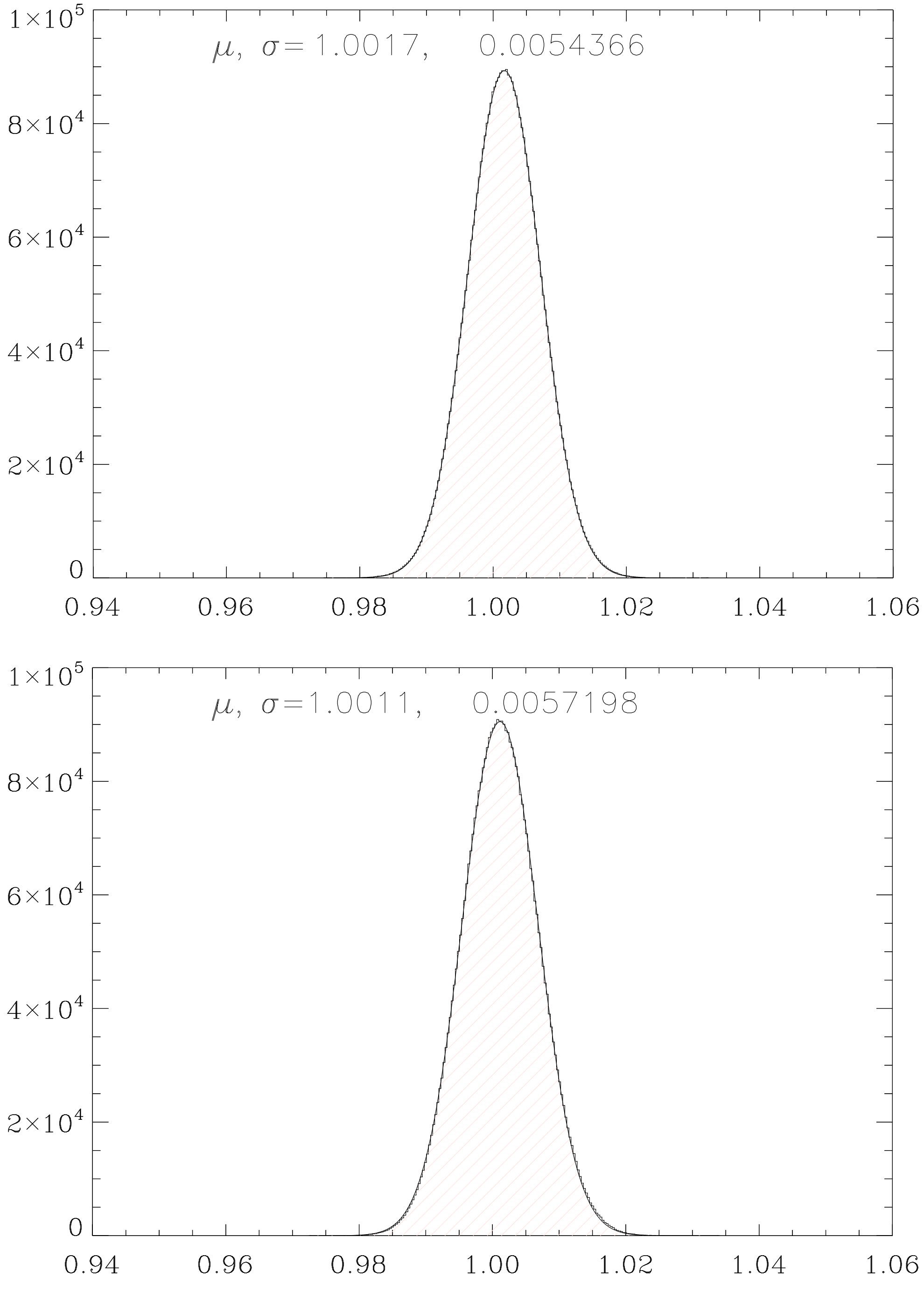

Figure 4.4 Single Night Dome Flat Comparison. We test the ratio of normalized dome flats to check the potential pixel to pixel variation in polarization. The upper histogram is a ratio of the normalized 0° and 90° flats and the lower histogram is a ratio of the normalized 45° and 135° flats for the V band filter from January 4$^{\mathrm{th}}$, 2013. The curve overlaying the shaded histogram is the Gaussian fit for the distribution. The mean (μ), and standard deviation (σ) are included in each of the figures.

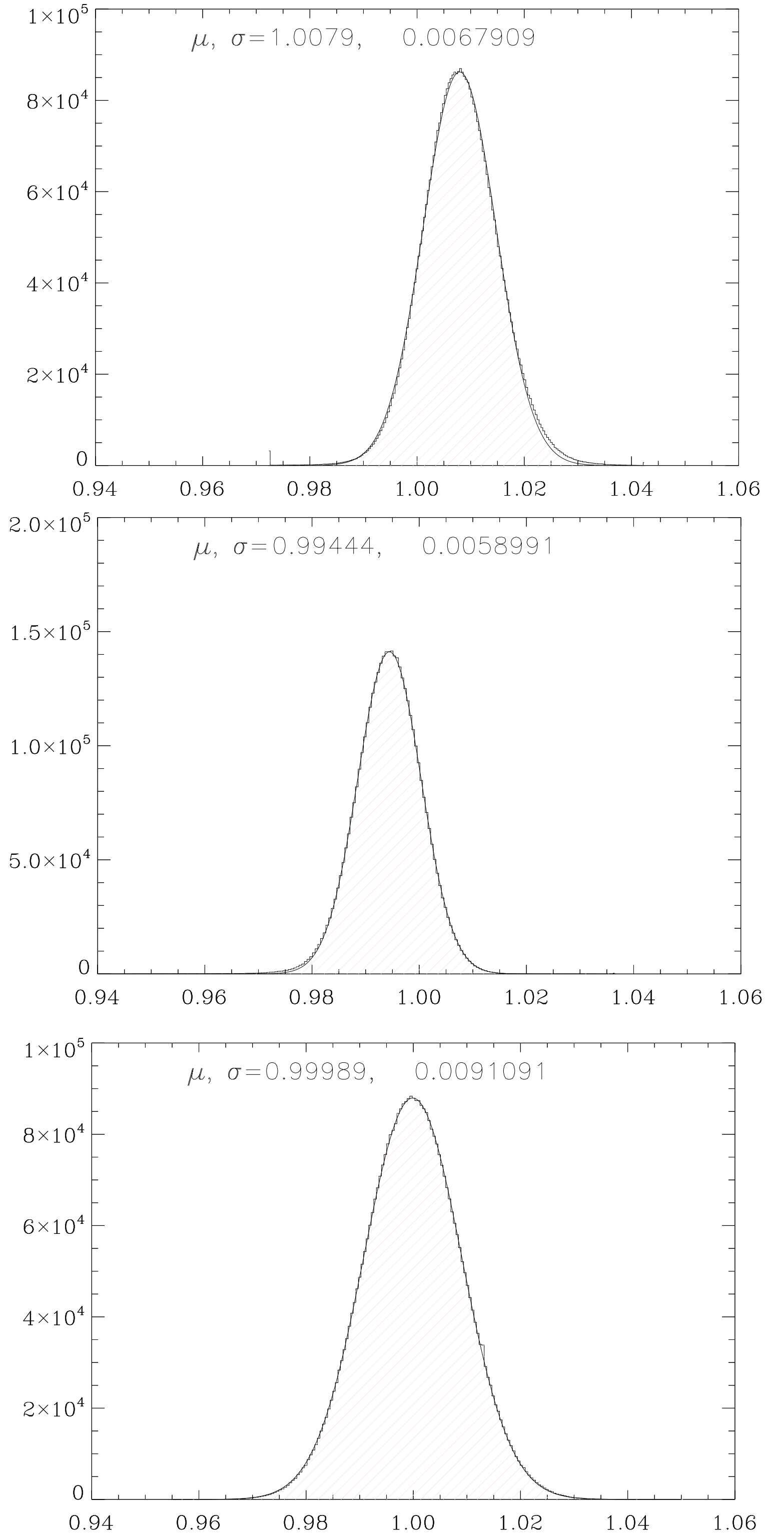

Figure 4.5 Multiple Night Dome Flat Comparison. We test the ratio dome flats between January 4th and June 4th 2013 for the V band polarization filters. The upper figure compares the normalized 0 degree images and the middle figure compares the normalized 45 degree images. The lower figure compares two individual 0 degree dome flats before they have been averaged.

or regions of the globular cluster may have a small amount of polarization both intrinsic to the globular cluster as well as part of the line of sight interstellar medium signal. Therefore, in our investigation of the variability of the polarization signal as a function of position on the filter, we use stars extracted from multiple globular clusters. Stars are found in each of the images using the IRAF DAOPHOT package for unsaturated detections $>100\sigma$ ($<1\%$ error). For the globular clusters we observed, typically 500-2000 stars were found in each image and a majority of those stars had matching pairs.

We plot the distribution of the $0° - 90°$ and $45° - 135°$ relative fluxes in Figure 4.6. We find multiplicative correction factors with respect to the 0° image of 0.9725 ± 0.00036, 0.9488 ± 0.00039, and 1.0085 ± 0.00095. The difference between the V and R band corrections was found to be at most 1.5%.

For our science observations we use bright unsaturated stars in the field to compute the correction factor between the polarizers as these should be a more accurate representation of that current field in current conditions. If any correction factors are significantly different than the ones found in from the globular clusters, those observations were not used because a significant difference would mean that clouds or other conditions affected one or both observations in a pair. As a check on the correction as well as photometric differences, we compute the total intensity in our apertures but separately summing the $0° - 90°$ and $45° - 135°$ pairs. We find the differences are typically in agreement to $\sim$1%. We compute a mean standard error for the correction factor based on the mean correction from multiple stars.

The initial error map is the Poisson error on the counts (converted to electrons by applying the SOI gain of 2 e^- ADU^{-1}) and adding the per pixel read error of 4.4 e^- per exposure and the error on the correction factor in quadrature. We then chose sky background regions which were in the same position of the sky for each set of polarizers. Typically we used circular areas at least $30''$ across to reduce the error across the images. The initial error (in electrons) for N pixels is:

$$\sigma = \sqrt{(2I)^2 + N4.4^2 + N^2\sigma_{corr}^2/N_{stars} + N^2\sigma_{bg}^2/N_{bg}}, \tag{4.16}$$

where I is the total number of counts, σ_{corr} is the standard deviation in the correction factor, N_{stars} are the number of stars used in the correction factor, σ_{bg} is the standard deviation in the background and N_{bg} is the area used to compute the background.

4.3.5 Polarized Calibration Targets

We analyzed polarized standard stars using the same procedure as the unpolarized standard star procedure. By comparing our measurements to the published measurements for the polarization standard provides an estimate of the accuracy of our estimated polarization fraction as well as the accuracy of the angle of the polarization vector. Typically, these stars are shrouded by dust which can change over year timescales and create a variable signal making both the measurement of polarization fraction as well as angle difficult to obtain consistent measurements. Therefore, we used diffuse nebula emission and the AGN jet in M87 as additional polarized calibrations to ensure we were able to faithfully reproduce strongly polarized sources.

We created Stokes parameter images with an IDL code written for this project. The code also calculates error maps of each parameter. We typically applied small binning (2×2 or 4×4 above the $0.15''$ pixels) to the data with the CONGRID IDL routine to improve the signal to noise level of detections and did not interpolate across cells to conserve flux and

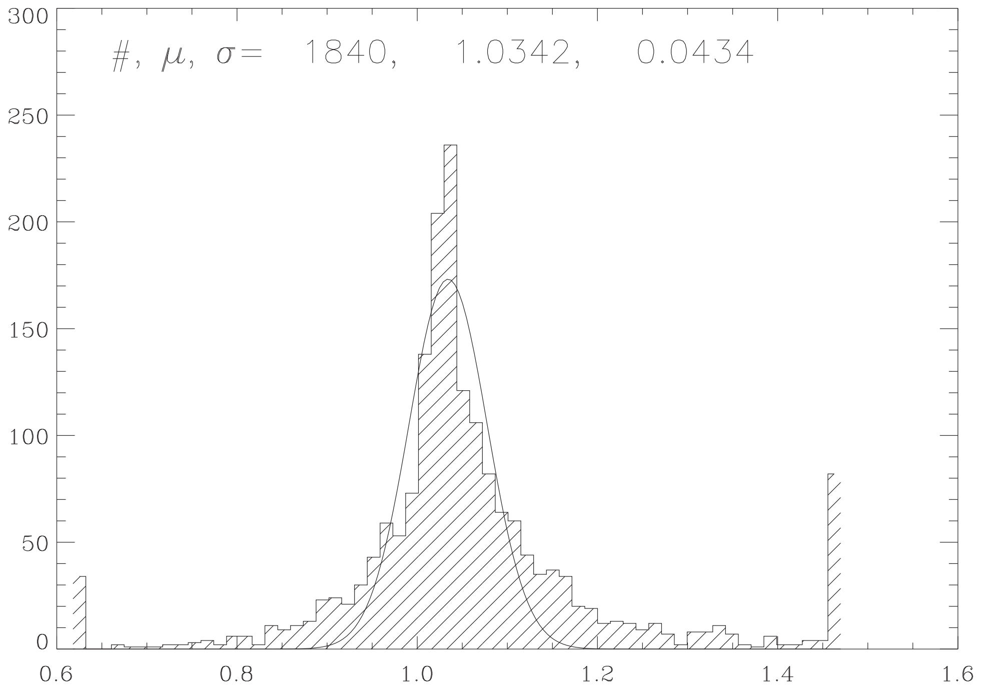

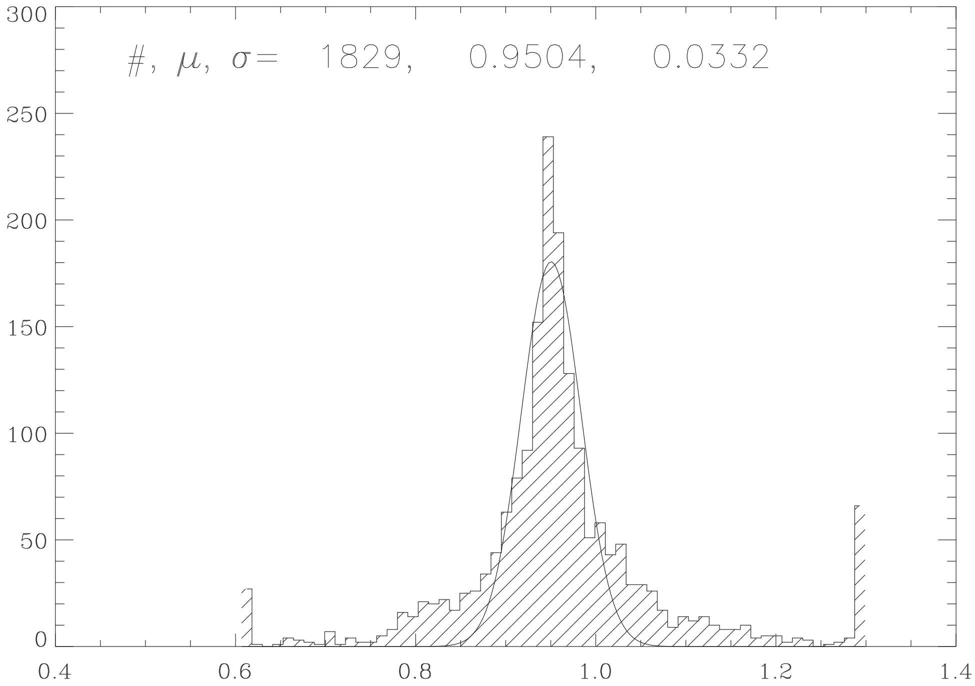

Figure 4.6 Globular Cluster Polarziation Comparison. We present globular cluster polarization difference histograms for NGC1851. The upper plot is for the $0^\circ - 90^\circ$ comparison and the lower plot is for the $45^\circ - 135^\circ$ comparison. The curves overlaying the shaded histograms are the Gaussian fit for the distribution. The number of stars (#), mean (μ), and standard deviation (σ) are included in each of the figures.

to maintain the noise properties from cell to cell which works well on our diffuse polarized emission. As well as images for each of the Stokes parameters I, Q, and U, we create maps for the fractional polarization and and for the signal-to-noise ratio of the fractional polarization. For the creation of polarization-fraction vectors, we impose a minimum S/N (i.e. I_P/σ_{I_P}) ratio of 5 is used. We present images of the Crab Nebula and show the output of the Bessell V images in Figure 4.7.

The Crab Nebula (M1) is a pulsar wind nebula with a very high polarization (∼25%) which has had its optical polarization mapped many times [Woltjer, 1957, Wilson, 1974, Schmidt et al., 1979, Hickson and van den Bergh, 1990]. We plot the polarization maps created with our IDL code for the Crab Nebula V band images in Figure 4.7 which include: the intensity image, the Stokes Q map, the Stokes U map, the polarization fraction map, and the signal to noise map. The chip gap is still visible along the center because these were made from a single observations. Only the scale bar for the signal to noise plot is included to give an if which areas that are not black that have a signal to noise ratio at least 5. We compare our electric field polarization map to the magnetic field polarization map in Hickson and van den Bergh [1990] in our Figure 4.8. We only plot vectors which have at least a signal-to-noise (i.e. P/P$_{err}$) greater than 5. Our vectors are orthogonal to theirs because of the orthogonality of the electric and magnetic field components of the light from Maxwell's equations. We make a quantitative comparison using two nebular regions in the Crab which are polarization calibration targets in Turnshek et al. [1990], presented in Table 4.2. For the Crab Nebula, a strongly polarized nebula, we find that the measurements for the individual observations are consistent, but in a couple cases are four to five percentage points (∼20%) different than the values from Turnshek et al. [1990], a difference larger than the measurement error. The measured angles are typically within the measured error of the

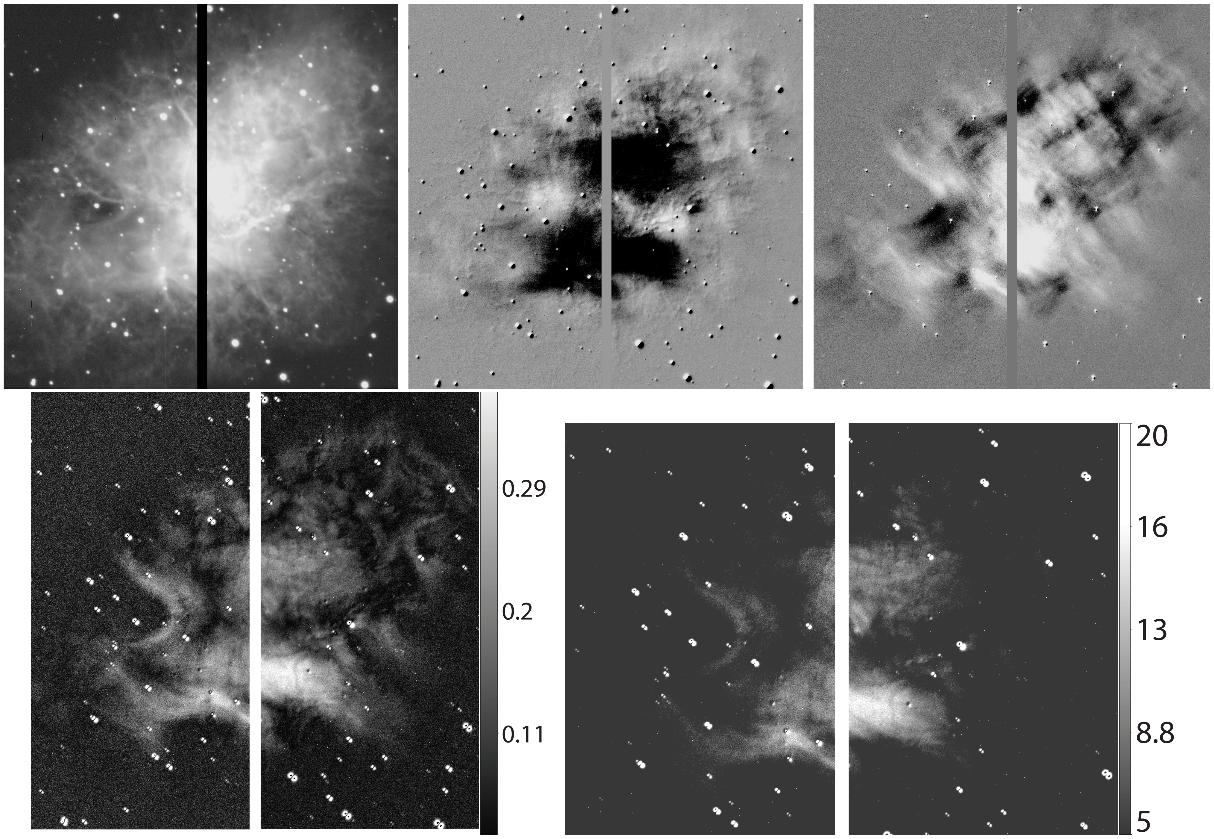

Figure 4.7 Crab Nebula Polarization Images. We include V band images of the full 50×50 field of the Crab Nebula from our January 4th, 2013 night. The stripe down the middle is the chip gap present in individual observations. From upper left to lower right, the figures are: Total intensity image, Stokes parameter Q image, Stokes parameter U image, Polarization percent image, and signal to noise image. In the Polarization percent image, the gradient range scale represents a percentage polarization between 2% and 40%. In the signal to noise image, the gradient range scale represents a signal to noise between 5 and 20.

standard value and within 2° of the standard value.

R Monocerotis is a T Tauri star which is part of the diffuse nebula NGC 2261. Given the youth of the star (300,000 years) the polarization vectors can change on very short timescales (a few years) due to the variability of the nebula [Johnson, 1966]. Polarized standard stars, like R Monocerotis (R Mon), typically have circumstellar dust which induces polarization on their light. The star in the nebula R Mon is a good test because the polarization of the emission in the nebula forms a ring around the star. In Figure 4.10 we compare the polarization map of R Mon to the map in Close et al. [1997] to show that the polarization angles which make a radial arcs north of the star are consistent. We make a quantitative comparison, presented in Table 4.2, using three nebular regions in RMon which are polarization calibration targets in Turnshek et al. [1990].

Table 4.2. Extended Polarization Standards

Source (—)	RA (2000)	Dec (2000)	Aperture ($''$)	P_V (%)	θ_V (deg)	Ref. P_V (%)	Ref. θ_V (deg)
Crab Nebula - 1	$5^h34^m33.01^s$	$+22°00'40.0''$	$5.3''$	16.61%±0.91%	160.7° ± 0.7°	21.45%±0.50%	160.7°
Crab Nebula - 2	$5^h34^m33.14^s$	$+22°00'13.5''$	$5.3''$	31.20%±0.32%	168.6°±0.4°	29.68%±0.61%	170.6°
Rmon - 1	$6^h39^m09.98^s$	$+8°44'41.4''$	$5.3''$	17.91% ± 0.42%	90.3° ± 1.7°	14.52%±0.47%	89.9°
Rmon - 2	$6^h39^m10.75^s$	$+8°44'27.7''$	$5.3''$	10.38%±1.22%	133.1° ± 1.0°	13.78%±0.45%	118.1°
Rmon - 3	$6^h39^m09.98^s$	$+8°44'23.7''$	$5.3''$	10.95%±0.88%	84.8° ± 3.4°	11.90%±0.47%	87.7°

Note. — We use Turnshek et al. [1990] for our reference.

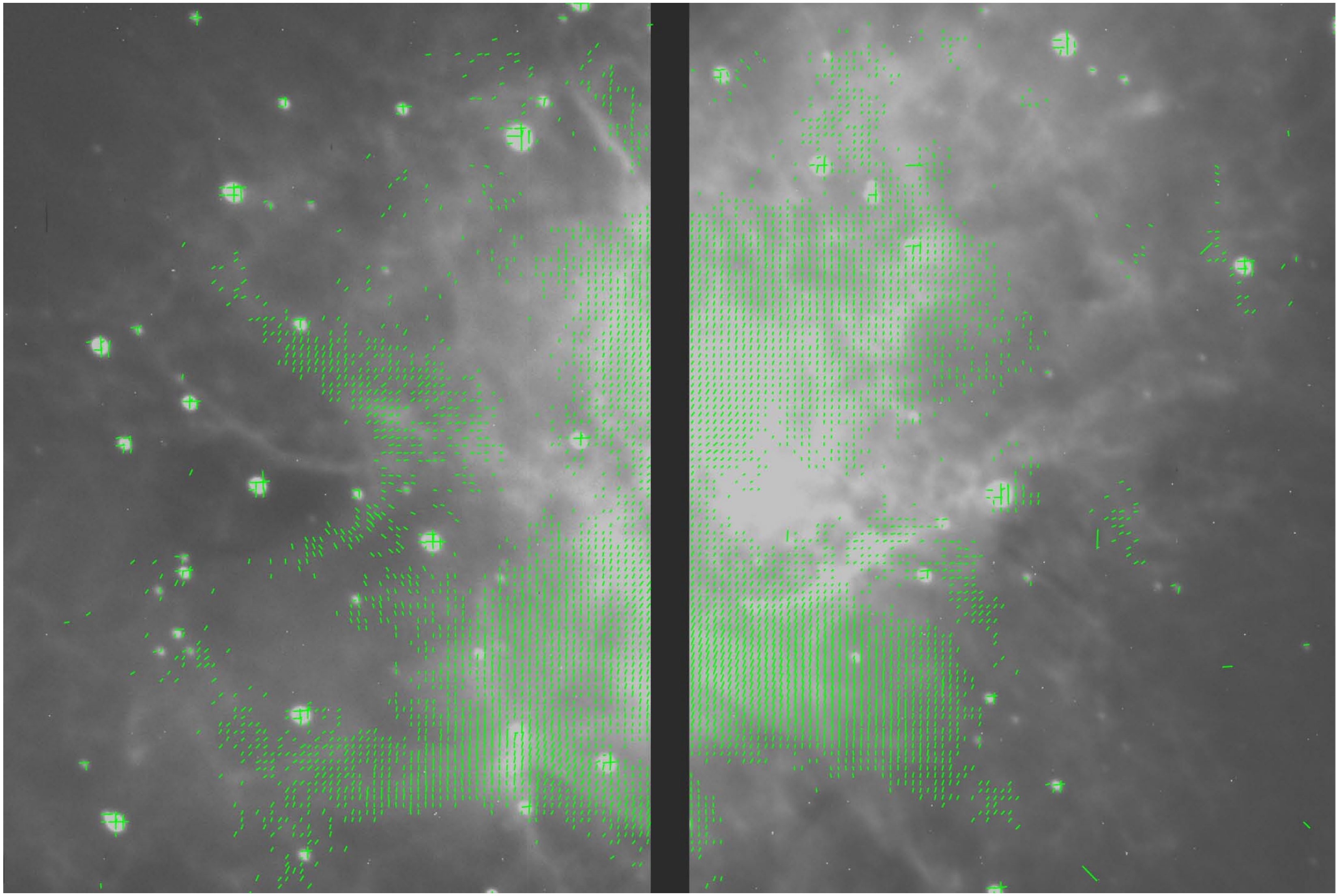

Figure 4.8 Crab Nebula Polarization Vectors. Our 5′×5′ intensity image for the Crab Nebulae, overlayed with polarization electric field lines calculated on the 2″ × 2″ bins. The minimum polarization vector is 10%. We compare the SOAR image and the direction of the field lines to that of Hickson and van den Bergh [1990] in Figure 4.9.

For these two strongly polarized nebula we find that the measurements for the individual observations are consistent but in a couple cases are four to five percentage points (∼20%) different than the values from Turnshek et al. [1990]. The measured angles are typically within the measured error of the standard value and within 2° of the standard value. M87 (NGC 4486) is the brightest cluster galaxy in the nearby Virgo Cluster. It contains an AGN which is known to have a strongly beamed jet which has had its polarization observed optically with HST [Perlman et al., 1999]. To measure the polarization of the jet we took a series of V-band images of M87 and use the IRAF routine ellipse to subtract out elliptical isophotes of the galaxy. We do not mask the jet and instead rely on outlier rejection to avoid subtracting the jet. These surface brightness isophotes track well for M87 and similar large ellipticals because their starlight profiles are very smooth. We reproduce two figures from Perlman et al. [1999] and compare it to our polarization map for a similar region in Figure 4.11. The extracted region in our SOAR data is coincident with the AGN outflow $11''$-$18''$ (which are included in two separate figures in the Perlman et al. [1999] paper) from the center of the galaxy as seen in the HST image.

4.4 Polarization Limits of M87 Filaments

We investigate the polarization signature in the Hα filaments of the brightest cluster galaxy (BCG) M87. For continuum measurements we observed broadband V and R as well as narrow band CTIO 6129-140 which is off of Hα as well as other common emission lines found in BCGs. Similarly to the other polarization analysis, we analyze each night separately to verify the consistency of the measurements. We tried to bin the data 4×4 to improve the signal to noise while keeping the filamentary structure intact to make a polarization map similar

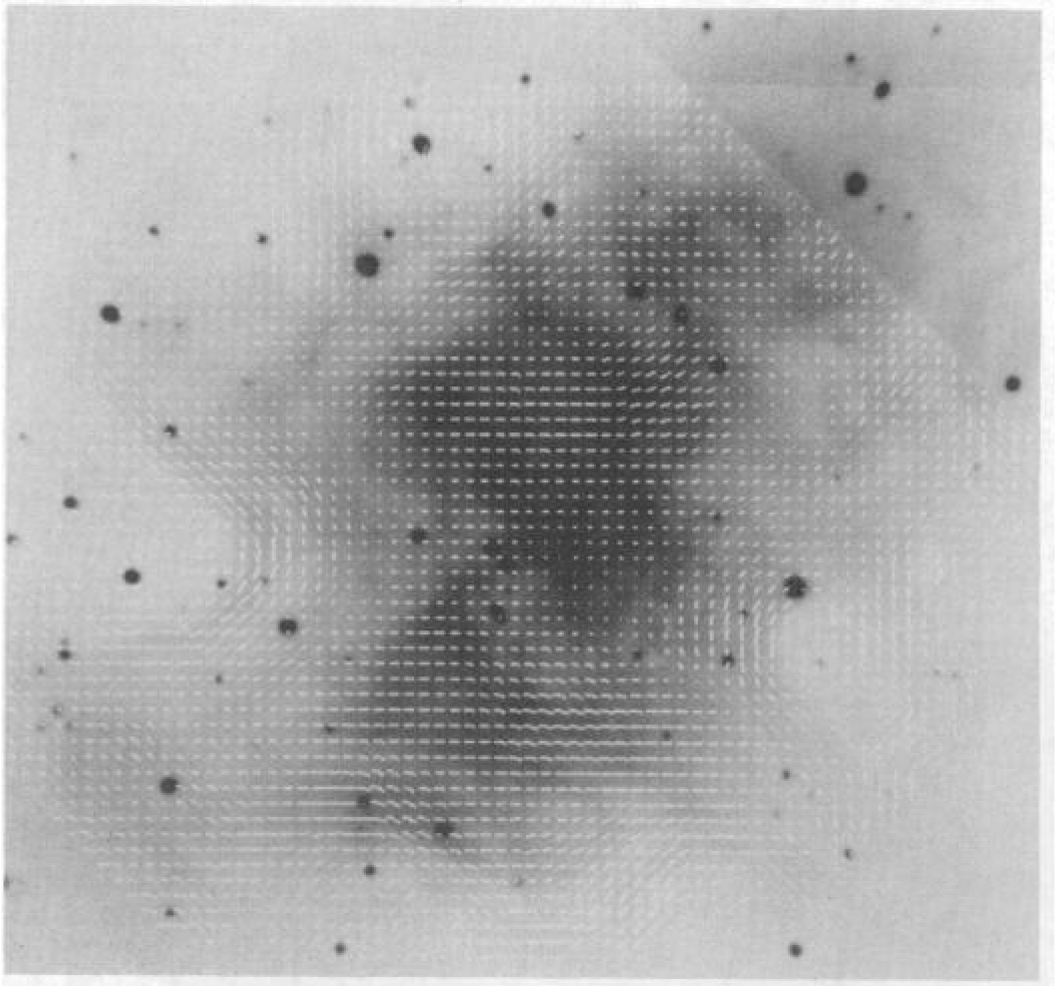

Figure 4.9 Hickson and van den Bergh [1990] Crab Nebula Magnetic Field Vectors. We reproduce Hickson and van den Bergh [1990] Figure 3 for a slightly smaller ($3.9' \times 3.7'$) field of the Crab Nebula. In the figure, the magnetic field lines are plotted instead of electric field lines. Their vectors are plotted with a polarization averaged from $2'' \times 2''$ bins. The $2''$ separation also corresponds to a 50% polarization vector.

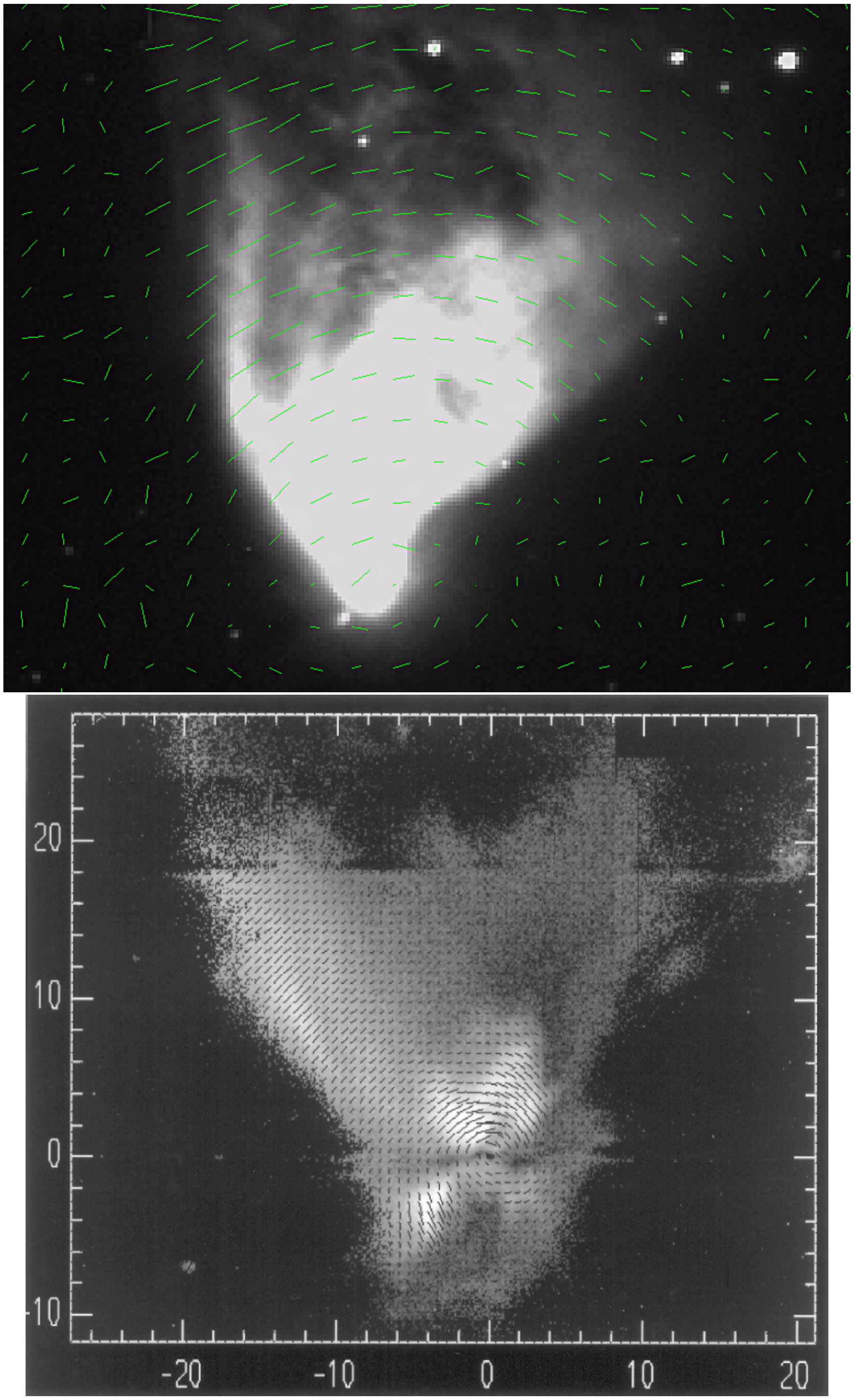

Figure 4.10 R Monocerotis Polarization Image. We compare our map of the polarized standard star R Monocerotis to the map in Close et al. [1997]. Notice the polarization vectors form a circle around the star near the bottom of the image. The rest of the polarization vectors in the nebula form a similar shape.

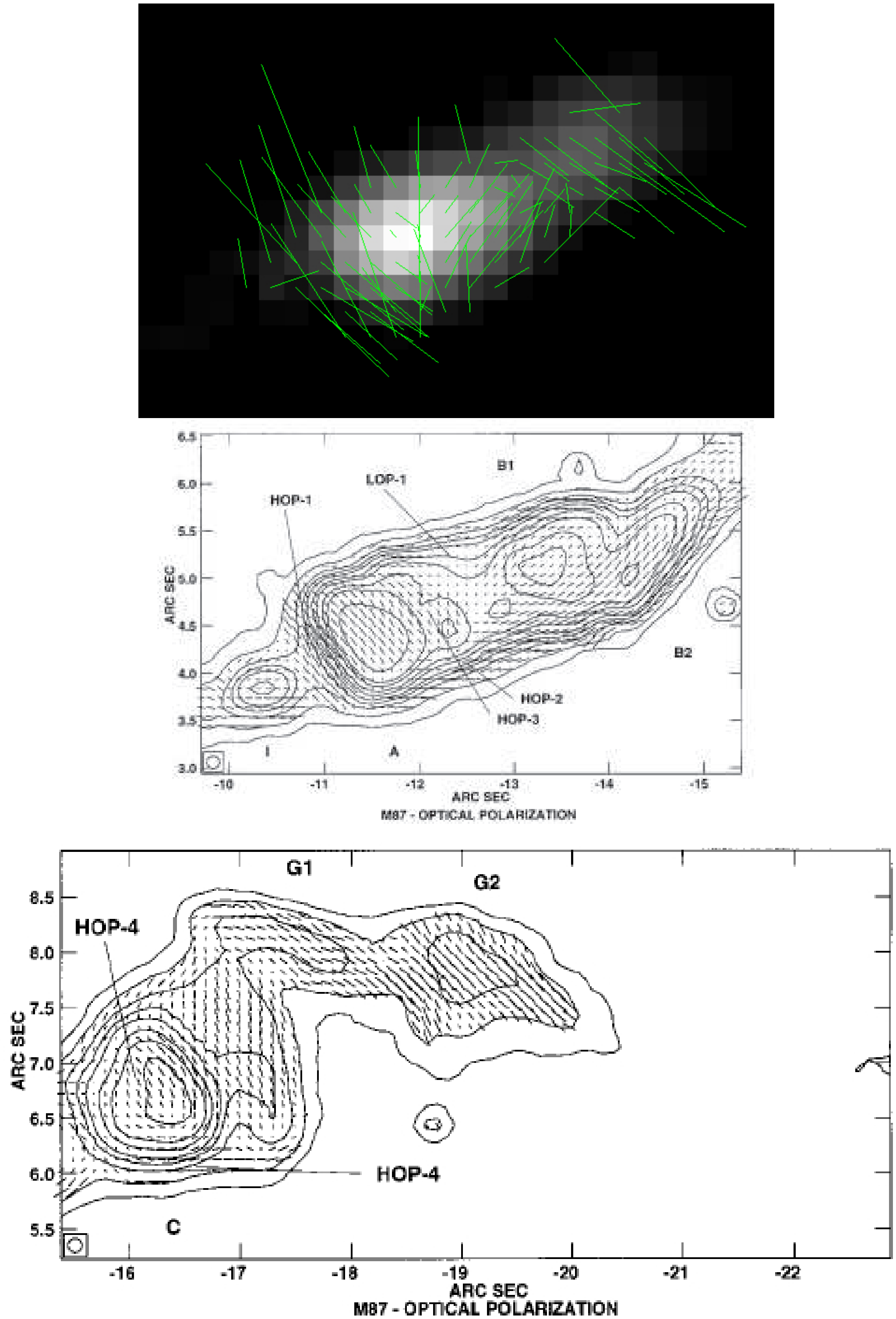

Figure 4.11 M87 AGN Polarization Comparison. We plot the polarization vectors on the intensity image of the M87 jet where we subtracted out elliptical profiles to remove the background galactic starlight. The plot to the right is a combination of two HST optical polarization maps from Perlman et al. [1999], which correspond to the relative regions in our map.

to the M87 jet, Crab, and R Mon. However, even at that resolution, the low level of signal to noise made it impossible to make a polarization map. Instead, we strategically extracted 65 $1.5'' \times 1.5''$ regions on bright regions of the filaments and computed Stokes parameters for each of the boxes. The locations of these boxes on the Hα filaments are shown in Figure 4.12. To create a control sample (i.e. regions which shouldn't have polarization) we extract 234 $1.5'' \times 1.5''$ regions north of the center of M87 in regions that are not on Hα filaments but have a similar number of raw counts per pixel such that the signal to noise for all regions are similar.

We determine the limits on the polarization of the filaments with two tests. First, in test 1, we examine the continuum emission as a control and verify it is consistent with zero net polarization. In test 2, we separately extract the Hα regions from the continuum regions and run the test with the Hα which has not been continuum subtracted, to improve the number of counts available. For test 1, we verified that the continuum regions are consistent between dither sets within a given night using the non-parametric, two-sample Kolmogorov-Smirnov (K-S) test. A small D statistic (equivalently a large p-value) indicated that the data from each dithered positions are consistent with having been drawn from the same distribution. However, even though the distributions are the statistically similar, there may be some differences in the relative photometry between each of the images such that the Q and U Stokes parameters may not have a distribution consistent with zero. In Figure 4.14 we show an example of this where the Q values of two different observations have a mean consistent with zero given the error while one of the U continuum measurements is not consistent. Additionally, a K-S test for the two observations which have a standard deviation larger than their mean may not come out to a null result because their means are on the opposite sides of zero, like in the case of Figure 4.13. With the K-S test we verify whether the continuum polarization distributions, which should have no net polarization, look statistically identical after a small mean value is subtracted. To correct for the offset in the means, we subtract each of the means from the distributions such that they are identically zero and can be compared. The results of the K-S test pairs for test 1 indicate a null result (i.e. $p > 0.10$) for all pairs of continuum control samples.

After the consistencies in the control sample fluxes were verified in test 1, we examined the distribution of the Hα boxes in test 2, the shaded regions in Figure 4.13. By eye it appears that, while noisy, the Hα region histograms align well with their respective continuum histograms. To be able to compare the Hα distributions, we corrected them for their continuum by subtracting the Hα histograms by their respective continuum means. The result for Q and U for one image are displayed in Figure 4.14. After the correction, the values are now consistent with zero. Therefore, we can determine the level of polarized emission in the Hα regions with respect to the continuum control regions, which should contain no polarized emission. In this case, after we correct for the continuum, we find that the distribution of polarization measurements in the Hα regions are consistent with no polarization.

We are also investigating if there are any specific regions that might contain polarization, so we must verify that there is no spatial trend even though the total distribution of the Hα filaments have a distribution centered on zero polarization. In Figure 4.15 we plot all Hα boxes for four separate images and color code them based on polarization fraction. The polarization fraction which is computed is the unbiased polarization fraction corrected using the continuum values; a process similar to what was done in for the corrected histograms. While their scales are not identical (typically -1% to 1% in polarization per pixel) no individual pixel, nor combination of clustered pixels, has a statistically significant polarization level. We estimate a limit on the polarization measured of the Hα filaments using the biased

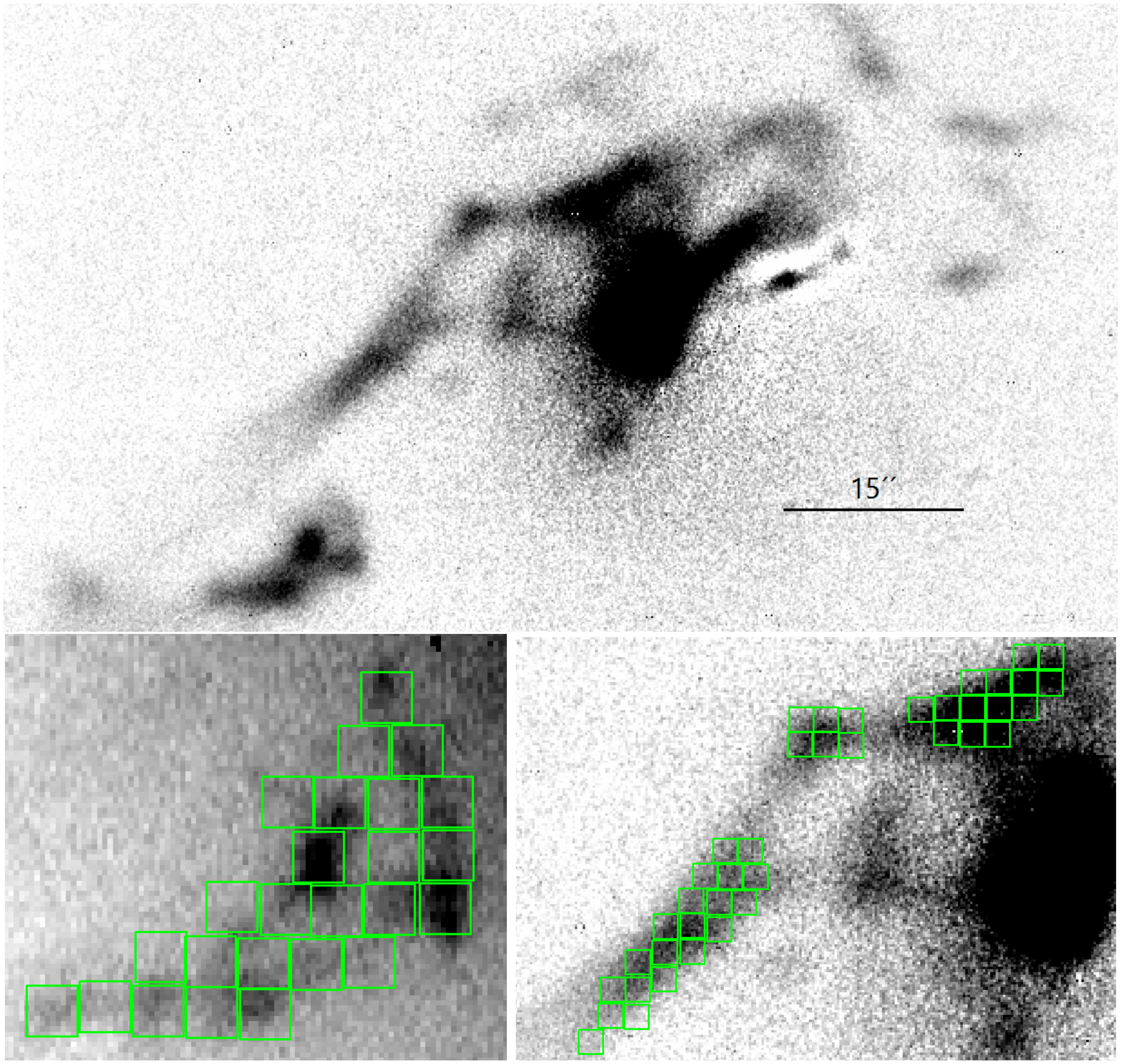

Figure 4.12 M87 Hα Polarization Fields. All three panels have their colors inverted such that darker areas are the areas of emission. The upper panel is the continuum-subtracted Hα image, which is a stacked image that includes 8 observations of four polarized images from two different dither positions from April 7$^{\text{th}}$, 2011. For M87, the $15''$ scale bar is equivalent to 1.35 kpc. The two lower panels are zoomed in areas of the upper image. The boxes are $1.5'' \times 1.5''$ boxes and were the regions used to measure Stokes parameters.

corrected uncertainties on the Hα Q and U histograms in Figure 4.14 as:

$$\sigma^2 = \frac{\sum_{i=0}^{N} \sigma_{Q_i}^2 + \sigma_{U_i}^2}{N}, \tag{4.17}$$

where N is the number of observations. We find a 3σ limit for polarization percentage in any of the individual $1.5''$ squares of 2.4%. The 3σ upper limit on the mean polarization over the entire filament covered by the these measurements is 0.3%, using the error on the mean for the 65 boxes.

4.5 Implications for the Filaments in M87

While we do detect significant polarization along the jet of M87 as well as at the nucleus, the off-nucleus Hα filament are noticeably polarization free. Sparks et al. [2014] has optical (450 nm to 900 nm) spectropolarimetry data for M87 from the VLT. Emission lines, including Hα from the off-nuclear filamentary regions of the galaxy are polarized $< 0.1\%$. These measurements, as well as our limits ($< 2.4\%$ for individual boxes, $< 0.3\%$ for the entire region) of the filaments, provide significant constraints on the possible mechanisms for the illumination of the off-nucleus Hα filaments. From deep observation of Abell 2597, Voit and Donahue [1997] used optical line ratios to show that shocks can't be a significant contributor to ionization and that the addition of photoionization from hot stars would also fall short of the total energy requirement. An additional contribution from something, like conduction from the hot ICM into the cooler filaments, a process which operates in regimes with strong temperature gradients, could make up this difference. For M87, the contribution from hot stars is limited as well because Sparks et al. [2009] found no hot stars in the vicinity of the south-east filaments that could account for UV flux needed to power the filaments. Instead, the only UV emission seen in the HST images was from a filamentary 10^5 K gas which was confirmed to be CIV (1549 Å) and HeII (1640 Å) line emission, by observations with the Cosmic Origins Spectrograph on HST [Sparks et al., 2012]. That emission is potentially an indicator of the intermediate temperature gas at the interface between the hot ICM and the cooler filaments. Therefore, thermal conduction is likely an important contributor to the structure and emission seen in M87, as well as other BCGs. However there is a debate whether the conduction is standard diffusive conduction or saturated conduction, a debate that can be resolved by examination of the polarization signal in the line emission filaments.

4.5.1 Thermal Conduction

Standard diffusive (i.e. Spitzer) conduction [Spitzer, 1962] is the process of thermal conduction where the heat is conducted by electrons in a fully ionized hydrogen plasma. The heat flux from conduction is:

$$q = -\kappa T, \tag{4.18}$$

where κ, the thermal conductivity is equal to:

$$\frac{1.84 \times 10^{-5} t_e^{5/2}}{\ln\Lambda} \text{erg s}^{-1}\text{deg}^{-1}\text{cm}^{-1}. \tag{4.19}$$

This form assumes that there are many collisions over the scale length of the temperature gradient, i.e. the mean free path is much smaller than the scale length. Under the conditions of Spitzer conduction, the hot electrons are able to heat the filaments isotropically, therefore, the emission is not expected to polarized. Cowie and McKee [1977] present a modification of Spitzer conduction in the regime where the mean free path of the electrons is much larger than the size of the interface. In this case normal Spitzer conduction reaches a maximum

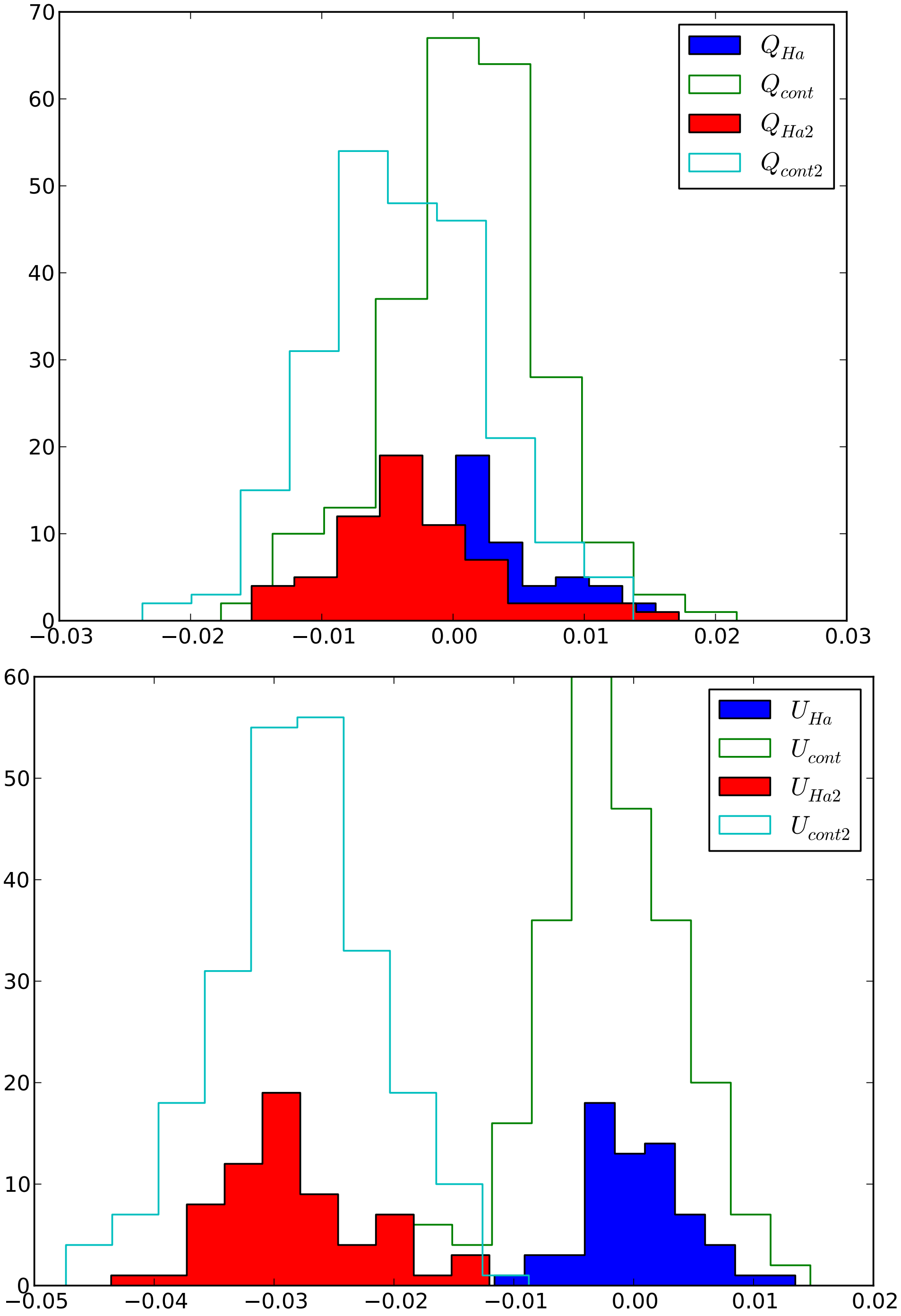

Figure 4.13 M87 Continuum Stokes Parameters. The histograms plot the Q and U Stokes parameter distributions for the 234 scaled (i.e. divided by the total counts in the respective pair of polarizers) continuum boxes ($1.5''$ on a side squares) as well as the 65 Hα boxes of identical size in M87. The centers of these distributions are not shifted. The two different indexes refer to two different pointings in April 2011. We see that in each pointing, while the distributions for each pointing are offset the Hα and continuum distributions for each pointing are aligned.

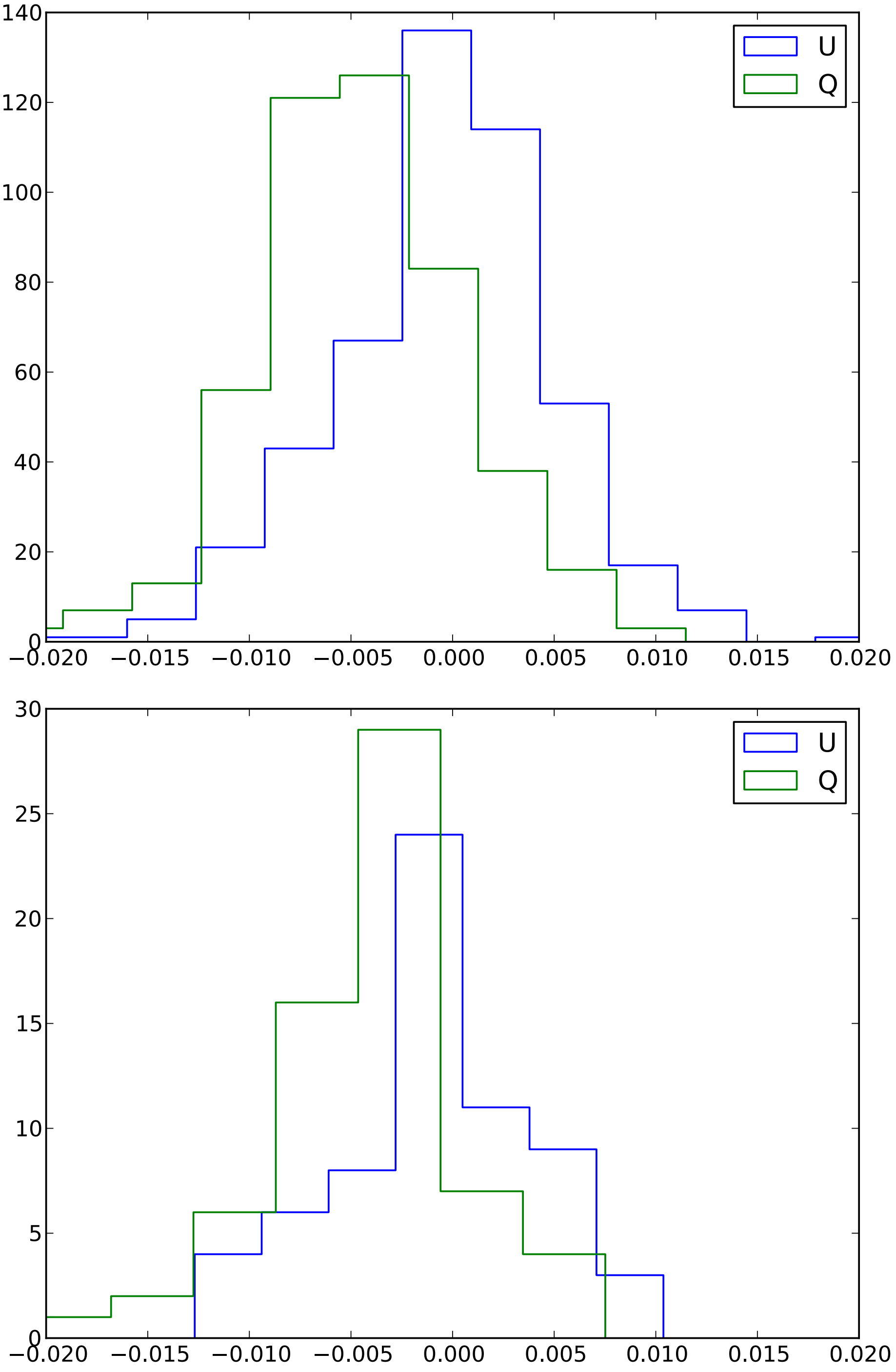

Figure 4.14 M87 Hα Stokes Parameters. The left histograms includes the scaled (i.e. divided by the total counts in the respective pair of polarizers) Q and U Stokes parameters for the continuum 1.5$''$ on a side squares. The right graph presents the equivalent for the sampling of 65 Hα 1.5$''$ on a side squares where the each of the distributions has been aligned by subtracting the means of the continuum Q and U.

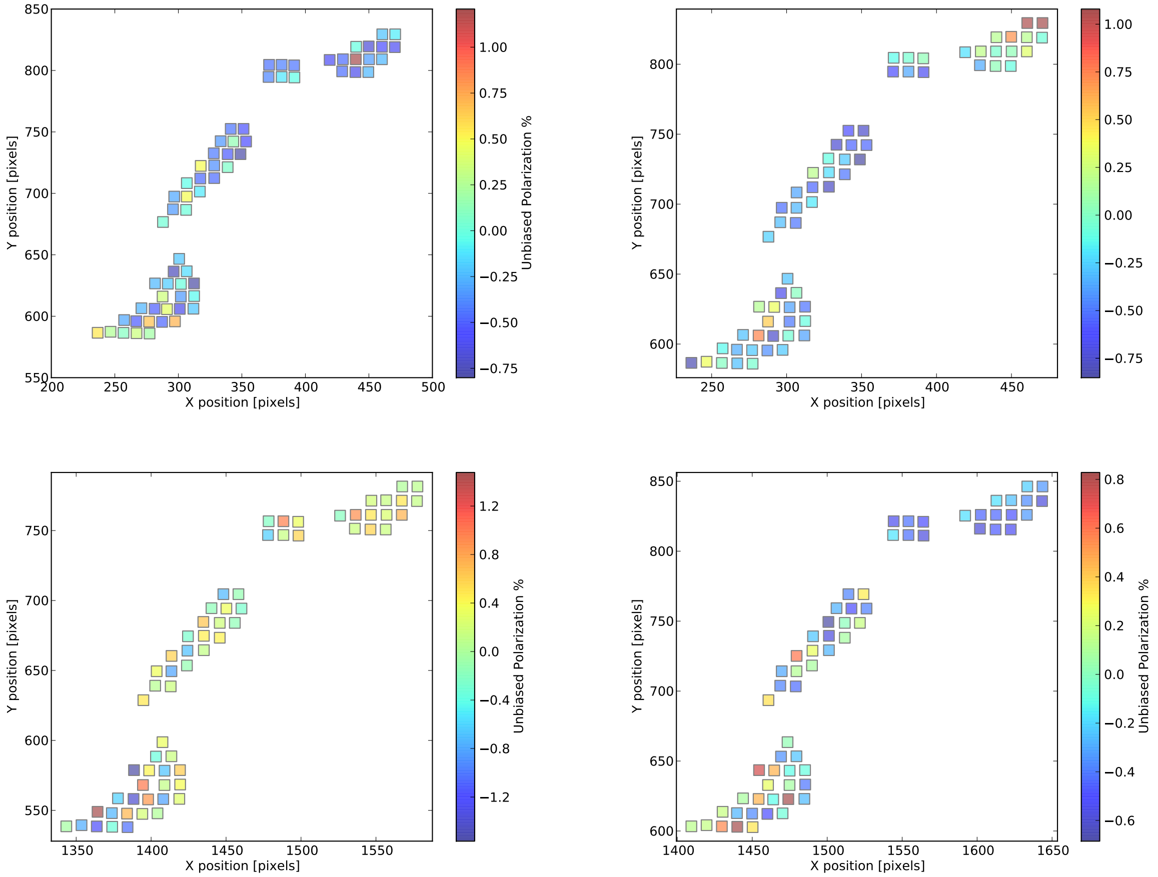

Figure 4.15 M87 Hα Region Polarization. We plot photometry differences between polarizers divided by the mean in each of the square apertures as an estimate of polarization fraction. The top two boxes are from observations from April 2011 and the bottom two are from April 2013. The calculated fractions are unbiased by subtracting the mean of the distribution for the continuum. We allow the fractions to be negative (which are consistent with zero polarization) to display the dynamic range (i.e. standard deviation of the Hα boxes). Looking across all the images, the boxes which are at least 2σ above zero polarization in a given image are are not seen consistently above zero polarization across the images.

heat flux $q_{sat} \approx 3/2(n_e k T_e) v_{char}$.

The maximum heat flux is known as saturated conduction. The characteristic velocity v_{char} is much less than the electron thermal velocity because otherwise the electrons, which are nearly free streaming, would move too quickly compared to the ions and build up a non-zero electric field. Therefore the characteristic speed is much closer the slower ion velocity which means that the ions, which are more massive, transfer more of the heat. Fabian et al. [2011] suggest that the Hα filaments are powered through saturated conduction from the ICM ions through reconnection diffusion [Lazarian and Desiati, 2010]. The process of reconnection diffusion allows the flow of one gas into another perpendicular to a magnetic field because of the amount of turbulence in the filament. Werner et al. [2013] find both turbulent and magnetic pressure in the filaments such that the reconnection diffusion is an applicable process. Under reconnection diffusion, the ICM gas will flow into the cold filaments perpendicular to the filaments. Therefore, we would have an anisotropic velocity field of charged particles, which produces strong polarization, 5-25%, in emission lines such as Lyα and Hα [Laming, 1990]. However, we do not see strong polarization in the filaments of M87 so the reconnection diffusion process is unlikely to be the cause of the Hα filament emission. While it could be the case that our projection of the filaments is biased, it would be very difficult to change the geometry to produce a more isotropic velocity field and create an unpolarized observation in M87. Therefore, it is more likely that thermal conduction occurs under the Spitzer regime where the hot electrons interact with the filaments isotropically.

4.6 Conclusions

Astronomical polarimetry can probe the structure and physics of many types of astrophysical sources in nearly all wavebands. We present here the first imaging polarization obtained with the SOAR Telescope, including a full suite of systematic tests and calibrations that demonstrate the system can measure reproducible fractional polarization for extended targets. The addition of polarimetry capabilities to the optical imager on the SOAR Telescope provides new capabilities for the SOAR telescope. The calibration requires the standard calibration frames (i.e. bias frames and dome flats for each polarizer and filter combination) as well as unpolarized sources (standard stars and globular clusters) for zero order corrections and polarized standards (polarized stars and extended sources) to verify polarization angles as well as percentages. We find that we can set limits of polarization down to 0.3% as seen in the upper limits on the polarization of the M87 filaments, measure polarization fractions to within 20% and measure the polarization angle of strongly polarized sources to a precision of $\pm 2^\circ$.

The study of bright sources as well as additional care taken to increase the number of dither positions once the count rate is high enough not to be dominated by instrumental noise could go farther to decrease the errors on polarization measurements which are relative photometry measurements instead of the more difficult absolute photometry measurements needed for flux calibration.

The limit of 2.4% polarization for the individual $(1.5'' \times 1.5'')$ Hα filament regions, as well as the limit on the mean of all of the regions, could be improved with additional observations with a better error estimation on mean of the Q and U Stokes parameter histograms. There is a limit to measuring fainter structures, because increasing the length of observations is limited by sky variability. For increased precision, increasing the number of observations and excluding the more variable observations, likely due to bad weather.

The lack of polarization seen in the Hα filaments makes a strong case for ruling out saturated conduction as the mechanism for transporting energy from the hot ICM, to the emission-line filaments, because saturated conduction would result in strongly polarized emission of the filaments. Saturated conduction may still operate over small regions but it appears to be ruled out as the dominant method for energy transportation. However, standard Spitzer conduction is still a viable option for energy transport.

We would like to thank Dr. William Sparks for the purchase of the polarizers (purchased under the STScI Directors Discretionary Research Fund) and his feedback and support on designing the tests and calibrations. Also, we would like to thank the SOAR operators Daniel Maturana, Patricio Ugarte, Sergio Pizarro, and Alberto Pasten for their help during observing nights and SOAR Director Dr. Stephen Heathcote and Dr. Sean Points for their help with the initial installation.

Chapter 5

Summary

The state of the intracluster gas in a galaxy cluster is not only indicative of the current state of the cluster, but can also provide information about the history of the cluster. There have been many suggested methods of heating which would prevent the creation of a "cooling flow" which would cause a galaxy cluster to catastrophically cool on timescales much shorter than the age of the cluster. In this dissertation we presented analysis of both brightest cluster galaxies and their host galaxy clusters which support some of the common mechanisms proposed for heating the core of the cluster.

In Chapter 2 we saw that $\sim 40\%$ of BCGs in low central entropy clusters had UV or mid-infrared emission that was consistent with star formation such that in the infrared we were able to model the emission in the galaxy as a starburst plus an old stellar population. With such a large fraction of star formation signatures in these brightest cluster galaxies, star formation continues to have an important role in the emission characteristics of cluster cores. With these observations of large dust masses in the mid-infrared, it will be interesting to observe these BCGs at longer wavelengths with telescopes such as ALMA, which will be able to measure molecular emission in the cores and provide sources of even colder gas and metals.

In Chapter 3 we examine both the cool core galaxy cluster RXJ 2014.8-2430 as well as its BCG. This is a strong cool core cluster which shows sloshing in its core, but cavities are noticeably missing in the X-ray images. Using toy models as well as an estimate from the X-ray luminosity in the core of the cluster, we estimate the largest possible AGN cavities that could be part of this system. We also measure optical Hα emission imaging with optical spectra of the BCG and find that while there is a velocity gradient across the central region of the BCG, which may indicate that the gas is being pulled of the cluster or falling in, the centers of the stellar, optical line, and X-ray emission are in fairly good agreement. Therefore, we may have caught this cluster at a point in time when it has just begun to slosh. At this point, RXJ 2014.8-2430 is known as a radio source but the only observations have very poor resolution which prevents us from better investigating the impact of radio bubbles in the core of the cluster. A higher resolution radio image would provide definitive evidence for the AGN activity in this cluster and help answer the question of whether or not we are viewing this cluster during a unique period where the AGN has just recently turned on. Also, future X-ray missions, such as Astro-H, are of critical importance to the study of galaxy clusters because of the immense improvements in the energy resolution. With smaller energy bins it will be possible to more precisely measure metal abundances as well as separate elemental abundances. With additional ion diagnostics, it will be easier to probe the state of the gas. Improved energy resolution will also better probe the velocity widths of the X-ray gas which can be compared to the optical emission.

Chapter 4 presents our pilot study to measure optical polarization using SOI on the SOAR Telescope. We discuss the method as well as some best practices to use while observing in this mode. We review the data reduction and analysis steps to calculate Stokes parameters and polarization vectors for both strongly polarized targets as well as to compute upper limits on sources. We are able to set limits on the polarization of the Hα filaments in M87 which rule out saturated conduction as a mechanism for conducting energy from the intracluster medium into the Hα filaments of the BCG. With additional time, it is possible to measure even more precise polarizations using this new mode on the SOAR Telescope.

APPENDIX

Table A.1. Brightest Cluster Galaxy Identifications.

Cluster Name	*GALEX* IAU Name	2MASS ID	IRAC AOR	MIPS AOR
1E0657 56a	–	$06^h58^m16^s.04, -55^\circ 56' 36\ 95''$	12674048	21981440[a,b]
			23089920	23089664[a]
1E0657 56b	–	$06^h58^m35^s.16, -55^\circ 56' 55\ 8''$	12674048	21981440[a,b]
			23089920	23089664[a]
2A 0335+096	033840.6+095812[c]	03384056+0958119	18646528	18636544[a,b]

[a] MIPS AOR (Astronomical Observation Request) observation includes a 24μm observation.

[b] MIPS AOR observation includes a 70μm observation.

[c] *GALEX* observation only includes FUV measurement.

[d] *GALEX* observation only includes NUV measurement.

[e] *GALEX* observation includes both NUV and FUV measurement.

[f] MIPS AOR observation includes a 160μm observation.

[g] *Spitzer* observations were made by Donahue as part of the DDT program 488.

[h] Due to an anomalous point source in the pbcd reduction, the images needed to be reduced from the bcd frames.

[i] *GALEX* observation was taken as a Guest Investigator for Hicks et al. [2010].

[j] IRAC AOR observation only has bands 1 and 3 on target.

[k] IRAC AOR observation only has bands 2 and 4 on target.

Note. — This table is available in its entirety in a machine-readable form in the online journal [Hoffer et al., 2012b]. A portion is shown here for guidance regarding its form and content.

Table A.2. Physical Properties.

Cluster Name	Redshift	Central Entropy[a] (keV cm^2)	K_{100}[a] (keV cm^2)	alpha[a]	Scale (kpc/$''$)	IR Radius ($''$)	UV Radius ($''$)	Centroid Offset[a] (kpc)
1E0657 56a	0.2960	307.45	18.55	1.88	4.41	3.24	–	503.92
1E0657 56b	0.2960	307.45	18.55	1.88	4.41	3.24	–	216.72
2A 0335+096	0.0347	7.14	138.64	1.52	0.69	20.7	12.8	1.00
2PIGG J0011.5-2850	0.0753	101.98	214.68	0.84	1.43	10.01	17.3	2.10
2PIGG J2227.0-3041	0.0729	17.13	113.95	1.37	1.39	10.31	17.3	0.59
3C 28.0	0.1952	23.85	107.82	1.79	3.24	4.42	12.8	3.55
3C 295	0.4641	14.54	81.95	1.47	5.86	2.44	9	16.98
3C 388	0.0917	17.03	214.3	0.76	1.71	8.38	17.3	1.44

[a] Quantities defined in Cavagnolo et al. [2009] are from radially fit entropy profiles with a functional form $K(r) = K_0 + K_x(r/r_x)^\alpha$, where K_0 is the central entropy in excess above the power law fit, K_{100} is the entropy profile normalization at $100h_{70}^{-1}$ kpc from the X-ray centroid, and alpha is the best-fit power law index.

[b] UV data is taken from Hicks et al. [2010]

Note. — Redshift information and central entropies are reproduced from the ACCEPT database. The size scale is calculated as the angular distance size assuming the standard cosmology in the paper. The IR radii are set at $14.3h_{70}^{-1}$ kpc in size and are used for *2MASS* and IRAC aperture measurements except in the case where the aperture is below 5$''$. In this case the aperture is set to be 5$''$ to minimize large aperture corrections. The UV radius is set by the aperture photometry in the *GALEX* database which most closely matches the GALEXView total flux measurement. We compare the BCG positions that we derive from the *2MASS* locations in Table A.1 and compare that to the X-ray centroid in the ACCEPT database. These distances are presented in a histogram in Figure 2.1.

Note. — This table is available in its entirety in a machine-readable form in the online journal [Hoffer et al., 2012b]. A portion is shown here for guidance regarding its form and content.

Table A.3. Fluxes Matched to UV Aperture.

Name Cluster Name	Flux NUV (mag)	Error NUV (mag)	Flux FUV (mag)	Error FUV (mag)	Flux J (mag)	Error J (mag)	Flux H (mag)	Error H (mag)	Flux K (mag)	Error K (mag)
1E0657 56a	–	–	–	–	–	–	–	–	–	–
1E0657 56b	–	–	–	–	–	–	–	–	–	–
2A 0335+096	18.05	0	18.50	0	13.48	0.0130	13.13	0.0160	13.09	0.0160
2PIGG J0011.5-2850	20.07	0.1093	20.65	0.2108	13.15	0.0080	12.90	0.0100	13.05	0.0131
2PIGG J2227.0-3041	18.40	0.0176	19.85	0.0568	12.98	0.0070	12.75	0.0090	12.90	0.0106
3C 28.0	20.51	0.3453	20.56	0.2914	15.54	0.0660	15.35	0.0720	15.11	0.0697
3C 295	23.17	0	23.80	0.3245	16.38	0.1570	16.18	0.2230	15.76	0.1470
3C 388	19.95	0.0507	20.97	0.1878	13.29	0.0100	13.10	0.0120	13.28	0.0139

[a] BCGs are also in the Hicks et al. [2010] sample.

[b] BCG *GALEX* fluxes are taken from Hicks et al. [2010].

Note. — Fluxes reported with errors equal to 0 are 3σ upper limits. For NUV upper limits, the *2MASS* flux is matched with a $7''$ aperture such that it is similar in size to the GALEX PSF.

Note. — This table is available in its entirety in a machine-readable form in the online journal [Hoffer et al., 2012b]. A portion is shown here for guidance regarding its form and content.

Table A.4. *Spitzer* Aperture Flux.

Name Cluster Name	Flux 3.6μm (mJy)	Error 3.6μm (mJy)	Flux 4.5μm (mJy)	Error 4.5μm (mJy)	Flux 5.8μm (mJy)	Error 5.8μm (mJy)	Flux 8.0μm (mJy)	Error 8.0μm (mJy)	Flux 24μm (mJy)	Error 24μm (mJy)	Flux 70μm (mJy)	Error 70μm (mJy)	Flux 160μm (mJy)	Error 160μm (mJy)
1E0657 56a	0.47	0.02	0.38	0.02	0.22	0.01	0.14	0.01	0.15	0.02	5.29	0	–	–
1E0657 56b	0.57	0.03	0.46	0.02	0.26	0.01	0.17	0.01	0.11	0.02	1.43[a]	0	–	–
2A 0335+096	26.12	1.31	15.93	0.80	14.79	0.74	9.94	0.50	2.40[b]	0.24	77.10	20.36	–	–
2PIGG J0011.5-2850	–	–	–	–	–	–	–	–	–	–	–	–	–	–
2PIGG J2227.0-3041	–	–	–	–	–	–	–	–	–	–	–	–	–	–
3C 28.0	0.88	0.04	0.67	0.03	0.35	0.02	0.43	0.02	0.55[c]	0.08	6.78	0	–	–

[a] Originally, aperture flux measurement indicated a detection. However, 24 micron flux measurement and visual inspection indicated contamination in the aperture where flux is likely from an unrelated source. The reported measurement is now an upper limit computed using the point source estimate at 16″.

[b] Source not extended but has significant contamination. Point source measurement at 35″ radius is greater than 10% error margin.

[c] Source not extended but has mild source contamination. Point source measurement at 35″ radius is within 10% error.

[d] Flux measurement is a filtered detection.

[e] IRAC flux measurements derived from a BCD image that was remosaicked.

[f] Source is extended in the MIPS 24 micron image. 24 micron flux measured within the aperture (see Table A.2). Note an aperture radius of 35″ was used for NGC4636 because of significant point source contamination outside of 35″.

Note. — Fluxes reported with errors equal to 0 are 5σ upper limits.

Note. — This table is available in its entirety in a machine-readable form in the online journal [Hoffer et al., 2012b]. A portion is shown here for guidance regarding its form and content.

Table A.5. *2MASS* Aperture Flux.

Name Cluster Name	Flux J (mJy)	Error J (mJy)	Flux H (mJy)	Error H (mJy)	Flux K (mJy)	Error K (mJy)	Flux K24 (mJy)	Error K24 (mJy)
1E0657 56a	–	–	–	–	–	–	–	–
1E0657 56b	–	–	–	–	–	–	–	–
2A 0335+096	65.69	0.54	72.49	0.94	57.94	0.83	40.23	0.50
2PIGG J0011.5-2850	12.83	0.22	15.56	0.34	14.53	0.41	–	–
2PIGG J2227.0-3041	15.75	0.26	19.44	0.37	17.22	0.41	–	–
3C 28.0	1.26	0.12	1.64	0.17	1.68	0.19	3.35	0.51
3C 295	0.76	0.11	1.03	0.18	1.31	0.17	–	–
3C 388	10.31	0.18	12.48	0.28	11.57	0.32	15.38	0.49

Note. — This table is available in its entirety in a machine-readable form in the online journal [Hoffer et al., 2012b]. A portion is shown here for guidance regarding its form and content.

Table A.6. Star Formation Rates:

Name Cluster Name	SFR UV ($M_\odot$ yr^{-1})	Error UV ($M_\odot$ yr^{-1})	SFR IR ($M_\odot$ yr^{-1})	SFR $70\mu m$ ($M_\odot$ yr^{-1})	Error $70\mu m$ ($M_\odot$ yr^{-1})	SFR $24\mu m$ ($M_\odot$ yr^{-1})	Error $24\mu m$ ($M_\odot$ yr^{-1})	Mass Stellar Mass ($10^{10} M_\odot$)
1E0657 56a	–	–	2.12	5.22	0	0.91	0.11	5.52
1E0657 56b	–	–	1.64	1.65	0	0.76	0.12	6.68
2A 0335+096	–	–	0.72	0.94	0.25	0.21	0.02	5.58
2PIGG J0011.5-2850	0.92	0	–	–	–	–	–	–
2PIGG J2227.0-3041	1.82	0.33	–	–	–	–	–	–
3C 28.0	2.30	0.37	13.51	2.15	0	2.05	0.29	4.40
3C 295	–	–	–	–	–	–	–	–
3C 388	1.14	0	1.78	1.61	0.36	1.47	0.15	7.06
4C 55.16	–	–	–	–	–	–	–	–

Note. — A star formation rate uncertainty of 0 identifies the quoted rate as a 3σ upper limit.

Note. — UV SFR are calculated for all objects, including those in high K_0 systems. Upper limits are then calculated using the uncertainties on the NUV, K, and inert BCG color. If a star formation rate is consistent with a SFR of zero within 3σ, a 3σ upper limit is reported.

Note. — The IR SFR is estimated by a fit to the Groves et al. [2008] models. The 24 and 70 micron SFRs are estimated from empirical relationships reported in Calzetti et al. [2010] and the uncertainties are calculated using the 24 and 70 micron flux uncertainties, respectively.

Note. — This table is available in its entirety in a machine-readable form in the online journal [Hoffer et al., 2012b]. A portion is shown here for guidance regarding its form and content.

BIBLIOGRAPHY

BIBLIOGRAPHY

J. R. P. Angel and H. S. Stockman. Optical and infrared polarization of active extragalactic objects. *Annual Review of Astronomy and Astrophysics*, 18:321–361, 1980. doi: 10.1146/annurev.aa.18.090180.001541.

K. A. Arnaud. XSPEC: The First Ten Years. In G. H. Jacoby and J. Barnes, editors, *Astronomical Data Analysis Software and Systems V*, volume 101 of *Astronomical Society of the Pacific Conference Series*, page 17, 1996.

M. Arnaud, R. Rothenflug, O. Boulade, L. Vigroux, and E. Vangioni-Flam. Some Constraints on the Origin of the Iron Enriched Intracluster Medium. *Astronomy and Astrophysics*, 254:49, February 1992.

M. Arnaud, E. Pointecouteau, and G. W. Pratt. Calibration of the galaxy cluster M{500}-Y{X} relation with XMM-Newton. *Astronomy and Astrophysics*, 474:L37–L40, November 2007. doi: 10.1051/0004-6361:20078541.

J. N. Bahcall and C. L. Sarazin. Parameters and predictions for the X-ray emitting gas of Coma, Perseus, and Virgo. *Astrophysical Journal, Letters to the Editor*, 213:L99–L103, May 1977. doi: 10.1086/182418.

J. A. Baldwin, M. M. Phillips, and R. Terlevich. Classification parameters for the emission-line spectra of extragalactic objects. *Publications of the ASP*, 93:5–19, February 1981. doi: 10.1086/130766.

P. Bastien. A linear polarization survey of T Tauri stars. *Astrophysics and Space Science, Supplement Series*, 48:153–164, April 1982.

L. P. Bautz and G. O. Abell. Concerning the Forms of the Velocity-Distance Relation Clusters. *Astrophysical Journal*, 184:709–718, September 1973. doi: 10.1086/152363.

E. Bertschinger and A. Meiksin. The role of heat conduction in the cooling flows of galaxy clusters. *Astrophysical Journal, Letters to the Editor*, 306:L1–L5, July 1986. doi: 10.1086/184692.

J. Binney and G. Tabor. Evolving Cooling Flows. *Monthly Notices of the RAS*, 276:663, September 1995.

L. Bîrzan, D. A. Rafferty, B. R. McNamara, M. W. Wise, and P. E. J. Nulsen. A Systematic Study of Radio-induced X-Ray Cavities in Clusters, Groups, and Galaxies. *Astrophysical Journal*, 607:800–809, June 2004. doi: 10.1086/383519.

L. Bîrzan, B. R. McNamara, P. E. J. Nulsen, C. L. Carilli, and M. W. Wise. Radiative Efficiency and Content of Extragalactic Radio Sources: Toward a Universal Scaling Relation between Jet Power and Radio Power. *Astrophysical Journal*, 686:859–880, October 2008. doi: 10.1086/591416.

L. Bîrzan, D. A. Rafferty, P. E. J. Nulsen, B. R. McNamara, H. J. A. Röttgering, M. W. Wise, and R. Mittal. The duty cycle of radio-mode feedback in complete samples of clusters. *Monthly Notices of the RAS*, 427:3468–3488, December 2012. doi: 10.1111/j.1365-2966.2012.22083.x.

H. Boehringer, W. Voges, A. C. Fabian, A. C. Edge, and D. M. Neumann. A ROSAT HRI study of the interaction of the X-ray-emitting gas and radio lobes of NGC 1275. *Monthly Notices of the RAS*, 264:L25–L28, October 1993.

H. Böhringer, P. Schuecker, G. W. Pratt, M. Arnaud, T. J. Ponman, J. H. Croston, S. Borgani, R. G. Bower, U. G. Briel, C. A. Collins, M. Donahue, W. R. Forman, A. Finoguenov, M. J. Geller, L. Guzzo, J. P. Henry, R. Kneissl, J. J. Mohr, K. Matsushita, C. R. Mullis, T. Ohashi, K. Pedersen, D. Pierini, H. Quintana, S. Raychaudhury, T. H. Reiprich, A. K. Romer, P. Rosati, K. Sabirli, R. F. Temple, P. T. P. Viana, A. Vikhlinin, G. M. Voit, and Y.-Y. Zhang. The representative XMM-Newton cluster structure survey (REXCESS) of an X-ray luminosity selected galaxy cluster sample. *Astronomy and Astrophysics*, 469:363–377, July 2007a. doi: 10.1051/0004-6361:20066740.

H. Böhringer, P. Schuecker, G. W. Pratt, M. Arnaud, T. J. Ponman, J. H. Croston, S. Borgani, R. G. Bower, U. G. Briel, C. A. Collins, M. Donahue, W. R. Forman, A. Finoguenov, M. J. Geller, L. Guzzo, J. P. Henry, R. Kneissl, J. J. Mohr, K. Matsushita, C. R. Mullis, T. Ohashi, K. Pedersen, D. Pierini, H. Quintana, S. Raychaudhury, T. H. Reiprich, A. K. Romer, P. Rosati, K. Sabirli, R. F. Temple, P. T. P. Viana, A. Vikhlinin, G. M. Voit, and Y.-Y. Zhang. The representative XMM-Newton cluster structure survey (REXCESS) of an X-ray luminosity selected galaxy cluster sample. *Astronomy and Astrophysics*, 469:363–377, July 2007b. doi: 10.1051/0004-6361:20066740.

J. N. Bregman and L. P. David. Heat conduction in cooling flows. *Astrophysical Journal*, 326:639–644, March 1988. doi: 10.1086/166122.

V. Bromm, N. Yoshida, L. Hernquist, and C. F. McKee. The formation of the first stars and galaxies. *Nature*, 459:49–54, May 2009. doi: 10.1038/nature07990.

M. Brüggen. Simulations of Buoyant Bubbles in Galaxy Clusters. *Astrophysical Journal*, 592:839–845, August 2003. doi: 10.1086/375731.

M. Brüggen and C. R. Kaiser. Hot bubbles from active galactic nuclei as a heat source in cooling-flow clusters. *Nature*, 418:301–303, July 2002.

J. O. Burns. The radio properties of cD galaxies in Abell clusters. I - an X-ray selected sample. *Astronomical Journal*, 99:14–30, January 1990. doi: 10.1086/115307.

D. Calzetti, S.-Y. Wu, S. Hong, R. C. Kennicutt, J. C. Lee, D. A. Dale, C. W. Engelbracht, L. van Zee, B. T. Draine, C.-N. Hao, K. D. Gordon, J. Moustakas, E. J. Murphy, M. Regan, A. Begum, M. Block, J. Dalcanton, J. Funes, A. Gil de Paz, B. Johnson, S. Sakai, E. Skillman, F. Walter, D. Weisz, B. Williams, and Y. Wu. The Calibration of Monochromatic Far-Infrared Star Formation Rate Indicators. *Astrophysical Journal*, 714:1256–1279, May 2010. doi: 10.1088/0004-637X/714/2/1256.

N. Caon, M. Capaccioli, and M. D'Onofrio. On the Shape of the Light Profiles of Early Type Galaxies. *Monthly Notices of the RAS*, 265:1013, December 1993.

W. Cash. Parameter estimation in astronomy through application of the likelihood ratio. *Astrophysical Journal*, 228:939–947, March 1979. doi: 10.1086/156922.

B. Catinella, D. Schiminovich, G. Kauffmann, S. Fabello, J. Wang, C. Hummels, J. Lemonias, S. M. Moran, R. Wu, R. Giovanelli, M. P. Haynes, T. M. Heckman, A. R. Basu-Zych, M. R. Blanton, J. Brinchmann, T. Budavári, T. Gonçalves, B. D. Johnson, R. C. Kennicutt, B. F. Madore, C. D. Martin, M. R. Rich, L. J. Tacconi, D. A. Thilker, V. Wild, and T. K. Wyder. The GALEX Arecibo SDSS Survey - I. Gas fraction scaling relations of massive galaxies and first data release. *Monthly Notices of the RAS*, 403: 683–708, April 2010. doi: 10.1111/j.1365-2966.2009.16180.x.

K. W. Cavagnolo, M. Donahue, G. M. Voit, and M. Sun. Bandpass Dependence of X-Ray Temperatures in Galaxy Clusters. *Astrophysical Journal*, 682:821–834, August 2008a. doi: 10.1086/588630.

K. W. Cavagnolo, M. Donahue, G. M. Voit, and M. Sun. An Entropy Threshold for Strong Hα and Radio Emission in the Cores of Galaxy Clusters. *Astrophysical Journal, Letters to the Editor*, 683:L107–L110, August 2008b. doi: 10.1086/591665.

K. W. Cavagnolo, M. Donahue, G. M. Voit, and M. Sun. Intracluster Medium Entropy Profiles for a Chandra Archival Sample of Galaxy Clusters. *Astrophysical Journal, Supplement Series*, 182:12–32, May 2009. doi: 10.1088/0067-0049/182/1/12.

E. Churazov, M. Brüggen, C. R. Kaiser, H. Böhringer, and W. Forman. Evolution of Buoyant Bubbles in M87. *Astrophysical Journal*, 554:261–273, June 2001. doi: 10.1086/321357.

J. C. Clemens, J. A. Crain, and R. Anderson. The Goodman spectrograph. In A. F. M. Moorwood and M. Iye, editors, *Society of Photo-Optical Instrumentation Engineers (SPIE) Conference Series*, volume 5492 of *Society of Photo-Optical Instrumentation Engineers (SPIE) Conference Series*, pages 331–340, September 2004. doi: 10.1117/12.550069.

L. M. Close, F. Roddier, J. L. Hora, J. E. Graves, M. Northcott, C. Roddier, W. F. Hoffmann, A. Dayal, G. G. Fazio, and L. K. Deutsch. Adaptive Optics Infrared Imaging Polarimetry and Optical HST Imaging of Hubble's Variable Nebula (R Monocerotis/NGC 2261): A Close Look at a Very Young Active Herbig Ae/Be Star. *Astrophysical Journal*, 489:210, November 1997. doi: 10.1086/304777.

M. Cohen, W. A. Wheaton, and S. T. Megeath. Spectral Irradiance Calibration in the Infrared. XIV. The Absolute Calibration of 2MASS. *Astronomical Journal*, 126:1090–1096, August 2003. doi: 10.1086/376474.

E. Collett. *Field Guide to Polarized Light*. Field Guide Series. SPIE–the International Society for Optical Engineering, 2005. ISBN 9780819458681. URL `http://books.google.com/books?id=5lJwcCsLbLsC`.

J. J. Condon, W. D. Cotton, E. W. Greisen, Q. F. Yin, R. A. Perley, G. B. Taylor, and J. J. Broderick. The NRAO VLA Sky Survey. *Astronomical Journal*, 115:1693–1716, May 1998. doi: 10.1086/300337.

L. L. Cowie and J. Binney. Radiative regulation of gas flow within clusters of galaxies - A model for cluster X-ray sources. *Astrophysical Journal*, 215:723–732, August 1977. doi: 10.1086/155406.

L. L. Cowie and C. F. McKee. The evaporation of spherical clouds in a hot gas. I - Classical and saturated mass loss rates. *Astrophysical Journal*, 211:135–146, January 1977. doi: 10.1086/154911.

C. S. Crawford, S. W. Allen, H. Ebeling, A. C. Edge, and A. C. Fabian. The ROSAT Brightest Cluster Sample - III. Optical spectra of the central cluster galaxies. *Monthly Notices of the RAS*, 306:857–896, July 1999. doi: 10.1046/j.1365-8711.1999.02583.x.

C. S. Crawford, N. A. Hatch, A. C. Fabian, and J. S. Sanders. The extended Hα-emitting filaments surrounding NGC 4696, the central galaxy of the Centaurus cluster. *Monthly Notices of the RAS*, 363:216–222, October 2005. doi: 10.1111/j.1365-2966.2005.09463.x.

J. H. Croston, G. W. Pratt, H. Böhringer, M. Arnaud, E. Pointecouteau, T. J. Ponman, A. J. R. Sanderson, R. F. Temple, R. G. Bower, and M. Donahue. Galaxy-cluster gas-density distributions of the representative XMM-Newton cluster structure survey (REXCESS). *Astronomy and Astrophysics*, 487:431–443, August 2008. doi: 10.1051/0004-6361:20079154.

L. P. David, K. A. Arnaud, W. Forman, and C. Jones. Einstein observations of the Hydra A cluster and the efficiency of galaxy formation in groups and clusters. *Astrophysical Journal*, 356:32–40, June 1990a. doi: 10.1086/168812.

L. P. David, W. Forman, and C. Jones. The evolution of the interstellar medium in elliptical galaxies. I - The early wind phase. *Astrophysical Journal*, 359:29–41, August 1990b. doi: 10.1086/169030.

L. Davis, Jr. and J. L. Greenstein. The Polarization of Starlight by Aligned Dust Grains. *Astrophysical Journal*, 114:206, September 1951. doi: 10.1086/145464.

J. de Plaa, N. Werner, A. Simionescu, J. S. Kaastra, Y. G. Grange, and J. Vink. Cold fronts and multi-temperature structures in the core of Abell 2052. *Astronomy and Astrophysics*, 523:A81, November 2010. doi: 10.1051/0004-6361/201015198.

J. M. Dickey and F. J. Lockman. H I in the Galaxy. *Annual Review of Astronomy and Astrophysics*, 28:215–261, 1990. doi: 10.1146/annurev.aa.28.090190.001243.

M. Donahue and G. M. Voit. Cool Gas in Clusters of Galaxies. *Clusters of Galaxies: Probes of Cosmological Structure and Galaxy Evolution*, page 143, 2004.

M. Donahue, J. Mack, G. M. Voit, W. Sparks, R. Elston, and P. R. Maloney. Hubble Space Telescope Observations of Vibrationally Excited Molecular Hydrogen in Cluster Cooling Flow Nebulae. *Astrophysical Journal*, 545:670–694, December 2000. doi: 10.1086/317836.

M. Donahue, D. J. Horner, K. W. Cavagnolo, and G. M. Voit. Entropy Profiles in the Cores of Cooling Flow Clusters of Galaxies. *Astrophysical Journal*, 643:730–750, June 2006. doi: 10.1086/503270.

M. Donahue, S. Bruch, E. Wang, G. M. Voit, A. K. Hicks, D. B. Haarsma, J. H. Croston, G. W. Pratt, D. Pierini, R. W. O'Connell, and H. Böhringer. Star Formation and UV colors of the Brightest Cluster Galaxies in the Representative XMM-Newton Cluster Structure Survey. *Astrophysical Journal*, 715:881–896, June 2010. doi: 10.1088/0004-637X/715/2/881.

M. Donahue, G. E. de Messières, R. W. O'Connell, G. M. Voit, A. Hoffer, B. R. McNamara, and P. E. J. Nulsen. Polycyclic Aromatic Hydrocarbons, Ionized Gas, and Molecular Hydrogen in Brightest Cluster Galaxies of Cool-core Clusters of Galaxies. *Astrophysical Journal*, 732:40, May 2011. doi: 10.1088/0004-637X/732/1/40.

M. Donahue, G. M. Voit, A. Mahdavi, K. Umetsu, S. Ettori, J. Merten, M. Postman, A. Hoffer, A. Baldi, D. Coe, N. Czakon, M. Bartelmann, N. Benitez, R. Bouwens, L. Bradley, T. Broadhurst, H. Ford, F. Gastaldello, C. Grillo, L. Infante, S. Jouvel, A. Koekemoer, D. Kelson, O. Lahav, D. Lemze, E. Medezinski, P. Melchior, M. Meneghetti, A. Molino, J. Moustakas, L. A. Moustakas, M. Nonino, P. Rosati, J. Sayers, S. Seitz, A. Van der Wel, W. Zheng, and A. Zitrin. CLASH-X: A Comparison of Lensing and X-Ray Techniques for Measuring the Mass Profiles of Galaxy Clusters. *Astrophysical Journal*, 794:136, October 2014. doi: 10.1088/0004-637X/794/2/136.

J. L. Donley, G. H. Rieke, P. G. Pérez-González, and G. Barro. Spitzer's Contribution to the AGN Population. *Astrophysical Journal*, 687:111–132, November 2008. doi: 10.1086/591510.

B. T. Draine and A. Li. Infrared Emission from Interstellar Dust. IV. The Silicate-Graphite-PAH Model in the Post-Spitzer Era. *Astrophysical Journal*, 657:810–837, March 2007. doi: 10.1086/511055.

B. T. Draine and E. E. Salpeter. On the physics of dust grains in hot gas. *Astrophysical Journal*, 231:77–94, July 1979. doi: 10.1086/157165.

J. Dubinski. The Origin of the Brightest Cluster Galaxies. *Astrophysical Journal*, 502: 141, July 1998. doi: 10.1086/305901.

K. Ebneter and B. Balick. Centaurus A. *Publications of the ASP*, 95:675–690, October 1983. doi: 10.1086/131239.

A. C. Edge. The detection of molecular gas in the central galaxies of cooling flow clusters. *Monthly Notices of the RAS*, 328:762–782, December 2001. doi: 10.1046/j.1365-8711.2001.04802.x.

A. C. Edge, G. C. Stewart, and A. C. Fabian. Properties of cooling flows in a flux-limited sample of clusters of galaxies. *Monthly Notices of the RAS*, 258:177–188, September 1992.

A. C. Edge, J. B. R. Oonk, R. Mittal, S. W. Allen, S. A. Baum, H. Böhringer, J. N. Bregman, M. N. Bremer, F. Combes, C. S. Crawford, M. Donahue, E. Egami, A. C. Fabian, G. J. Ferland, S. L. Hamer, N. A. Hatch, W. Jaffe, R. M. Johnstone, B. R. McNamara, C. P. O'Dea, P. Popesso, A. C. Quillen, P. Salomé, C. L. Sarazin, G. M. Voit, R. J. Wilman, and M. W. Wise. Herschel observations of FIR emission lines in brightest cluster galaxies. *Astronomy and Astrophysics*, 518:L46, July 2010a. doi: 10.1051/0004-6361/201014569.

A. C. Edge, J. B. R. Oonk, R. Mittal, S. W. Allen, S. A. Baum, H. Böhringer, J. N. Bregman, M. N. Bremer, F. Combes, C. S. Crawford, M. Donahue, E. Egami, A. C. Fabian, G. J. Ferland, S. L. Hamer, N. A. Hatch, W. Jaffe, R. M. Johnstone, B. R. McNamara, C. P. O'Dea, P. Popesso, A. C. Quillen, P. Salomé, C. L. Sarazin, G. M. Voit, R. J. Wilman, and M. W. Wise. Herschel photometry of brightest cluster galaxies in cooling flow clusters. *Astronomy and Astrophysics*, 518:L47, July 2010b. doi: 10.1051/0004-6361/201014572.

E. Egami, G. H. Rieke, D. Fadda, and D. C. Hines. A Large Mass of H_2 in the Brightest Cluster Galaxy in Zwicky 3146. *Astrophysical Journal, Letters to the Editor*, 652:L21–L24, November 2006. doi: 10.1086/509886.

R. Elston and P. Maloney. Molecular Hydrogen Emission from Central Cluster Galaxies in Cooling Flows. In I. S. McLean, editor, *Astronomy with Arrays, The Next Generation*, volume 190 of *Astrophysics and Space Science Library*, page 169, 1994.

A. C. Fabian. Cooling Flows in Clusters of Galaxies. *Annual Review of Astronomy and Astrophysics*, 32:277–318, 1994a. doi: 10.1146/annurev.aa.32.090194.001425.

A. C. Fabian. Cooling Flows in Clusters of Galaxies. *Annual Review of Astronomy and Astrophysics*, 32:277–318, 1994b. doi: 10.1146/annurev.aa.32.090194.001425.

A. C. Fabian and P. E. J. Nulsen. Subsonic accretion of cooling gas in clusters of galaxies. *Monthly Notices of the RAS*, 180:479–484, August 1977.

A. C. Fabian, J. S. Sanders, S. Ettori, G. B. Taylor, S. W. Allen, C. S. Crawford, K. Iwasawa, R. M. Johnstone, and P. M. Ogle. Chandra imaging of the complex X-ray core of the Perseus cluster. *Monthly Notices of the RAS*, 318:L65–L68, November 2000. doi: 10.1046/j.1365-8711.2000.03904.x.

A. C. Fabian, J. S. Sanders, G. B. Taylor, S. W. Allen, C. S. Crawford, R. M. Johnstone, and K. Iwasawa. A very deep Chandra observation of the Perseus cluster: shocks, ripples and conduction. *Monthly Notices of the RAS*, 366:417–428, February 2006. doi: 10.1111/j.1365-2966.2005.09896.x.

A. C. Fabian, J. S. Sanders, R. J. R. Williams, A. Lazarian, G. J. Ferland, and R. M. Johnstone. The energy source of the filaments around the giant galaxy NGC 1275. *Monthly Notices of the RAS*, 417:172–177, October 2011. doi: 10.1111/j.1365-2966.2011.19034.x.

G. G. Fazio, J. L. Hora, L. E. Allen, M. L. N. Ashby, P. Barmby, L. K. Deutsch, J.-S. Huang, S. Kleiner, M. Marengo, S. T. Megeath, G. J. Melnick, M. A. Pahre, B. M. Patten, J. Polizotti, H. A. Smith, R. S. Taylor, Z. Wang, S. P. Willner, W. F. Hoffmann, J. L. Pipher, W. J. Forrest, C. W. McMurty, C. R. McCreight, M. E. McKelvey, R. E. McMurray, D. G. Koch, S. H. Moseley, R. G. Arendt, J. E. Mentzell, C. T. Marx, P. Losch, P. Mayman, W. Eichhorn, D. Krebs, M. Jhabvala, D. Y. Gezari, D. J. Fixsen, J. Flores, K. Shakoorzadeh, R. Jungo, C. Hakun, L. Workman, G. Karpati, R. Kichak, R. Whitley, S. Mann, E. V. Tollestrup, P. Eisenhardt, D. Stern, V. Gorjian, B. Bhattacharya, S. Carey, B. O. Nelson, W. J. Glaccum, M. Lacy, P. J. Lowrance, S. Laine, W. T. Reach, J. A. Stauffer, J. A. Surace, G. Wilson, E. L. Wright, A. Hoffman, G. Domingo, and M. Cohen. The Infrared Array Camera (IRAC) for the Spitzer Space Telescope. *Astrophysical Journal, Supplement Series*, 154:10–17, September 2004. doi: 10.1086/422843.

G. J. Ferland, A. C. Fabian, N. A. Hatch, R. M. Johnstone, R. L. Porter, P. A. M. van Hoof, and R. J. R. Williams. Collisional heating as the origin of filament emission in galaxy clusters. *Monthly Notices of the RAS*, 392:1475–1502, February 2009. doi: 10.1111/j.1365-2966.2008.14153.x.

C. Ferrari, M. Arnaud, S. Ettori, S. Maurogordato, and J. Rho. Chandra observation of the multiple merger cluster Abell 521. *Astronomy and Astrophysics*, 446:417–428, February 2006. doi: 10.1051/0004-6361:20053946.

A. H. Gonzalez, A. I. Zabludoff, and D. Zaritsky. Intracluster Light in Nearby Galaxy Clusters: Relationship to the Halos of Brightest Cluster Galaxies. *Astrophysical Journal*, 618:195–213, January 2005. doi: 10.1086/425896.

A. H. Gonzalez, D. Zaritsky, and A. I. Zabludoff. A Census of Baryons in Galaxy Clusters and Groups. *Astrophysical Journal*, 666:147–155, September 2007. doi: 10.1086/519729.

N. Grevesse and A. J. Sauval. Standard Solar Composition. *Space Science Reviews*, 85:161–174, May 1998. doi: 10.1023/A:1005161325181.

B. Groves, M. A. Dopita, R. S. Sutherland, L. J. Kewley, J. Fischera, C. Leitherer, B. Brandl, and W. van Breugel. Modeling the Pan-Spectral Energy Distribution of Starburst Galaxies. IV. The Controlling Parameters of the Starburst SED. *Astrophysical Journal, Supplement Series*, 176:438–456, June 2008. doi: 10.1086/528711.

H. Gursky, E. Kellogg, S. Murray, C. Leong, H. Tananbaum, and R. Giacconi. A Strong X-Ray Source in the Coma Cluster Observed by UHURU. *Astrophysical Journal, Letters to the Editor*, 167:L81, August 1971. doi: 10.1086/180765.

M. Hamuy, N. B. Suntzeff, S. R. Heathcote, A. R. Walker, P. Gigoux, and M. M. Phillips. Southern spectrophotometric standards, 2. *Publications of the ASP*, 106:566–589, June 1994. doi: 10.1086/133417.

T. M. Heckman, S. A. Baum, W. J. M. van Breugel, and P. McCarthy. Dynamical, physical, and chemical properties of emission-line nebulae in cooling flows. *Astrophysical Journal*, 338:48–77, March 1989. doi: 10.1086/167181.

J.-C. Henoux, G. Chambe, D. Heristchi, M. Semel, B. Woodgate, D. Shine, and J. Beckers. Conductive flux in the chromosphere derived from line linear polarization observation. *Solar Physics*, 86:115–122, July 1983a. doi: 10.1007/BF00157180.

J. C. Henoux, D. Heristchi, G. Chambe, B. Woodgate, R. Shine, J. Beckers, and M. Machado. Conductive flux in flaring solar chromospheres deduced from the linear polarization observations. *Astronomy and Astrophysics*, 119:233–238, March 1983b.

R. C. Hickox and M. Markevitch. Absolute Measurement of the Unresolved Cosmic X-Ray Background in the 0.5-8 keV Band with Chandra. *Astrophysical Journal*, 645:95–114, July 2006. doi: 10.1086/504070.

A. K. Hicks, R. Mushotzky, and M. Donahue. Detecting Star Formation in Brightest Cluster Galaxies with GALEX. *Astrophysical Journal*, 719:1844–1858, August 2010. doi: 10.1088/0004-637X/719/2/1844.

P. Hickson and S. van den Bergh. CCD observations of the polarization of the Crab Nebula. *Astrophysical Journal*, 365:224–229, December 1990. doi: 10.1086/169473.

J. G. Hoessel. The photometric properties of brightest cluster galaxies. II - SIT and CCD surface photometry. *Astrophysical Journal*, 241:493–506, October 1980. doi: 10.1086/158364.

J. G. Hoessel, J. E. Gunn, and T. X. Thuan. The photometric properties of brightest cluster galaxies. I - Absolute magnitudes in 116 nearby Abell clusters. *Astrophysical Journal*, 241:486–492, October 1980. doi: 10.1086/158363.

A. S. Hoffer, M. Donahue, A. Hicks, and R. S. Barthelemy. Infrared and Ultraviolet Star Formation in Brightest Cluster Galaxies in the ACCEPT Sample. *Astrophysical Journal, Supplement Series*, 199:23, March 2012a. doi: 10.1088/0067-0049/199/1/23.

A. S. Hoffer, M. Donahue, A. Hicks, and R. S. Barthelemy. IR and UV star formation in ACCEPT BCGs (Hoffer+, 2012). *VizieR Online Data Catalog*, 219:90023, March 2012b.

E. M. Hu, L. L. Cowie, and Z. Wang. Long-slit spectroscopy of gas in the cores of X-ray luminous clusters. *Astrophysical Journal, Supplement Series*, 59:447–498, December 1985. doi: 10.1086/191081.

W. Jaffe and M. N. Bremer. Molecular hydrogen emission in cooling flows. *Monthly Notices of the RAS*, 284:L1–L5, January 1997.

T. H. Jarrett, T. Chester, R. Cutri, S. E. Schneider, and J. P. Huchra. The 2MASS Large Galaxy Atlas. *Astronomical Journal*, 125:525–554, February 2003. doi: 10.1086/345794.

R. I. Jedrzejewski. CCD surface photometry of elliptical galaxies. I - Observations, reduction and results. *Monthly Notices of the RAS*, 226:747–768, June 1987.

B. D. Johnson, D. Schiminovich, M. Seibert, M. Treyer, D. C. Martin, T. A. Barlow, K. Forster, P. G. Friedman, P. Morrissey, S. G. Neff, T. Small, T. K. Wyder, L. Bianchi, J. Donas, T. M. Heckman, Y.-W. Lee, B. F. Madore, B. Milliard, R. M. Rich, A. S. Szalay, B. Y. Welsh, and S. K. Yi. Ultraviolet, Optical, and Infrared Constraints on Models of Stellar Populations and Dust Attenuation. *Astrophysical Journal, Supplement Series*, 173:377–391, December 2007a. doi: 10.1086/522932.

B. D. Johnson, D. Schiminovich, M. Seibert, M. Treyer, D. C. Martin, T. A. Barlow, K. Forster, P. G. Friedman, P. Morrissey, S. G. Neff, T. Small, T. K. Wyder, L. Bianchi, J. Donas, T. M. Heckman, Y.-W. Lee, B. F. Madore, B. Milliard, R. M. Rich, A. S. Szalay, B. Y. Welsh, and S. K. Yi. Ultraviolet through Infrared Spectral Energy Distributions from 1000 SDSS Galaxies: Dust Attenuation. *Astrophysical Journal, Supplement Series*, 173:392–403, December 2007b. doi: 10.1086/522960.

H. M. Johnson. Hubble's variable nebula NGC 2261. *Astronomical Journal*, 71:224–227, April 1966. doi: 10.1086/109910.

J. S. Kaastra and R. Mewe. X-ray emission from thin plasmas. I - Multiple Auger ionisation and fluorescence processes for Be to Zn. *Astrophysics and Space Science, Supplement Series*, 97:443–482, January 1993.

E. Kellogg and S. Murray. Studies of cluster X-ray sources - Size measurements. *Astrophysical Journal, Letters to the Editor*, 193:L57–L60, October 1974. doi: 10.1086/181630.

R. C. Kennicutt, Jr. The rate of star formation in normal disk galaxies. *Astrophysical Journal*, 272:54–67, September 1983. doi: 10.1086/161261.

R. C. Kennicutt, Jr. Star Formation in Galaxies Along the Hubble Sequence. *Annual Review of Astronomy and Astrophysics*, 36:189–232, 1998. doi: 10.1146/annurev.astro.36.1.189.

R. C. Kennicutt, Jr., L. Armus, G. Bendo, D. Calzetti, D. A. Dale, B. T. Draine, C. W. Engelbracht, K. D. Gordon, A. D. Grauer, G. Helou, D. J. Hollenbach, T. H. Jarrett, L. J. Kewley, C. Leitherer, A. Li, S. Malhotra, M. W. Regan, G. H. Rieke, M. J. Rieke, H. Roussel, J.-D. T. Smith, M. D. Thornley, and F. Walter. SINGS: The SIRTF Nearby Galaxies Survey. *Publications of the ASP*, 115:928–952, August 2003. doi: 10.1086/376941.

J. M. Laming. Emission-line polarization as an equilibration diagnostic for nonradiative shock fronts. *Astrophysical Journal*, 362:219–225, October 1990. doi: 10.1086/169257.

A. Lazarian and P. Desiati. Magnetic Reconnection as the Cause of Cosmic Ray Excess from the Heliospheric Tail. *Astrophysical Journal*, 722:188–196, October 2010. doi: 10.1088/0004-637X/722/1/188.

S. M. Lea, J. Silk, E. Kellogg, and S. Murray. Thermal-Bremsstrahlung Interpretation of Cluster X-Ray Sources. *Astrophysical Journal, Letters to the Editor*, 184:L105, September 1973. doi: 10.1086/181300.

L. Leisman, D. B. Haarsma, D. A. Sebald, and ACCEPT Team. Brightest Cluster Galaxy Identification. In *American Astronomical Society Meeting Abstracts #217*, volume 43 of *Bulletin of the American Astronomical Society*, page 149.08, January 2011.

D. A. Liedahl, A. L. Osterheld, and W. H. Goldstein. New calculations of Fe L-shell X-ray spectra in high-temperature plasmas. *Astrophysical Journal, Letters to the Editor*, 438: L115–L118, January 1995. doi: 10.1086/187729.

J. Magorrian, S. Tremaine, D. Richstone, R. Bender, G. Bower, A. Dressler, S. M. Faber, K. Gebhardt, R. Green, C. Grillmair, J. Kormendy, and T. Lauer. The Demography of Massive Dark Objects in Galaxy Centers. *Astronomical Journal*, 115:2285–2305, June 1998. doi: 10.1086/300353.

A. Mahdavi, H. Hoekstra, A. Babul, J. Sievers, S. T. Myers, and J. P. Henry. Joint Analysis of Cluster Observations. I. Mass Profile of Abell 478 from Combined X-Ray, Sunyaev-Zel'dovich, and Weak-Lensing Data. *Astrophysical Journal*, 664:162–180, July 2007. doi: 10.1086/517958.

A. Mahdavi, H. Hoekstra, A. Babul, C. Bildfell, T. Jeltema, and J. P. Henry. Joint Analysis of Cluster Observations. II. Chandra/XMM-Newton X-Ray and Weak Lensing Scaling Relations for a Sample of 50 Rich Clusters of Galaxies. *Astrophysical Journal*, 767:116, April 2013. doi: 10.1088/0004-637X/767/2/116.

D. Makovoz and F. R. Marleau. Point-Source Extraction with MOPEX. *Publications of the ASP*, 117:1113–1128, October 2005. doi: 10.1086/432977.

D. C. Martin, J. Fanson, D. Schiminovich, P. Morrissey, P. G. Friedman, T. A. Barlow, T. Conrow, R. Grange, P. N. Jelinsky, B. Milliard, O. H. W. Siegmund, L. Bianchi, Y.-I. Byun, J. Donas, K. Forster, T. M. Heckman, Y.-W. Lee, B. F. Madore, R. F. Malina, S. G. Neff, R. M. Rich, T. Small, F. Surber, A. S. Szalay, B. Welsh, and T. K. Wyder. The Galaxy Evolution Explorer: A Space Ultraviolet Survey Mission. *Astrophysical Journal, Letters to the Editor*, 619:L1–L6, January 2005. doi: 10.1086/426387.

W. G. Mathews and J. N. Bregman. Radiative accretion flow onto giant galaxies in clusters. *Astrophysical Journal*, 224:308–319, September 1978. doi: 10.1086/156379.

B. J. Maughan, P. A. Giles, S. W. Randall, C. Jones, and W. R. Forman. Self-similar scaling and evolution in the galaxy cluster X-ray luminosity-temperature relation. *Monthly Notices of the RAS*, 421:1583–1602, April 2012. doi: 10.1111/j.1365-2966.2012.20419.x.

B. R. McNamara and P. E. J. Nulsen. Heating Hot Atmospheres with Active Galactic Nuclei. *Annual Review of Astronomy and Astrophysics*, 45:117–175, September 2007. doi: 10.1146/annurev.astro.45.051806.110625.

B. R. McNamara, M. Wise, C. L. Sarazin, B. T. Jannuzi, and R. Elston. Optical Structure in the Abell 1795 Cluster Central Galaxy: Evidence for Stripping and Deflection of Radio Jets. *Astrophysical Journal, Letters to the Editor*, 466:L9, July 1996. doi: 10.1086/310162.

B. R. McNamara, M. Wise, P. E. J. Nulsen, L. P. David, C. L. Sarazin, M. Bautz, M. Markevitch, A. Vikhlinin, W. R. Forman, C. Jones, and D. E. Harris. Chandra X-Ray Observations of the Hydra A Cluster: An Interaction between the Radio Source and the X-Ray-emitting Gas. *Astrophysical Journal, Letters to the Editor*, 534:L135–L138, May 2000. doi: 10.1086/312662.

B. R. McNamara, M. W. Wise, P. E. J. Nulsen, L. P. David, C. L. Carilli, C. L. Sarazin, C. P. O'Dea, J. Houck, M. Donahue, S. Baum, M. Voit, R. W. O'Connell, and A. Koekemoer. Discovery of Ghost Cavities in the X-Ray Atmosphere of Abell 2597. *Astrophysical Journal, Letters to the Editor*, 562:L149–L152, December 2001. doi: 10.1086/338326.

B. R. McNamara, P. E. J. Nulsen, M. W. Wise, D. A. Rafferty, C. Carilli, C. L. Sarazin, and E. L. Blanton. The heating of gas in a galaxy cluster by X-ray cavities and large-scale shock fronts. *Nature*, 433:45–47, January 2005. doi: 10.1038/nature03202.

R. Mewe, E. H. B. M. Gronenschild, and G. H. J. van den Oord. Calculated X-radiation from optically thin plasmas. V. *Astrophysics and Space Science, Supplement Series*, 62: 197–254, November 1985.

R. Mewe, J. R. Lemen, and G. H. J. van den Oord. Calculated X-radiation from optically thin plasmas. VI - Improved calculations for continuum emission and approximation formulae for nonrelativistic average Gaunt factors. *Astrophysics and Space Science, Supplement Series*, 65:511–536, September 1986.

P. Morrissey, T. Conrow, T. A. Barlow, T. Small, M. Seibert, T. K. Wyder, T. Budavári, S. Arnouts, P. G. Friedman, K. Forster, D. C. Martin, S. G. Neff, D. Schiminovich, L. Bianchi, J. Donas, T. M. Heckman, Y.-W. Lee, B. F. Madore, B. Milliard, R. M. Rich, A. S. Szalay, B. Y. Welsh, and S. K. Yi. The Calibration and Data Products of GALEX. *Astrophysical Journal, Supplement Series*, 173:682–697, December 2007. doi: 10.1086/520512.

R. F. Mushotzky and M. Loewenstein. Lack of Evolution in the Iron Abundance in Clusters of Galaxies and Implications for the Global Star Formation Rate at High Redshift. *Astrophysical Journal, Letters to the Editor*, 481:L63, June 1997. doi: 10.1086/310651.

R. W. O'Connell. Far-Ultraviolet Radiation from Elliptical Galaxies. *Annual Review of Astronomy and Astrophysics*, 37:603–648, 1999. doi: 10.1146/annurev.astro.37.1.603.

C. P. O'Dea, S. A. Baum, G. Privon, J. Noel-Storr, A. C. Quillen, N. Zufelt, J. Park, A. Edge, H. Russell, A. C. Fabian, M. Donahue, C. L. Sarazin, B. McNamara, J. N. Bregman, and E. Egami. An Infrared Survey of Brightest Cluster Galaxies. II. Why are Some Brightest Cluster Galaxies Forming Stars? *Astrophysical Journal*, 681:1035–1045, July 2008. doi: 10.1086/588212.

K. P. O'Dea, A. C. Quillen, C. P. O'Dea, G. R. Tremblay, B. T. Snios, S. A. Baum, K. Christiansen, J. Noel-Storr, A. C. Edge, M. Donahue, and G. M. Voit. Hubble Space Telescope Far-ultraviolet Observations of Brightest Cluster Galaxies: The Role of Star Formation in Cooling Flows and BCG Evolution. *Astrophysical Journal*, 719:1619–1632, August 2010. doi: 10.1088/0004-637X/719/2/1619.

E. S. Perlman, J. A. Biretta, F. Zhou, W. B. Sparks, and F. D. Macchetto. Optical and Radio Polarimetry of the M87 Jet at 0.2" Resolution. *Astronomical Journal*, 117: 2185–2198, May 1999. doi: 10.1086/300844.

J. R. Peterson and A. C. Fabian. X-ray spectroscopy of cooling clusters. *Physics Reports*, 427:1–39, April 2006. doi: 10.1016/j.physrep.2005.12.007.

J. R. Peterson, S. M. Kahn, F. B. S. Paerels, J. S. Kaastra, T. Tamura, J. A. M. Bleeker, C. Ferrigno, and J. G. Jernigan. High-Resolution X-Ray Spectroscopic Constraints on Cooling-Flow Models for Clusters of Galaxies. *Astrophysical Journal*, 590:207–224, June 2003. doi: 10.1086/374830.

M. Postman and T. R. Lauer. Brightest cluster galaxies as standard candles. *Astrophysical Journal*, 440:28–47, February 1995. doi: 10.1086/175245.

M. Postman, D. Coe, N. Benítez, L. Bradley, T. Broadhurst, M. Donahue, H. Ford, O. Graur, G. Graves, S. Jouvel, A. Koekemoer, D. Lemze, E. Medezinski, A. Molino, L. Moustakas, S. Ogaz, A. Riess, S. Rodney, P. Rosati, K. Umetsu, W. Zheng, A. Zitrin, M. Bartelmann, R. Bouwens, N. Czakon, S. Golwala, O. Host, L. Infante, S. Jha, Y. Jimenez-Teja, D. Kelson, O. Lahav, R. Lazkoz, D. Maoz, C. McCully, P. Melchior, M. Meneghetti, J. Merten, J. Moustakas, M. Nonino, B. Patel, E. Regös, J. Sayers, S. Seitz, and A. Van der Wel. The Cluster Lensing and Supernova Survey with Hubble: An Overview. *Astrophysical Journal, Supplement Series*, 199:25, April 2012. doi: 10.1088/0067-0049/199/2/25.

G. W. Pratt, J. H. Croston, M. Arnaud, and H. Böhringer. Galaxy cluster X-ray luminosity scaling relations from a representative local sample (REXCESS). *Astronomy and Astrophysics*, 498:361–378, May 2009a. doi: 10.1051/0004-6361/200810994.

G. W. Pratt, J. H. Croston, M. Arnaud, and H. Böhringer. Galaxy cluster X-ray luminosity scaling relations from a representative local sample (REXCESS). *Astronomy and Astrophysics*, 498:361–378, May 2009b. doi: 10.1051/0004-6361/200810994.

A. C. Quillen, N. Zufelt, J. Park, C. P. O'Dea, S. A. Baum, G. Privon, J. Noel-Storr, A. Edge, H. Russell, A. Fabian, M. Donahue, J. N. Bregman, B. R. McNamara, and

C. L. Sarazin. An Infrared Survey of Brightest Cluster Galaxies. I. *Astrophysical Journal, Supplement Series*, 176:39–58, May 2008. doi: 10.1086/525560.

D. A. Rafferty, B. R. McNamara, P. E. J. Nulsen, and M. W. Wise. The Feedback-regulated Growth of Black Holes and Bulges through Gas Accretion and Starbursts in Cluster Central Dominant Galaxies. *Astrophysical Journal*, 652:216–231, November 2006. doi: 10.1086/507672.

D. A. Rafferty, B. R. McNamara, and P. E. J. Nulsen. The Regulation of Cooling and Star Formation in Luminous Galaxies by Active Galactic Nucleus Feedback and the Cooling-Time/Entropy Threshold for the Onset of Star Formation. *Astrophysical Journal*, 687: 899–918, November 2008. doi: 10.1086/591240.

S. W. Randall, C. Jones, M. Markevitch, E. L. Blanton, P. E. J. Nulsen, and W. R. Forman. Gas Sloshing and Bubbles in the Galaxy Group NGC 5098. *Astrophysical Journal*, 700:1404–1414, August 2009. doi: 10.1088/0004-637X/700/2/1404.

W. T. Reach, S. T. Megeath, M. Cohen, J. Hora, S. Carey, J. Surace, S. P. Willner, P. Barmby, G. Wilson, W. Glaccum, P. Lowrance, M. Marengo, and G. G. Fazio. Absolute Calibration of the Infrared Array Camera on the Spitzer Space Telescope. *Publications of the ASP*, 117:978–990, September 2005. doi: 10.1086/432670.

T. H. Reiprich and H. Böhringer. The Mass Function of an X-Ray Flux-limited Sample of Galaxy Clusters. *Astrophysical Journal*, 567:716–740, March 2002. doi: 10.1086/338753.

G. H. Rieke, E. T. Young, C. W. Engelbracht, D. M. Kelly, F. J. Low, E. E. Haller, J. W. Beeman, K. D. Gordon, J. A. Stansberry, K. A. Misselt, J. Cadien, J. E. Morrison, G. Rivlis, W. B. Latter, A. Noriega-Crespo, D. L. Padgett, K. R. Stapelfeldt, D. C. Hines, E. Egami, J. Muzerolle, A. Alonso-Herrero, M. Blaylock, H. Dole, J. L. Hinz, E. Le Floc'h, C. Papovich, P. G. Pérez-González, P. S. Smith, K. Y. L. Su, L. Bennett, D. T. Frayer, D. Henderson, N. Lu, F. Masci, M. Pesenson, L. Rebull, J. Rho, J. Keene, S. Stolovy, S. Wachter, W. Wheaton, M. W. Werner, and P. L. Richards. The Multiband Imaging Photometer for Spitzer (MIPS). *Astrophysical Journal, Supplement Series*, 154: 25–29, September 2004. doi: 10.1086/422717.

G. B. Rybicki and A. P. Lightman. *Radiative processes in astrophysics.* 1979.

S. Salim, R. M. Rich, S. Charlot, J. Brinchmann, B. D. Johnson, D. Schiminovich, M. Seibert, R. Mallery, T. M. Heckman, K. Forster, P. G. Friedman, D. C. Martin, P. Morrissey, S. G. Neff, T. Small, T. K. Wyder, L. Bianchi, J. Donas, Y.-W. Lee, B. F. Madore, B. Milliard, A. S. Szalay, B. Y. Welsh, and S. K. Yi. UV Star Formation Rates in the Local Universe. *Astrophysical Journal, Supplement Series*, 173:267–292, December 2007. doi: 10.1086/519218.

A. J. R. Sanderson, A. C. Edge, and G. P. Smith. LoCuSS: the connection between brightest cluster galaxy activity, gas cooling and dynamical disturbance of X-ray cluster cores. *Monthly Notices of the RAS*, 398:1698–1705, October 2009. doi: 10.1111/j.1365-2966.2009.15214.x.

C. L. Sarazin. *X-ray emission from clusters of galaxies.* 1988.

C. L. Sarazin and J. N. Bahcall. X-ray line emission for clusters of galaxies. II - Numerical models. *Astrophysical Journal, Supplement Series*, 34:451–467, August 1977. doi: 10.1086/190457.

D. J. Schlegel, D. P. Finkbeiner, and M. Davis. Maps of Dust Infrared Emission for Use in Estimation of Reddening and Cosmic Microwave Background Radiation Foregrounds. *Astrophysical Journal*, 500:525, June 1998. doi: 10.1086/305772.

G. D. Schmidt, J. R. P. Angel, and E. A. Beaver. The small-scale polarization of the Crab Nebula. *Astrophysical Journal*, 227:106–113, January 1979. doi: 10.1086/156708.

B. Sheehan, G. Kyne, P. Collins, M. Redfern, and A. Shearer. Detectors for High-Speed Polarimetric Observations Using GASP. In *Proceedings of High Time Resolution Astrophysics - The Era of Extremely Large Telescopes (HTRA-IV). May 5 - 7, 2010. Agios Nikolaos, Crete Greece. Published online at ¡A href="http://pos.sissa.it/cgi-bin/reader/conf.cgi?confid=108"¿http://pos.sissa.it/cgi-bin/reader/conf.cgi?confid=108¡/A¿, id.53*, 2010.

A. Simionescu, N. Werner, W. R. Forman, E. D. Miller, Y. Takei, H. Böhringer, E. Churazov, and P. E. J. Nulsen. Metal transport by gas sloshing in M87. *Monthly Notices of the RAS*, 405:91–99, June 2010. doi: 10.1111/j.1365-2966.2010.16450.x.

W. B. Sparks, F. Macchetto, and D. Golombek. Imaging observations of gas and dust in NGC 4696 and implications for cooling flow models. *Astrophysical Journal*, 345:153–162, October 1989a. doi: 10.1086/167890.

W. B. Sparks, F. Paresce, and D. Macchetto. Polarization and visual intensity of the inner light echo around SN 1987A. *Astrophysical Journal, Letters to the Editor*, 347:L65–L68, December 1989b. doi: 10.1086/185609.

W. B. Sparks, M. Donahue, A. Jordán, L. Ferrarese, and P. Côté. X-Ray and Optical Filaments in M87. *Astrophysical Journal*, 607:294–301, May 2004. doi: 10.1086/383189.

W. B. Sparks, J. E. Pringle, M. Donahue, R. Carswell, M. Voit, M. Cracraft, and R. G. Martin. Discovery of C IV Emission Filaments in M87. *Astrophysical Journal, Letters to the Editor*, 704:L20–L24, October 2009. doi: 10.1088/0004-637X/704/1/L20.

W. B. Sparks, J. E. Pringle, R. F. Carswell, M. Donahue, R. Martin, M. Voit, M. Cracraft, N. Manset, and J. H. Hough. Hundred Thousand Degree Gas in the Virgo Cluster of Galaxies. *Astrophysical Journal, Letters to the Editor*, 750:L5, May 2012. doi: 10.1088/2041-8205/750/1/L5.

W. B. Sparks, J. E. Pringle, R. F. Carswell, G. M. Voit, M. Donahue, M. Cracraft, E. T. Meyer, J. H. Hough, and N. Manset. Polarization Diagnostics for Cool Core Cluster Emission Lines. *Astrophysical Journal*, 780:66, January 2014. doi: 10.1088/0004-637X/780/1/66.

D. N. Spergel, R. Bean, O. Doré, M. R. Nolta, C. L. Bennett, J. Dunkley, G. Hinshaw, N. Jarosik, E. Komatsu, L. Page, H. V. Peiris, L. Verde, M. Halpern, R. S. Hill, A. Kogut, M. Limon, S. S. Meyer, N. Odegard, G. S. Tucker, J. L. Weiland, E. Wollack, and E. L. Wright. Three-Year Wilkinson Microwave Anisotropy Probe (WMAP) Observations: Implications for Cosmology. *Astrophysical Journal, Supplement Series*, 170:377–408, June 2007. doi: 10.1086/513700.

L. Spitzer. *Physics of Fully Ionized Gases*. 1962.

M. Sun. Every BCG with a Strong Radio Agn has an X-Ray Cool Core: Is the Cool Core-Noncool Core Dichotomy Too Simple? *Astrophysical Journal*, 704:1586–1604, October 2009. doi: 10.1088/0004-637X/704/2/1586.

M. Sun, C. Jones, W. Forman, A. Vikhlinin, M. Donahue, and M. Voit. X-Ray Thermal Coronae of Galaxies in Hot Clusters: Ubiquity of Embedded Mini-Cooling Cores. *Astrophysical Journal*, 657:197–231, March 2007. doi: 10.1086/510895.

T. Takahashi, K. Mitsuda, R. Kelley, F. Aharonian, F. Akimoto, S. Allen, N. Anabuki, L. Angelini, K. Arnaud, H. Awaki, A. Bamba, N. Bando, M. Bautz, R. Blandford, K. Boyce, G. Brown, M. Chernyakova, P. Coppi, E. Costantini, J. Cottam, J. Crow, J. de Plaa, C. de Vries, J.-W. den Herder, M. Dipirro, C. Done, T. Dotani, K. Ebisawa, T. Enoto, Y. Ezoe, A. Fabian, R. Fujimoto, Y. Fukazawa, S. Funk, A. Furuzawa, M. Galeazzi, P. Gandhi, K. Gendreau, K. Gilmore, Y. Haba, K. Hamaguchi, I. Hatsukade, K. Hayashida, J. Hiraga, K. Hirose, A. Hornschemeier, J. Hughes, U. Hwang, R. Iizuka, K. Ishibashi, M. Ishida, K. Ishimura, Y. Ishisaki, N. Isobe, M. Ito, N. Iwata, J. Kaastra, T. Kallman, T. Kamae, H. Katagiri, J. Kataoka, S. Katsuda, M. Kawaharada, N. Kawai, S. Kawasaki, D. Khangaluyan, C. Kilbourne, K. Kinugasa, S. Kitamoto, T. Kitayama, T. Kohmura, M. Kokubun, T. Kosaka, T. Kotani, K. Koyama, A. Kubota, H. Kunieda, P. Laurent, F. Lebrun, O. Limousin, M. Loewenstein, K. Long, G. Madejski, Y. Maeda, K. Makishima, M. Markevitch, H. Matsumoto, K. Matsushita, D. McCammon, J. Miller, S. Mineshige, K. Minesugi, T. Miyazawa, T. Mizuno, K. Mori, H. Mori, K. Mukai, H. Murakami, T. Murakami, R. Mushotzky, Y. Nakagawa, T. Nakagawa, H. Nakajima, T. Nakamori, K. Nakazawa, Y. Namba, M. Nomachi, S. O'Dell, H. Ogawa, M. Ogawa, K. Ogi, T. Ohashi, M. Ohno, M. Ohta, T. Okajima, N. Ota, M. Ozaki, F. Paerels, S. Paltani, A. Parmar, R. Petre, M. Pohl, S. Porter, B. Ramsey, C. Reynolds, S.-I. Sakai, R. Sambruna, G. Sato, Y. Sato, P. Serlemitsos, M. Shida, T. Shimada, K. Shinozaki, P. Shirron, R. Smith, G. Sneiderman, Y. Soong, L. Stawarz, H. Sugita, A. Szymkowiak, H. Tajima, H. Takahashi, Y. Takei, T. Tamagawa, T. Tamura, K. Tamura, T. Tanaka, Y. Tanaka, Y. Tanaka, M. Tashiro, Y. Tawara, Y. Terada, Y. Terashima, F. Tombesi, H. Tomida, M. Tozuka, Y. Tsuboi, M. Tsujimoto, H. Tsunemi, T. Tsuru, H. Uchida, Y. Uchiyama, H. Uchiyama, Y. Ueda, S. Uno, M. Urry, S. Watanabe, N. White, T. Yamada, H. Yamaguchi, K. Yamaoka, N. Yamasaki, M. Yamauchi, S. Yamauchi, Y. Yatsu, D. Yonetoku, and A. Yoshida. The ASTRO-H Mission. In *Society of Photo-Optical Instrumentation Engineers (SPIE) Conference Series*, volume 7732 of *Society of Photo-Optical Instrumentation Engineers (SPIE) Conference Series*, July 2010. doi: 10.1117/12.857875.

A. G. G. M. Tielens. Interstellar Polycyclic Aromatic Hydrocarbon Molecules. *Annual Review of Astronomy and Astrophysics*, 46:289–337, September 2008. doi: 10.1146/annurev.astro.46.060407.145211.

D. Tody. IRAF in the Nineties. In R. J. Hanisch, R. J. V. Brissenden, and J. Barnes, editors, *Astronomical Data Analysis Software and Systems II*, volume 52 of *Astronomical Society of the Pacific Conference Series*, page 173, January 1993.

W. H. Tucker and R. Rosner. Thermal conduction and heating by nonthermal electrons in the X-ray halo of M87. *Astrophysical Journal*, 267:547–550, April 1983. doi: 10.1086/160891.

D. A. Turnshek, R. C. Bohlin, R. L. Williamson, II, O. L. Lupie, J. Koornneef, and D. H. Morgan. An atlas of Hubble Space Telescope photometric, spectrophotometric, and polarimetric calibration objects. *Astronomical Journal*, 99:1243–1261, April 1990. doi: 10.1086/115413.

P. G. van Dokkum. Cosmic-Ray Rejection by Laplacian Edge Detection. *Publications of the ASP*, 113:1420–1427, November 2001. doi: 10.1086/323894.

G. M. Voit and M. Donahue. A Deep Look at the Emission-Line Nebula in Abell 2597. *Astrophysical Journal*, 486:242, September 1997. doi: 10.1086/304509.

G. M. Voit and M. Donahue. The Fate of Stellar Mass Loss in Central Cluster Galaxies. *Astrophysical Journal, Letters to the Editor*, 738:L24, September 2011. doi: 10.1088/2041-8205/738/2/L24.

G. M. Voit, G. L. Bryan, M. L. Balogh, and R. G. Bower. Modified Entropy Models for the Intracluster Medium. *Astrophysical Journal*, 576:601–624, September 2002. doi: 10.1086/341864.

G. M. Voit, K. W. Cavagnolo, M. Donahue, D. A. Rafferty, B. R. McNamara, and P. E. J. Nulsen. Conduction and the Star Formation Threshold in Brightest Cluster Galaxies. *Astrophysical Journal, Letters to the Editor*, 681:L5–L8, July 2008. doi: 10.1086/590344.

A. von der Linden, P. N. Best, G. Kauffmann, and S. D. M. White. How special are brightest group and cluster galaxies? *Monthly Notices of the RAS*, 379:867–893, August 2007. doi: 10.1111/j.1365-2966.2007.11940.x.

A. R. Walker, M. Boccas, M. Bonati, R. Galvez, M. Martinez, P. Schurter, R. E. Schmidt, M. C. Ashe, F. Delgado, and R. Tighe. The SOAR Optical Imager. In M. Iye and A. F. M. Moorwood, editors, *Society of Photo-Optical Instrumentation Engineers (SPIE) Conference Series*, volume 4841 of *Society of Photo-Optical Instrumentation Engineers (SPIE) Conference Series*, pages 286–294, March 2003. doi: 10.1117/12.457977.

S. A. Walker, A. C. Fabian, and J. S. Sanders. Large-scale gas sloshing out to half the virial radius in the strongest cool core REXCESS galaxy cluster, RXJ2014.8-2430. *Monthly Notices of the RAS*, March 2014. doi: 10.1093/mnrasl/slu040.

J. Wang, R. Overzier, G. Kauffmann, A. von der Linden, and X. Kong. The UV-optical colours of brightest cluster galaxies in optically and X-ray selected clusters. *Monthly Notices of the RAS*, 401:433–444, January 2010. doi: 10.1111/j.1365-2966.2009.15653.x.

D. W. Weedman, F. R. Feldman, V. A. Balzano, L. W. Ramsey, R. A. Sramek, and C.-C. Wuu. NGC 7714 - The prototype star-burst galactic nucleus. *Astrophysical Journal*, 248:105–112, August 1981. doi: 10.1086/159133.

M. C. Weisskopf, B. Brinkman, C. Canizares, G. Garmire, S. Murray, and L. P. Van Speybroeck. An Overview of the Performance and Scientific Results from the Chandra X-Ray Observatory. *Publications of the ASP*, 114:1–24, January 2002. doi: 10.1086/338108.

M. W. Werner, T. L. Roellig, F. J. Low, G. H. Rieke, M. Rieke, W. F. Hoffmann, E. Young, J. R. Houck, B. Brandl, G. G. Fazio, J. L. Hora, R. D. Gehrz, G. Helou, B. T. Soifer, J. Stauffer, J. Keene, P. Eisenhardt, D. Gallagher, T. N. Gautier, W. Irace, C. R. Lawrence, L. Simmons, J. E. Van Cleve, M. Jura, E. L. Wright, and D. P. Cruikshank. The Spitzer Space Telescope Mission. *Astrophysical Journal, Supplement Series*, 154:1–9, September 2004. doi: 10.1086/422992.

N. Werner, A. Simionescu, E. T. Million, S. W. Allen, P. E. J. Nulsen, A. von der Linden, S. M. Hansen, H. Böhringer, E. Churazov, A. C. Fabian, W. R. Forman, C. Jones, J. S. Sanders, and G. B. Taylor. Feedback under the microscope-II. Heating, gas uplift and mixing in the nearest cluster core. *Monthly Notices of the RAS*, 407:2063–2074, October 2010. doi: 10.1111/j.1365-2966.2010.16755.x.

N. Werner, J. B. R. Oonk, R. E. A. Canning, S. W. Allen, A. Simionescu, J. Kos, R. J. van Weeren, A. C. Edge, A. C. Fabian, A. von der Linden, P. E. J. Nulsen, C. S. Reynolds, and M. Ruszkowski. The Nature of Filamentary Cold Gas in the Core of the Virgo Cluster. *Astrophysical Journal*, 767:153, April 2013. doi: 10.1088/0004-637X/767/2/153.

S. D. M. White and C. S. Frenk. Galaxy formation through hierarchical clustering. *Astrophysical Journal*, 379:52–79, September 1991. doi: 10.1086/170483.

A. S. Wilson. The structure of the Crab Nebula-IV. The variation of polarization with wavelength. *Monthly Notices of the RAS*, 166:617–632, March 1974.

L. Woltjer. The polarization and intensity distribution in the Crab nebula derived from plates taken with the 200-inch telescope by Dr. W. Baade. *Bulletin Astronomical Inst. Netherlands*, 13:301, September 1957.

E. L. Wright. A Cosmology Calculator for the World Wide Web. *Publications of the ASP*, 118:1711–1715, December 2006. doi: 10.1086/510102.

H. Wu, C. Cao, C.-N. Hao, F.-S. Liu, J.-L. Wang, X.-Y. Xia, Z.-G. Deng, and C. K.-S. Young. PAH and Mid-Infrared Luminosities as Measures of Star Formation Rate in Spitzer First Look Survey Galaxies. *Astrophysical Journal, Letters to the Editor*, 632:L79–L82, October 2005. doi: 10.1086/497961.

J. A. ZuHone, M. Markevitch, and R. E. Johnson. Stirring Up the Pot: Can Cooling Flows in Galaxy Clusters be Quenched by Gas Sloshing? *Astrophysical Journal*, 717: 908–928, July 2010. doi: 10.1088/0004-637X/717/2/908.

F. Zwicky. On the Masses of Nebulae and of Clusters of Nebulae. *Astrophysical Journal*, 86:217, October 1937. doi: 10.1086/143864.

F. Zwicky. On the Clustering of Nebulae. *Publications of the ASP*, 50:218–220, August 1938. doi: 10.1086/124935.

F. Zwicky, E. Herzog, P. Wild, M. Karpowicz, and C. T. Kowal. *Catalogue of galaxies and of clusters of galaxies, Vol. I.* 1961.